POLITECNICO DI TORINO

Master's Degree in Aerospace Engineering

Master's Degree Thesis

Adaptation of a grid model for the generation of a prescribed full-depth atmospheric boundary layer in a wind tunnel

Supervisors

Prof. Gaetano IUSO

Prof. Ramis ÖRLÜ

Dr. Geoffrey TANGUY

Candidate

Emanuele Antonio D'ALÒ

October 2022

Abstract

The Atmospheric Boundary Layer (ABL) is the lowest part of the atmosphere and its behaviour is directly influenced by turbulence. The study of its characteristics is essential for a broad spectrum of applications: wind turbines, civil engineering, marine engineering, meteorology, etc.

The internship project focuses on the reproduction of a "full-depth" ABL in the wind tunnel. Multiscale Inhomogeneous Grids (MIG) and spires are used for this, which are designed in order to simulate any prescribed flows and to avoid trial-and-error approaches. The key objective is to obtain a prescribed mean velocity profile and a turbulence intensity profile representative of the real atmosphere.

A theoretical model based on interacting wake turbulence is used to design the MIG grids and spires. These are produced in additive manufacturing and tested in the SCL-PIV wind tunnel at Onera Lille. The measurements are taken with both the Single Hot Wire Anemometer (S-HWA) and the Cross Hot Wire Anemometer (X-HWA).

The experimental investigation showed that in order to obtain relevant findings, it is necessary to artificially simulate the Earth's surface roughness in the wind tunnel. The results proved that grids and spires are capable of reproducing a full-depth artificial boundary layer with a mean velocity profile representative of a real ABL. Moreover, these atmospheric flow generators allows to control the boundary layer height. However for all the grids, the produced turbulence intensity was insufficient for simulating the ABL. This is not valid for the spires, that generates turbulent intensity sufficiently high over the whole boundary layer height.

The experimental campaign showed that the spires are the best device to reproduce an artificial ABL topped by an undisturbed freestream in the wind tunnel. Indeed, they allow to tailor accurately the mean velocity profile and to produce a turbulent intensity profile representative of the full-scale ABL.

Keywords

Atmospheric Boundary Layer, Turbulence, Wind Tunnel, Grids, Spires, Hot Wire Anemometry.

Acknowledgements

I am sincerely grateful to my supervisor at Onera, Geoffrey Tanguy, for sharing his valuable knowledge and encouraging me during my experience. I would also like to extend my deepest gratitude to the PhD student Thomas Huret, who was always available for sharing his expertise and for guiding me during the project. Being at Onera has been a great experience for my professional and personal growth.

I would like to thank my supervisor at Polito, Gaetano Iuso, for following my activities and for his support during my thesis.

Special thanks to Ramis Örlü, my supervisor at KTH, for giving me the opportunity to get experience at one of the top research institutes in Europe and for supporting me throughout the internship.

There are just never enough words to properly express my gratitude to my family. My parents, sister, and grandparents have always encouraged me to follow my aspirations and supported with all my decisions.

Table of Contents

List of Figures

List of Tables

Chapter 1

Introduction

The Atmospheric Boundary Layer (ABL) is a complex environment where turbulence is the major force behind exchanges of momentum, heat, humidity or chemical species in the lower atmosphere. In this environment, turbulence itself is influenced by both momentum and heat distributions, with considerable variations depending on terrain characteristics and topography, time of the day and meteorological conditions.

Quantifying the effects of the Atmospheric Boundary Layer (ABL) characteristics is essential for design and validation steps in a broad spectrum of applications, gathered within the designation of Wind Engineering: wind turbines, civil engineering (e.g. buildings and bridges design), aerial dispersion of pollutants, take-off/landing aeronautics, marine engineering, marine aerodynamics (e.g. aircraft interactions with ships, sailing boats), meteorology, etc. The complexity of the turbulent exchange processes between the atmosphere and the Earth surface (for both oceans and continents) [14] justifies the use of wind tunnel experiments, where artificial flows similar to the natural full-scale ABL have to be generated.

Over the past decades, several techniques were investigated in wind tunnel facilities in order to reproduce ABL characteristics. This was also justified by the high Reynolds numbers of the ABL flow, which made it extremely challenging to carry out accurate numerical simulations due to limited computational resources. The huge length scales are the primary cause of the high Reynolds number. In the atmosphere it is possible to reach $Re_\theta > 10^6$ [15], where $Re_\theta = \frac{U_\infty \theta}{\nu}$ is the Reynolds number based on the *"momentum thickness"* θ[1], the kinematic viscosity ν, and freestream velocity U_∞.

Although some of the devices discovered in the last fifty years were successful, such as the one from Counihan (1969) [16] which are still used nowadays, they are based on empirical assumptions and limited to specific ABL configurations. As a result, several academic institutions and private enterprises continue to fund ABL research in order to improve the already available tools and investigate the numerous applications impacted by this flow.

[1] $\theta = \int_0^\delta \frac{U}{U_\infty}\left(1 - \frac{U}{U_\infty}\right) dy$, where U is the streamwise mean velocity

1.1 Motivation

Devices for the production of such artificial atmospheric flows consist essentially in passive obstacles designed to thicken a boundary layer and produce mean velocity and turbulent intensity profiles that are similar to the observed profiles from the real Atmospheric Boundary Layer [16]. These devices, which were created in recent decades, were used by both research centers and private enterprises. (Figure 1.1). More recently, new flow regimes were achieved using active grids, mainly for academic purpose [17].

Figure 1.1: ABL generation device in an industrial wind tunnel. Credits: Shimizu Corporation.

However, all of these current generation devices suffer from three main difficulties:

1. A design process essentially based on trial-and-error, with difficulties for adaptation to the broad range of potential atmospheric configurations. The design technique provided by Irwin (1981) [18] is an exception since it may create a predefined mean flow profile even though it does not specifically tailor the turbulent intensity profile;

2. The generated flows do not reproduce accurately the profiles of integral length scales of turbulence (the characteristic scales of the most energetic turbulent structures). Although the order of magnitude is usually correct, the correct profile's shape is not achieved [19];

3. They are not suited for the reproduction of thermal stratification configurations (stable or unstable), although they are the most frequently encountered in the atmosphere [14]. In order to take into account heat transfer, expensive wind tunnel facilities with differential heating and cooling systems are required [20].

Examples of the passive devices used nowadays are: grids, spires, mixing obstacles or roughness fetch. These are designed through trials and cannot be easily adapted to different flow conditions without preliminary experimental tests. However, the Multiscale Inhomogeneous Grids (MIG), presented by Zheng *et al.* (2018) [11] and based on theoretical techniques on interacting wakes turbulence, might offer an independent control of mean flow and turbulence intensity profile.

1.2 Purpose

The internship project is carried out at ONERA (Office National d'Etudes et de Recherches Aérospatiales, France) under the supervision of Geoffrey Tanguy (Research Engineer at ONERA) and Thomas Huret (PhD student at ONERA). Indeed, the work is conducted in collaboration with the PhD student Thomas Huret who developed a MIG design model by using the McCarthy (1964) [21] approach in order to study the ABL's logarithmic region.

The aim of the internship is at modifying the aforementioned MIG design model in order to reproduce a "full-depth" ABL (topped by an undisturbed freestream) in the wind tunnel. The key objective is to design grids and spires with a prescribed mean velocity profile and a turbulence intensity profile as close as possible to the values measured in the real atmosphere. The last point is the most challenging since passive grids are known to produce weak turbulence intensity sufficiently far downstream.

A secondary goal concerns the study of the interaction between the free stream and the artificial boundary layer. This analysis is carried out by adapting the existing design algorithm to produce partial section grids and by studying the flow behavior in the "mixing layer" created between the end of the grid and the empty section of the wind tunnel.

Additionally, the research will provide useful insight and data for the Huret's wider investigation, which aims to develop a theoretical model to tailor mean velocity, turbulence intensity and integral length scales profiles produced in the wind tunnel by the MIG grids.

1.3 Research methodology

Following recommendations from the literature, a technique for the design of both full-section and partial-section grids has been established in the project's initial phase. After the design stage, the grids have been 3D printed using PLA with 100% of fill.

Several experimental tests have been conducted in a $H \times W = 0.29\ m \times 0.3\ m$ wind tunnel at ONERA Lille in order to characterize the flow generated by the grids. This was done undertaking one-point measurements through Hot-Film Anemometry (both single probe and X-cross probe).

Then, in order to address some of the issues found, better grids were designed using the collected data. To establish whether issues with the previous grids had been resolved, the new set of grids was tested in the wind tunnel and the findings were compared with those of the earlier grids.

Finally, the same theoretical method and the same design algorithm were adapted to create spires generating the same objective velocity profile of the grids. In order to choose the ideal device for the ABL reproduction, the spires were tested in wind tunnel and the data gathered were compared with those from the grids.

1.4 Outline

The manuscript is divided into three major sections: a global background, an overview of the methodological approach implemented during the study, and a presentation and discussion of the findings.

Chapter 2 provides an overview of the main characteristics of the Atmospheric Boundary Layer and the different experimental methods employed in the last decades to reproduce such a complex flow in the wind tunnel.

The first section of Chapter 3 describes the main experimental setup and the measurements techniques used in the wind tunnel to characterize the flow. The second part of the chapter outlines the main features of MIG grids and provides a brief description of the theoretical model [21] applied for the grids design.

Chapter 4 describes the main steps of the research, the devices utilized and the design decision made to meet the project goals. The entire design procedure is accurately described, starting from the application of the McCarthy (1964) [21] model through to the grids production. Additionally, the necessity of recreating Earth's surface roughness is highlighted, and two distinct techniques are introduced in order to meet the roughness similarity condition.

The results obtained in the experimental campaigns are presented and examined in Chapter 5. The turbulent flows produced by the different grids and spires are compared in order to establish which configuration best meets our objectives.

Chapter 6 summarizes the significant outcomes obtained from the experimental investigation, along with suggestion for future work in ABL-related industrial applications .

Chapter 2

Theoretical background

2.1 The Atmospheric Boundary Layer

The Atmospheric Boundary Layer (ABL) is the layer of the atmosphere directly impacted by the presence of the Earth surface (both continents and oceans), responding to surface forcings with timescales lower than one hour (Stull, 1988 [14]). These forcings are related to exchanges of momentum (from surface frictional drag), heat transfers and humidity transfers that are mainly due to the turbulent motion of the air (Monin & Obukhov, 1954 [4]). The boundary layer height can vary in time and space, ranging from 300 m and 3000 m, depending on the meteorological, topological and dynamical conditions (Stull, 1988 [14]). It is topped by the Free Troposphere, a portion of the earth's atmosphere in which the effect of the earth's surface friction on the air motion is negligible, and in which the air is usually treated (dynamically) as an ideal fluid. The free troposphere extends up to the interface between troposphere and stratosphere, which is called *"tropopause"* and can exist anywhere between 6 km and 18 km (M. Dameris, 2003 [22]), usually an average value of 11 km is considered.

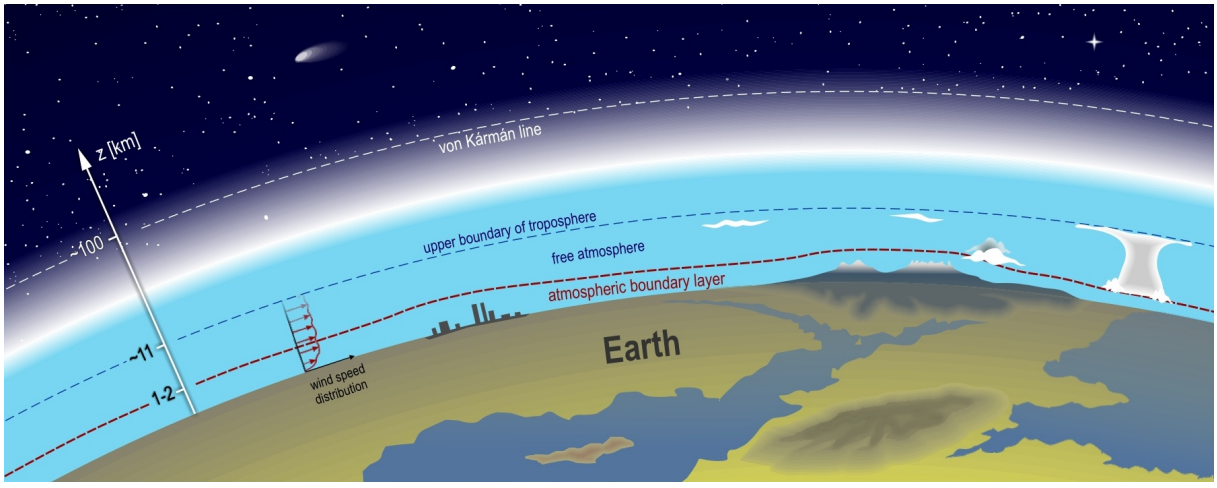

Figure 2.1: The troposphere structure and its approximate mean equilibrium, extracted from [1].

Temperature non-uniformities (which lead to pressure non-uniformities) are primarily

caused by the diurnal cycle of surface heating and cooling, the presence of clouds, and horizontal variability in surface properties, and they have a significant impact on the structure of ABL turbulence and global air motion (J.R. Garrat, 1994 [23]). The atmospheric motions at very large scales (planetary scales) is governed by the so called *"Geostrophic equilibrium"* that exists between the Coriolis force and the pressure force associated with these thermal non-uniformities (as shown in figure 2.2a).

As explained by Holton [2], turbulence has a negligible effect at very large scales. As the surface is approached, however, the Reynolds stresses become increasingly significant because they are responsible for the momentum loss propagation from the ground to the upper layer through turbulent friction. In this region, a new force equilibrium establishes between Coriolis force, pressure force and turbulent friction (see figure 2.2b). The turbulent friction causes a continuous shift of mean flow velocity direction toward the lowest pressure region (which can be modeled through the so-called *Ekman's spiral*, see section 2.3). The boundary layer is referred to as the *Ekman Boundary Layer* when such a phenomenon is visible (meaning that the influence of the Coriolis force is not negligible), which formally coincides with the Atmospheric Boundary Layer (this is true for neutral ABL but not always for convective boundary layers, as shown by J. C. Kaimal and J. J. Finnigan, 1994 [5]).

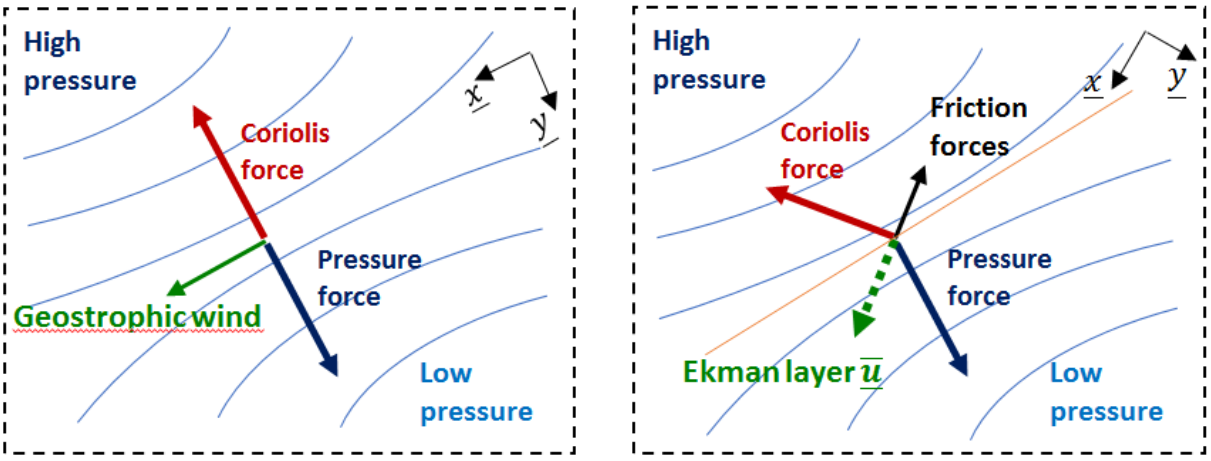

(a) Geostrophic equilibrium scheme

(b) Forces equilibrium in the Ekman layer

Figure 2.2: Schemes of force balance in the Atmospheric Boundary Layer, inspired by Holton (2012) [2] and Smith (2001) [3].

To make analysis easier, the ABL is frequently subdivided into different regions (as shown in figure 2.3). Starting at the Earth surface, Monin & Obukhov (1954) [4] named the first region encountered the *Surface Layer* (SL), which may be considered as the inner portion of the Ekman layer. According to J. C. Kaimal and J. J. Finnigan (1994) [5], this region extends up to about 50 m – 100 m and it is characterized by a significant turbulent intensity, of the order of 20 – 30%. Because this layer is very close to the surface, it experiences high vertical gradients which controls the transfer of momentum, mass and heat. Observations support the notion that these fluxes are constant over altitude, and

this hypothesis enabled Monin & Obukhov (1954) [4] to derive their similarity model, which establishes the foundations for a description of the ABL dependencies in relation to air thermal stratification. The Surface Layer (SL) in turn contains in its inner part the *Roughness Sublayer* (RSL) and in its outer part the *Inertial Sublayer* (ISL). The RSL has a thickness of approximately 2 to 3 times the height of the roughness obstacles. Moreover, it is influenced by individual roughness, resulting in horizontal changes in the time-averaged flow on the roughness elements' scale (Mahrt, 1999 [24]). Finally, the ISL extends from the top of the Roughness sublayer to the region where Coriolis forces are not negligible (outer part of the Ekman Boundary Layer).

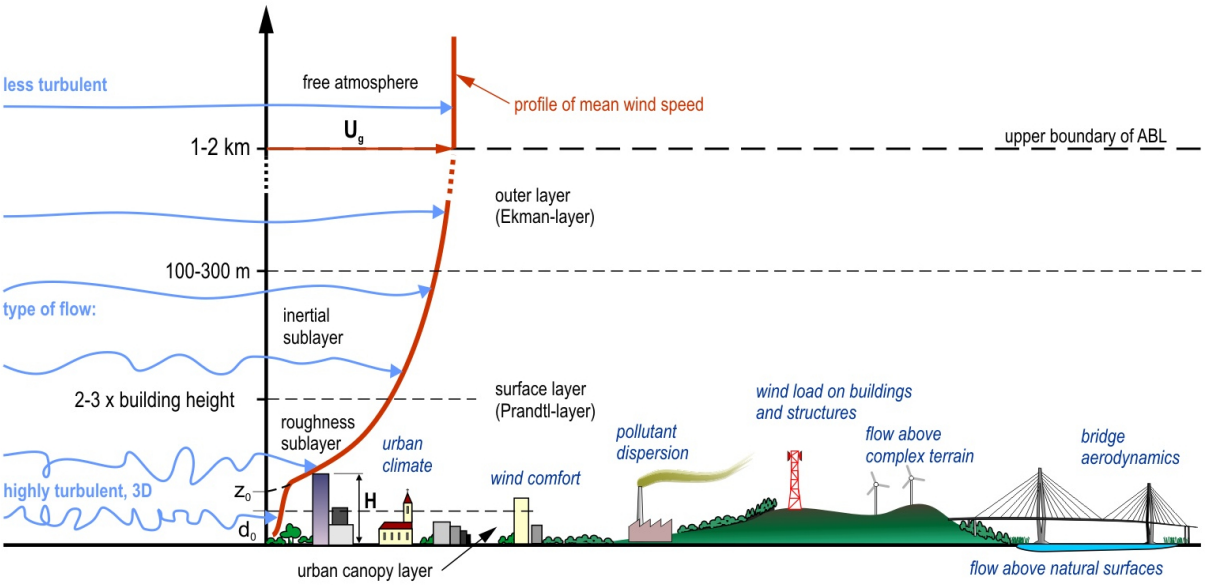

Figure 2.3: Schematic visualization of the structure of a neutral Atmospheric Boundary Layer (ABL), taken from [1].

In general, turbulence is several orders of magnitude more efficient at transporting quantities than is molecular diffusivity. Turbulence permits the boundary layer to adapt to surface forcing changes [14]. In particular, the ABL flow is the consequence of a competition between vertical shear (relative to vertical momentum flux) and thermal stratification (relative to vertical heat flux), both of which impact turbulence production (or exhaustion). This competition may be measured using the Richardson number Ri, which was first established by L. F. Richardson (1920) [25] and currently has several definitions depending on whether it is computed as a ratio of fluxes or a ratio of gradients (the latter being easier to observe during terrain experimental campaigns) [2]. The Obukhov Length (defined in A. S. Monin and A. M. Obukhov, 1954 [4]) can also evaluate the aforementioned competition:

$$L = -\frac{u_*^3}{\kappa \frac{g}{T_0} \frac{q}{c_p \rho}}$$

Where $u_* = \sqrt{-\langle u'w' \rangle}$ is the friction velocity, g stands for the gravitational acceleration, T_0 is the mean potential temperature at the considered layer, $q = \rho c_p \langle T'w' \rangle_{surface}$ the

turbulent heat flux at the surface, c_p the specific constant-pressure heat capacity, ρ the density of air and κ the Von Kármán constant ($\sim 0.35 - 0.41$ [14]). In general at low altitudes, vertical shear predominates over thermal stratification in the lower layers of the ABL, however in the upper layers, the opposite is true. The Obukhov Length may be used to determine the height at which thermal stratification has a non-negligible impact on the flow. By knowing the ABL thickness H, it is possible to study the stability of the ABL through the ratio $\frac{H}{L}$. Similar considerations may be done with the Richardson parameter (R_i) and three main flow regimes can be distinguished for the ABL.

2.2 Different types of boundary layers in the atmosphere

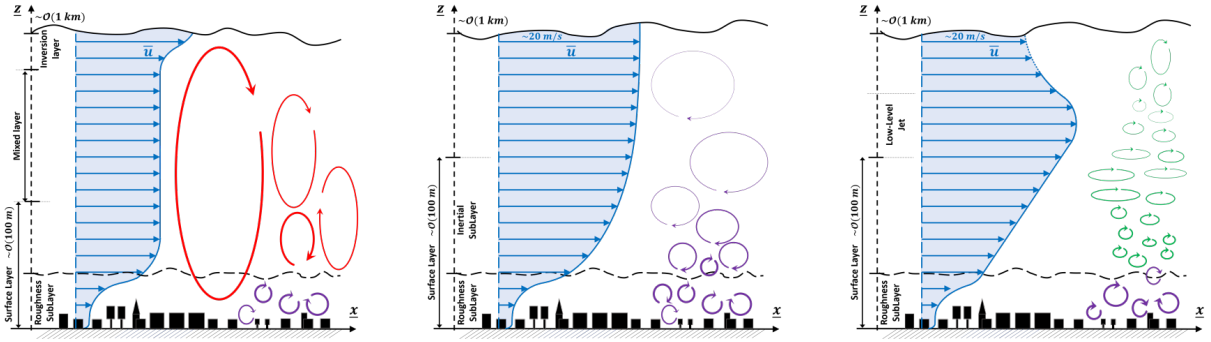

(a) Convective boundary layer (CBL)

(b) Neutral ABL

(c) Stable boundary layer (SBL)

Figure 2.4: Schematic visualization of the Atmospheric Boundary Layer (ABL) in its three main thermal stability conditions. (a) Based on [4], [5], [6]. (b) Based on [4], [5], [7]. (c) Based on [4], [5], [8], [9].

2.2.1 Neutral ABL

When the heat flux measured at the surface is negligible (Ri and H/L near to 0, L infinite), the thermal stratification has a neutral role for the production of turbulence, keeping just shear as a source term. This case corresponds to a "Neutral Surface Layer "(Figure 2.4b). It is worth to mention that in the atmosphere, completely neutral stability conditions are rare. The atmospheric boundary layer may be regarded near-neutral during gloomy skies and strong surface geostrophic winds, and simpler theoretical and semiempirical methodologies established for neutral boundary layers by fluid dynamists and engineers can be applied in meteorology (Holton, 2012 [2]). Jiménez, 2004 [26] proved that a Neutral ABL is analogous to a classical turbulent boundary layer over a rough surface. Different formulation have been introduced during the years to approximate the neutral boundary layer.

2.2.1.1 The power-law profile

Fluid dynamicists employed a power-law to characterize flat-plate boundary layers as well as channel flows. However, meteorologists utilize a modified power-law since wind speed does not grow monotonously with height up to the top of the ABL:

$$U = U_{ref} \left(\frac{z}{z_{ref}} \right)^{\alpha} \tag{2.1}$$

where U_{ref} is the mean velocity (or wind speed) at a reference height z_{ref}, that has to be smaller or equal to the the height corresponding to the mean velocity maximum; a standard reference of 10 m is commonly used.
Although the power-law lacks a solid physical basis, it typically provides a reasonable fit to the observed velocity profiles in the lower part of the ABL. The exponent α is found to depend on both the surface roughness and stability. Under near-neutral conditions, the values of α range from 0.10 for smooth water, snow, and ice surfaces to about 0.40 for well-developed urban areas (Holton, 2001). Historically, the first classifications of terrain roughness were established based on this parameter (see for instance Davenport, 1960 [27]). With increasing stability, the exponent α approaches one (equivalent to a linear profile) in highly stable conditions.

2.2.1.2 The log-law profile

The ABL physically follows a "law-of-the-wall" with a logarithmic mean velocity profile [4], which depend on the surface roughness through the "roughness height" h_0^r and on the "displacement height" d which shifts the origin of the altitudes according to the surface characteristics. Grimmond, 1999 [28] showed that these length scales are non-trivial functions (because aggregated by aerodynamics effects) of the roughness geometry. This law is valid in the aforementioned Inertial SubLayer (ISL) and it is usually expressed as a function of z:

$$\overline{u}(z) = \frac{u_*}{\kappa} ln \left(\frac{z-d}{h_0^r} \right) \tag{2.2}$$

where $u_* = \sqrt{\frac{\tau_w}{\rho}}$ is the *friction velocity*, κ the *Von Karman* constant which could be chosen in the range between 0.35 and 0.41, even though it is generally assumed to be around 0.40.

The different surface terrains have an influence on the velocity profile which is embodied by the two parameters h_0^r and d. To make the analysis of the ABL unique, several classifications of different surface terrains in terms of h_0^r and d have been proposed in the recent decades. Davenport was one among the meteorologists who worked on this, proposing a first classification in 1960 [27], then updating it for the first time to include smoother terrains, and ultimately presenting the final classification in 2000 [29], which included urban areas (see Figure 2.5b). Another classification (Figure 2.5a) was proposed

by the Engineering Science Data Unit (ESDU) in its 1985 report 85020 [7], which was established by a committee of international experts assembled by the company ESDU (it should be noted that A.G. Davenport was a member of this scientific commitee for the referred ESDU report). While the Davenport categorization is more connected with the United States, the latter is more developed in Europe (Laporte 2010) [30].
It can be observed that in both the classifications, d assumes negligible values except for very high roughness, while h_0^r is always relatively small with respect to the real height of the roughness obstacles.

Terrain Description	z_0 (m)	d (m)
City centres Forests	0.7	15 to 25
Small towns Suburbs of large towns and cities Wooded country (many trees)	0.3	5 to 10
Outskirts of small towns Villages Countryside with many hedges, some trees and some buildings	0.1	0 to 2
Open level country with few trees and hedges and isolated buildings; typical farmland	0.03	0
Fairly level grass plains with isolated trees	0.01	0
Very rough sea in extreme storms (once in 50-yr extreme) Flat areas with short grass and no obstructions Runway area of airports	0.003	0
Rough sea in annual extreme storms Snow covered farmland Flat desert or arid areas Inland lakes in extreme storms	0.001	0

(a) ESDU 82026 classification. The table is extracted from the report ESDU 85020 (1985) [7].

z_0 (m)	Classification	Landscape	C_{DN}
0.0002	Sea	Calm sea, paved areas, snow-covered flat plain, tide flat, smooth desert.	0.0014
0.005	Smooth	Beaches, pack ice, morass, snow-covered fields.	0.0028
0.03	Open	Grass prairie or farm fields, tundra, airports, heather.	0.0047
0.1	Roughly open	Cultivated area with low crops and occasional obstacles (single bushes).	0.0075
0.25	Rough	High crops, crops of varied height, scattered obstacles such as trees or hedgerows, vineyards.	0.012
0.5	Very rough	Mixed farm fields and forest clumps, orchards, scattered buildings.	0.018
1.0	Closed	Regular coverage with large size obstacles with open spaces roughly equal to obstacle heights, suburban houses, villages, mature forests.	0.030
≥2	Chaotic	Centers of large towns and cities, irregular forests with scattered clearings.	0.062

(b) Revised Davenport's classification, presented in [29]. The table is taken from [31]. The C_{DN} value expresses the drag coefficient for neutral static stability.

Figure 2.5: The two main classifications for terrain characteristics.

2.2.1.3 Law of the wake

The *"law of the wake"* (2.3) formulated by Coles (1956) [32] is particularly useful being representative of inner layer, overlap and outer region of the boundary layer. This law was established for both pipe flows and flat boundary layers. It is a superposition of the "law of the wall" and the law of the wake due to the free turbulence at the core (in pipe flows). If the Coriolis forces are neglected, which is often the case in classical wind tunnel facilities (due to the difficulties given by large rotating facilities required to simulate these forces), the full-depth neutral ABL can be reproduced by using the law of the wake:

$$U^+ = \frac{1}{\kappa}\ln z^+ + C - \Delta U^+ + \frac{\Pi(x)}{\kappa}\omega\left(\frac{z}{\delta}\right) \tag{2.3}$$

where different contributions can be noticed:

- $U^+ = \frac{1}{\kappa}\ln z^+ + C$ is the *"law of the wall"*, where κ is the von Karman constant ($\kappa \approx 0.41$ and C is a constant approximately equal to 5.1).
- ω is the *"wake function"* which shows how the modification due to the wake becomes relevant with increasing z; J. Hinze (1975) [33] approximated it as a sine-squared function:

$$\omega\left(\frac{z}{\delta}\right) = \frac{2\Pi(x)}{\kappa}\left(\sin\frac{\pi z}{2\delta}\right)^2 \tag{2.4}$$

- The Π function contains the free stream turbulence effect on the mean velocity and describes how well-developed the wake region is. It is dependant of the pressure gradient therefore it may vary along the streamwise direction x. Moreover, as explained by Marusic (2015) [34] it is possible to estimate the value of the Π function knowing the mean velocity profile from the inner layer up to the outer layer and by minimizing the function $f = U_{mean} - u^* \cdot U^+$, where $u^* = \sqrt{\tau_w/\rho}$ is the *"friction velocity"* and U^+ is computed with (2.3), see section 4.3

- z^+ is the *"wall units"* or *"plus units"* and it is commonly used to measure the distance from the wall by normalising the normal-wall coordinate with a near wall characteristic length scale δ_v, as follows: $z^+ = \frac{z}{\delta_v} = \frac{zu^*}{\nu}$

- ΔU^+ is the *"roughness function"* and takes into account the effect of the surface roughness on the mean velocity profile which causes the formation of a *"roughness sub-layer"* in the region very close to the wall and, consequently, a downward velocity shift to the log-law profile. As well-explained by Kadivar (2021) [12] different expressions for ΔU^+ have been proposed during the years as a result of both experimental and numerical work, however the general form proposed by J. Andersson (2020) [35] appears to be the most accurate for studying a wide variety of surface roughness

$$\Delta U^+ = \begin{cases} 0 & k_s^+ \leq k_{Smooth}^+ \\ \frac{1}{\kappa}\ln\left[C_s k_s^+\right] \cdot \sin\left(\frac{\pi}{2}\frac{\ln k_s^+ - \ln k_{Smooth}^+}{\ln k_{Rough}^+ - \ln k_{Smooth}^+}\right) & k_{Smooth}^+ < k_s^+ \leq k_{Rough}^+ \\ \frac{1}{\kappa}\ln\left[C_s k_s^+\right] & k_s^+ > k_{Rough}^+ \end{cases} \tag{2.5}$$

  the values proposed by Demirel et al. (2017) [36] by fitting the roughness function proposed by Schultz and Flack (2007) [37] have been used for the analysis explained in the next sections: $C_s = 0.26, k_{Smooth}^+ = 3$ and $k_{Rough}^+ = 15$. Moreover, $k_s^+ = \frac{u^* k_s}{\nu}$ is the *"roughness Reynolds number"*, where k_s is the *"equivalent sand-grain roughness height"* that is commonly used to describe the surface roughness while ν is the *"kinematic viscosity"*.

2.2.2 Convective boundary layer (CBL)

The Surface Layer and the entire Atmospheric Boundary Layer are described to be "unstable" or "convective" when the vertical heat flux measured at the Earth surface is positive (R_i negative, L finite and positive, and H/L positive), especially during the day. In general, the CBL develops from sunrise and lasts until sunset. It has a considerable

diurnal variability, growing from a few hundred meters in depth early in the morning to more than one kilometer in the afternoon (Jordi Vilà-Guerau de Arellano, 2015 [38]).

The turbulent flow in a CBL is driven by buoyancy, causing heat and moisture exchange in statically unstable conditions due to solar radiation absorption at the surface or cold air advection over warm surfaces (for instance sea ice edge). Light rising air from the surface organizes itself into thermal eddies (large convective structures), with diameters up to $1km$ and therefore, associated to integral length scales of the order of the ABL depth in the vertical direction. Thermals transfer moisture upward and are bordered by downward motions of dry air entrained from the free troposphere. These eddies combine air from the surface to the boundary layer's top, resulting in a well-mixed layer. As a result, quantities like heat, moisture, and atmospheric composition stay constant as a function of height, and the vertical gradient of these variables remains stable throughout time.

The CBL may be divided into four separate zones under these conditions: a *surface layer*, a *well-mixed layer*, an *inversion layer*, and a *residual layer* that merges into the free tropospheric layer ([38]). Considering Figure 2.4a, it is possible to notice as the mean velocity profile reveals a constant velocity zone where the flow is strongly mixed by the convective structure. This is followed by a steady *Inversion Layer* that marks the maximum height that the convective structure may reach. In the outer region of the ABL instead, the Coriolis force becomes negligible in comparison to convective effect, due to the interaction between the large scale motion and the upper part of the ABL.

2.2.3 Stable boundary layer (SBL)

When the vertical heat flux measured at the Earth surface is negative (Ri positive, L finite and negative and H/L negative), in particular during the night, the shear-driven turbulent flow exchanges in statically stable conditions, which are unfavorable to vertical motion: this is the "Stable ABL "configuration. Its depth can vary roughly in the range of $100 - 1000\ m$.

The SBL is usually generated because of the longwave cooling at the surface during the night or due to the advection of warm air over cold surfaces (for instance the interaction between warm sea and cold continent). Unlike in the CBL, the turbulent structures become smaller and do not couple anymore the high altitudes with the Surface Layer (see figure 2.4c). These small eddy structures causes a weak local mixing in the *surface layer* (which extends for approximately $100 - 300\ m$), since wind shear overcomes the negative buoyancy effect. Furthermore, Eddy diffusion is too weak to mix uniformly in the vertical direction either the potential temperature or any other scalar quantity (Xuhui Lee, 2018 [39]). In the high altitude layers, the friction term becomes less significant in the balance between pressure and Coriolis terms, therefore the wind velocity increases and a so-called *Low-Level Jet* is formed. At the same time, the lack of momentum at the surface is diffused upward by weaker and very localized turbulent exchange processes. Overall, the velocity profile is is characterized by a nearly constant shear topped by the Low-Level

Jet ([5], [40]).

2.3 The Ekman layer

In this section, a brief description of the Ekman Layer as well as of the Ekman's spiral is proposed following the steps presented by Holton (2012) [2]. This model tries to represent the full-depth ABL (up to the free-stream) which is what we aim to reproduce in the wind tunnel.
To make the analysis simpler, the special case of horizontally homogeneous turbulence above the roughness layer is considered. In this situation, the mean flow horizontal momentum equations are reduced to the following form [2]:

$$\frac{\overline{D}\overline{u}}{Dt} = -\frac{1}{\rho_0}\frac{\partial \overline{p}}{\partial x} + f\overline{v} - \frac{\partial \overline{u'w'}}{\partial z} \tag{2.6}$$

$$\frac{\overline{D}\overline{v}}{Dt} = -\frac{1}{\rho_0}\frac{\partial \overline{p}}{\partial y} + f\overline{u} - \frac{\partial \overline{v'w'}}{\partial z} \tag{2.7}$$

since it is possible to neglect the molecular viscosity and turbulent momentum flux divergence terms. The term $f = 2\Omega_{\oplus}\sin(\Phi)$ is the so-called *Coriolis parameter*. In general, a number of approximate semi-empirical method must be used to solve the equations (2.6) and (2.7), if the vertical distribution of the turbulent momentum flux is not known.
In the boundary layer the inertial accelerations terms (on the left hand side in (2.6) and (2.7)) are small compared to the Coriolis force and pressure gradient force terms, but the turbulent flux terms must be included. Thus, to a first approximation, planetary boundary layer equations define a three-way balance among the Coriolis force, the pressure gradient force, and the turbulent momentum flux divergence. It is also possible to introduce the *geostrophic relationship*, that can be expressed as a first approximation as:

$$-fv_g \approx -\frac{1}{\rho}\frac{\partial p}{\partial x}; \quad -fu_g \approx -\frac{1}{\rho}\frac{\partial p}{\partial y} \tag{2.8}$$

where $\mathbf{V}_g = \mathbf{e}_x \cdot u_g + \mathbf{e}_y \cdot v_g$ is the *geostrophic wind*. Therefore, the momentum equations can be simplified as follows:

$$f\left(\overline{v} - \overline{v}_g\right) - \frac{\partial \overline{u'w'}}{\partial z} = 0 \tag{2.9}$$

$$-f\left(\overline{u} - \overline{u}_g\right) - \frac{\partial \overline{u'w'}}{\partial z} = 0 \tag{2.10}$$

In order to obtain closed equations, the turbulent momentum flux divergence must be expressed in terms of mean variables. One of the most used closure scheme is the so-called *the Flux-Gradient theory* or *K theory*, in which the turbulent eddies are assumed to act similarly to molecular diffusion so that the field's flux is proportional to the local gradient

of the mean.The turbulent flux terms can be expressed as follows under this assumption:

$$\overline{u'w'} = -K_m \left(\frac{\partial \overline{u}}{\partial z}\right); \quad \overline{v'w'} = -K_m \left(\frac{\partial \overline{v}}{\partial z}\right) \tag{2.11}$$

where $K_m(m^2 s^{-1})$ is the *eddy viscosity* coefficient.

By using the aforementioned closure scheme and by assuming the value of K_m to be constant, the equations (2.9) and (2.10) can be reduced to the *classical Ekman layer* equations:

$$K_m \frac{\partial^2 u}{\partial z^2} + f\,(v - v_g) = 0 \tag{2.12}$$

$$K_m \frac{\partial^2 v}{\partial z^2} + f\,(u - u_g) = 0 \tag{2.13}$$

The overbars have been removed because all fields are Reynolds-averaged. The equations (2.12) and (2.13) are assumed to be valid throughout the entire boundary layer's height to simplify the study.

To solve the equations, we have to introduce the boundary conditions on u and v:

$$u = 0, v = 0 \quad as\ z = 0$$

$$u \to u_g, v \to v_g \quad as\ z \to \infty$$

Indeed, it is reasonable that the horizontal velocity components are zero at the ground (for the no-slip condition), while they approach their geostrophic values at high altitudes. Then, it is possible to reduce the equations (2.12) and (2.13) to a second-order equation in complex velocity $(u + iv)$ by multiplying the second equation by $i = \sqrt{-1}$ and adding the result to the first equation. The following is the resultant relationship:

$$K_m \frac{\partial^2 (u + iv)}{\partial z^2} - if(u + iv) = -if(u_g + iv_g) \tag{2.14}$$

The single equation admits solution. To make the analysis easier, the geostrophic wind is assumed to have no height dependence and to be oriented in the zonal direction (i.e., $v_g = 0$). The problem's general solution is:

$$(u + iv) = A \cdot exp\left[(if/K_m)^{1/2} z\right] + B \cdot exp\left[-(if/K_m)^{1/2} z\right] + u_g \tag{2.15}$$

Introducing the boundary conditions and the relationship $\sqrt{i} = (i + 1)/\sqrt{2}$ and considering the Northern Hemisphere (where $f > 0$):

$$u + iv = -u_g \cdot exp[-\gamma(1 + i)z] + u_g \tag{2.16}$$

where $\gamma = (f/2K_m)^{1/2}$.

Then, applying the Euler relation $e^{-i\theta} = \cos\theta - i \sin\theta$ and separating the real and the

imaginary parts, the *Ekman spiral* solution is obtained for the Northern Hemisphere:

$$u = u_g \left(1 - e^{-\gamma z} \cos \gamma z\right), \quad v = u_g e^{-\gamma z} \sin \gamma z \tag{2.17}$$

Because of its structure, the solution is best illustrated by a hodograph, showing the Geostrophic wind direction in the x-axis plotted as a function of height (see figure 2.6a). In the same plot, the velocities for different values of γz are indicated by arrows. When $z = \pi/\gamma$ the wind is approximately parallel to the geostrophic value. Therefore, the convention is to define the Ekman layer depth as $\delta_e = \pi/\gamma$.

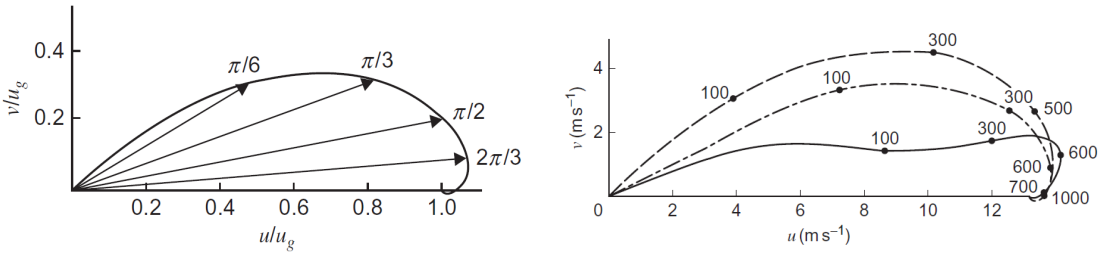

(a) Hodograph of wind components in the Ekman spiral solution

(b) Mean wind hodograph for Jacksonville, Florida ($\approx 30°N$), April 4, 1968 (solid line) compared with the Ekman spiral (dashed line) and the modified Ekman spiral (dash-dot line) computed with $\delta_e \approx 1200m$. Heights are shown in meters.

Figure 2.6: Normalized hodograph for the Ekman spiral solution and mean wind hodograph for modified Ekman spiral solution. Both the figures are from Holton (2012) [2].

As already explained, the most important information given by the Ekman layer solution is that the boundary layer wind is directed toward lower pressure due to the balance of forces acting in the atmosphere.

It is important to mention that the ideal Ekman layer is almost never observed in reality and this is mainly because of two main reasons:

- Turbulent momentum fluxes are not simply proportional to the gradient of the mean momentum in most applications;
- The assumption of a constant eddy viscosity coefficient is not realistic since K_m varies rapidly with height in the Surface Layer (where the Ekman layer solution is not valid anymore).

For these reasons, a *Modified Ekman Layer* is introduced combining the logarithmic surface layer (subsection 2.2.1) and the Ekman spiral, leading to a fit closer to observations. However, this model tends to overestimate the angle between the boundary layer wind and the geostrophic wind, as shown in Figure 2.6b. The reason for this is that in a neutrally buoyant atmosphere, the Ekman layer is often unstable, resulting in enormous circulations that transport significant amounts of momentum vertically (subsection 2.2.2).

2.4 Atmospheric Boundary Layer models

Several empirical descriptions of the ABL's various features (mean velocity profile, temperature, turbulent intensity, integral length scales, turbulent spectrum, and so on) were proposed based on the requirements of the scientific community. Without going into too much detail, it is worth to mention some of the parameterizations proposed during the years in the literature:

- The ESDU report 85020 (1985) [7], first dedicated to engineers.
- The book written by Kaimal & Finnigan (1994) [5], "Atmospheric Boundary Layer Flows: Their Structure and Measurement". The book discusses accurately the physical phenomena which characterize a real ABL. It examines the complementary aspects contributed to the Monin & Obukhov (1954) [4] similiarity theory by many observations in the second half of the twentieth century, leading to the "Businger-Dyer Flux-Profile" [41] relations and their corrections.
- The Eurocode (2005) report [42], one of the most used by civil engineers. Exactly like the EDSU report, it can be used as a reference fot the description of a neutral ABL.

These descriptions are mostly for equilibrium ABL, which means that all forcings are supposed to evolve considerably slower than the ABL's reaction time (the time scale threshold is set at around 1 hour by Stull, 1988 [14]). These three configurations ignore the ABL's "out-of-equilibrium" features, which are relevant at full scale (e.g. the diurnal cycle [14]).

2.5 Study of the Atmospheric Boundary Layer in the wind tunnel

The considerable complexity of the ABL structure arises from the brief discussion of its fundamental properties presented in the preceding sections. This explains the extensive experimental and theoretical research into the ABL during the last fifty years. Furthermore, due to the multiple potential configurations, the full reproduction of an ABL configuration in the wind tunnel appears to be quite challenging. In particular, Cermak & Arya (1970) [43] pointed out that the temperature stratification and non-uniformities (and high irregularities) of the Earth surface are the two most difficult components of the atmospheric boundary layer to reproduce in a wind tunnel. Moreover, it is almost impossible to simulate the Coriolis forces, and consequently the Ekman layer, since a rotating facility would be necessary. At the same time, experimental data are crucial for understanding the phenomenon, and the only way to obtain them in a conventional wind tunnel is to simplify the studied flow by limiting the considered flow's characteristics to the application in

question (Armitt & Counihan, 1968 [44]), while maintaining as much relevant similarity criteria as possible.

2.5.1 Similarity conditions for the generation of an ABL in wind tunnel

The similarity criteria provide the necessary parameters for a wind tunnel flow to be identical to a full-scale Atmospheric Boundary Layer flow. These criteria were obtained from the atmospheric motion equations for three distinct scales (related with different approximations) of the atmosphere by Cermak (1971) [20] and Avissar (1990) [45]. Instead of evaluating scenes with horizontal typical length scales of 10-100 km (meso-scale atmosphere case) or scenes with horizontal typical length scales of a few kilometres (small-scales atmosphere case), our representation considers situations with virtually planar and uniform terrain roughness (micro-scales atmosphere). The small-scales example might be thought of as a refined version of a less general arrangement (as it depends on each considered topography).

According to Cermak (1971) [20], Cermak (1975) [46] and Avissar (1990) [45], the similarity criteria can be classified in three main types:

- **The geometric similarity**, which requires that for all length scales of the analyzed configuration, the same scaling ratio S between full-size and wind tunnel scale must be maintained;
- **The dynamic similarity**, associated to the conservation of several non-dimensional parameters, in particular:
  - The **Rossby number**, $R_0 = \frac{U_0}{\Omega L_0}$, where U_0 is a representative velocity, L_0 is a length scale of interest and $\Omega_0 = 2\Omega_{\oplus} sin(\Phi)$ is the so-called *Coriolis parameter* (with $\Omega_{\oplus}$ being the Earth's rotation velocity and Φ the latitude of the considered location). This is a crucial quantity in the theoretical analysis of an Atmospheric Boundary Layer because it allows you to examine the effects of inertia and Coriolis forces on turbulent flow. However, a large rotating facility would be required to adequately reproduce this number in the wind tunnel, hence this parameter is normally ignored in ABL experimental research. This implies that the Ekman boundary layer's outer region (where the mean flow changes direction according to the "Ekman spiral") cannot be fully replicated. In this paper, a full-depth Atmospheric Boundary Layer will be reproduced in the wind tunnel neglecting the Coriolis forces' effect, which may result in some deviations from the actual world. On the other hand, the Coriolis effect has no effect on the Surface Layer, if the full-scale configuration is considered on timescales relatively small compared to the duration of the day (e.g. $< 6h$). Therefore, the Surface Layer can be fully reproduced in the wind tunnel.

- The **Reynolds number**, $Re = \frac{U_0 L_0}{\nu_0}$ with ν_0 a representative air kinematic viscosity. It represents the ratio between inertia and viscous forces. In the full-scale Surface Layer, it is possible to reach very high Reynolds numbers, of the order of $\sim 10^8 - 10^9$ which are very difficult to obtain in wind tunnels. Usually, this is not a problem because the main flow's properties become independent of Reynolds number when the latter is sufficiently high [46]. However, there are two quantities which always depend on the Reynolds number. The first one is the flow inside the viscous sublayer of boundary layers. However, in the case of "aerodynamically rough surface", defined empirically as $(u_* h_0^r)/\nu > 2.5$ ([47] [46] [45]), the presence of viscous sublayers can be ignored since it develops only on very smooth surfaces. This is always true in the atmosphere, therefore this regime should be achieved on the modeled surface in the wind tunnel. The second characteristics which is always dependant of Reynolds number concerns the small scales of turbulence. The turbulent inertial range, as defined by Kolmogorov's (1941) theory [48], will not be sufficiently wide for a lower Reynolds number in the wind tunnel than in the atmosphere. This means that the Taylor and Kolmogorov microscales won't be small enough in comparison to their full-scale counterparts. At the very least, the Reynolds number of the wind tunnel should be designed to propagate the inertial range of the turbulent spectrum up to small enough scales to encompass the frequencies (or wavenumbers) of importance for the applications under consideration ([44] [49]).
- The bulk **Richardson number** $Ri_B = \frac{g L_0 \Delta T_0}{T_0 U_0^2}$ with g the gravitational acceleration, ΔT_0 the vertical temperature variation, T_0 a representative potential temperature at the considered altitude. It quantifies the competition between shear and thermal convection. This parameter is linked to the Richardson number, which was previously discussed and introduced in [25]. It may be replicated in highly specialised wind tunnels with heating and cooling systems. The only conceivable value for Ri_B in a classical aerodynamics wind tunnel is 0, which corresponds to a neutral ABL.
- The **Prandtl number** $Pr = \frac{\nu_0}{\kappa_0}$ with κ a representative air thermal diffusivity. It is automatically the same when the same fluid is used between model and full scale;

- **The boundary conditions** in the wind tunnel have to be identical to those in the real world. These boundary characteristics can be listed as follows:
  - The surface roughness. Ideally, the roughness geometry in the wind tunnel should be identical to the reality, but Jensen & Franck (1963) [50] has shown that, to reproduce the effective flow field, it is sufficient to conserve at least the Jensen number, $Je = \frac{L_0}{h_0^r}$ where h_0^r is the roughness height defined by the equation (2.2). The displacement height d scaling isn't necessary in similarity

criterion because it is simply used to define the origin of the altitudes. Moreover, as already presented for the Reynolds number similarity just above, the surface should be "aerodynamically" rough: $(u_* h_0^r)/\nu > 2.5$ [47] [46] [45].

- The surface temperature distribution: it is achieved in special wind tunnels with heating and cooling systems [20];
- The upstream distribution of temperature: it is also achieved in specific wind tunnels with heating/cooling devices (such as upstream heated grids) [20];
- The upstream Atmospheric Boundary Layer flow: this is exactly the condition that justifies the design of an Atmospheric Boundary Layer in a wind tunnel, because it can then be used to generate an incoming flow for a variety of applications involving atmospheric flows, including civil engineering, wind turbines, marine engineering, pollutant dispersal, and meteorological research.

2.5.2 The relevant ABL characteristics for engineering applications

Before starting any investigation, it is crucial to understand which ABL's characteristics must be reproduced in the wind tunnel, in order to get useful data for engineering purposes, in particular wind engineering. Armitt & Counihan (1968) [44] provide specifics about the fundamental quantities of the ABL that should be recreated in a wind tunnel for most applications within the constraints set by the prior similarity criteria. After that, Cermak (1999) [49] refers to a similar list:

- The mean velocity profiles: $\overline{u}(z)$, $\overline{v}(z)$ and $\overline{w}(z)$
- The turbulent intensity computed in the three directions:

$$I_u(z) = \frac{\sqrt{\langle u'^2 \rangle}}{\overline{u}}$$
$$I_v(z) = \frac{\sqrt{\langle v'^2 \rangle}}{\overline{u}}$$
$$I_w(z) = \frac{\sqrt{\langle w'^2 \rangle}}{\overline{u}}$$

- The turbulent characteristic length scales, especially the integral length scales which can be defined through the correlations of the velocity components:

$$L_{u_i u_j, x_k}(\underline{x}) = \int_0^{+\infty} \frac{\langle u_i'(\underline{x}) u_j'(\underline{x} + \Delta x_k \underline{e}_k) \rangle}{\sqrt{\langle {u_i}'^2(\underline{x}) \rangle} \sqrt{\langle {u_j}'^2(\underline{x} + \Delta x_k \underline{e}_k) \rangle}} \mathrm{d}\Delta x_k$$

The cases where $i = j$ are of particular interest. These integral length scales can be ranked in order of importance, as follows: $L_{uu,x}$, $L_{ww,x}$, $L_{uu,z}$, $L_{ww,z}$, $L_{uu,y}$, $L_{ww,y}$, $L_{vv,x}$, $L_{vv,z}$, and $L_{vv,y}$.

- The Reynolds stress tensor $R_{ij} = \left\langle u_i' u_j' \right\rangle$, which measures the exchange of energy between mean and fluctuating motions.

2.5.3 Devices and methods for ABL generation

The studies by Jensen & Franck (1963) [50], Davenport & Isyumov (1967) [51] and Cermak & Arya (1970) [43] proved that it is possible to successfully reproduce an ABL in the wind tunnel. They used a long roughness fetch scaled down in order to conserve the Jensen number [50], defined as $Je = D/h_0^r$, with D being a characteristic length scale (usually the boundary layer height) and h_0^r the roughness length. The main drawback of their approach, however, was the requirement for an excessively long wind tunnel (on the range of $25 - 30$ times the depth of the desired boundary layer). Davenport & Isyumov (1967) [51] were able to expand the section of well-developed boundary layer by adding a downstream grid, partially covering the section, and thereby lowering the development length to around 16.5 times the boundary layer thickness in a wind tunnel like this. In particular, they studied two different configurations of roughness terrain: one representing rural roughness ("Open country" with a value of $\alpha = 0.16$) and one representing urban roughness ("Urban region" with a value of $\alpha = 0.36$). As expected, the shear and the turbulent intensity increase with the surface roughness, especially in the region close to the wall. Two definitions of turbulent intensity are provided: the first one is based on the local velocity $\overline{u}(z)$, while the other one depends on the velocity measured outside of the boundary layer U_g. Their experimental findings differ according to the conventions used for this computation, hence the convention has to be specified each time. Considering the work of Davenport & Isyumov (1967) [51], the turbulence intensity that should be representative of an ABL appears to be around 12% in rural areas and 32% in urban areas, when normalized by the local mean velocity. Finally, by analyzing the normalized energy spectra, they noticed an increase in magnitude of the turbulent structure at the energy peak when the roughness is higher.

A wide range of devices were proposed to further reduce the length of the required wind tunnels (which reached the value of 16.5 times the boundary layer's depth with Dasenport & Isyumov 1967 [51]). A considerable number of these recommendations are described by Hunt & Fernholz (1975) report of the Euromech 50 conference [53], which exposes the attempts, successful or not, from the period when ABL creation in wind tunnels was a very active domain. The following are some of the most important techniques that have emerged from these investigations.

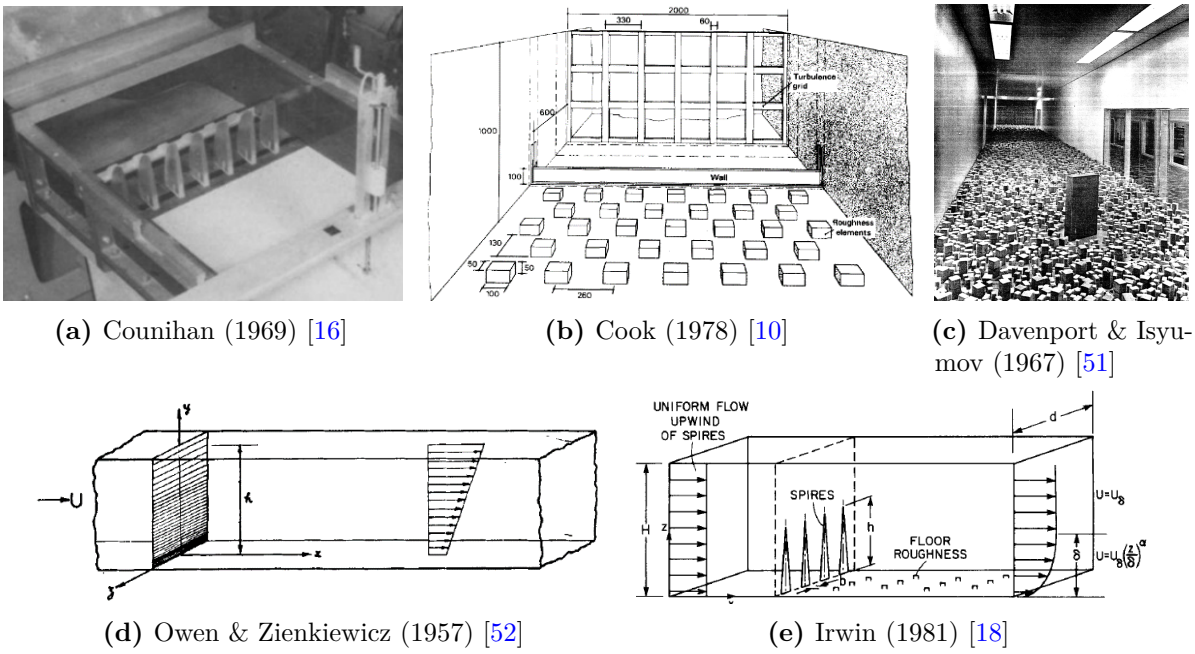

(a) Counihan (1969) [16] **(b)** Cook (1978) [10] **(c)** Davenport & Isyumov (1967) [51]

(d) Owen & Zienkiewicz (1957) [52] **(e)** Irwin (1981) [18]

Figure 2.7: Various devices that were studied in order to reproduce (at least partially) the characteristics of a neutral ABL.

2.5.3.1 Combination "Roughness-Barrier-Mixing devices "

This expression (derived by [10]) encompasses a wide range of methods based on the same approach described by Cook (1978) [10]: the use of vortex generators, downstream of the wind tunnel section of interest, allows for the creation of a mixed layer in which the turbulent kinetic energy generated near roughness components on the floor is transferred upward. J. Armitt and J. Counihan [44] showed that this technique artificially increases the boundary layer's depth. These Reynolds stresses encourage kinetic energy generation at the expense of mean flow, which is now approaching the mean flow of a boundary layer [44]. Then, a vertical barrier can be added in the vicinity of the wall surface, either upstream ([16], Figure 2.7a) or downstream ([10], Figure 2.7b) of the vortex generators, increasing the defect of mean velocity close to the wall. With mixing, this velocity defect expands over the whole boundary layer [10]. In combination with the Reynolds stress, the related vertical shear contributes to the generation of turbulence.

Several devices that fulfill this qualitative scenario have been presented, assuming diverse shapes based on each experimentalist's intuitions and tries [10]. Without being exhaustive, some of them are listed:

- **Counihan (1969)**: [16], based on the observations from Armitt (1966) [54] and Armitt & Counihan (1968) [44], proposed the use of vortex generators in the shape of elliptical quarters besides a upstream barrier and roughness surface downstream (Figure 2.7a). The research focused on the usage of a castellated barrier, with a higher height in the alignment of the vortex generators, rather than keeping a constant height barrier. Indeed, the turbulence produced by vortex generators tends

to accelerate the mean flow due to mixing of momentum from upward [10], requiring a larger velocity defect in the regions very close to the vortex generators. This combination was very successful, and two configurations were proposed ("Open rural" [16] and "Built-up area" [55]) that accurately reproduces the mean flow profile and turbulent intensity profile while also generating integral lengthscales equivalent to the full scale ABL with the same altitude trend (data only for the urban scenario in 1973 [55]). In both cases, the Reynolds stress profile indicates a thick layer where the Reynolds stress is nearly constant (or decrease slowly with altitude). This feature describes the ABL's Surface Layer, which contains the logarithmic law. The boundary layers reproduced by Counihan (1969) [16] and Counihan (1973) [55] are fully developed after a distance of 4.5 times the height of the boundary layer from the trailing edge of the vortex generators. This device has had a lot of success in wind tunnels for ABL replication, allowing to reduce the length of the test sections. The Counihan method is still in usage nowadays (Kozmar (2010) [56], Kozmar (2011) [19] with an extended range of achievable flows). In particular, Kozmar [19] studied three different ABL configurations (power law exponents from $\alpha = 0.16$ up to $\alpha = 0.36$), achieving results representative of a neutral ABL in terms of mean flow and turbulent intensity profiles. Although the integral length scales have the correct order of magnitude, their profile does not correspond to atmospheric trends;

- **Cook (1973)** [57], and then **Cook (1978)** [10], have replaced the use of vortex generators by a uniform grid with square mesh (Figure 2.7b), designed to provide a specified velocity spectrum at high turbulence scales (but the conception method does not seem to be explicited). This adjustment, in particular, allows a fraction of the full-depth ABL to be generated in the wind tunnel (the first third of the ABL). The results are similar to the ones by Counihan (1973) [55] for a "urban" configuration. However, in this method the required development length is reduced to 4 times the depth of the partially simulated boundary layer (here the height of the wind tunnel);

- **Irwin (1981)** [18], based on Campbell & Standen (1969) [58], Standen (1972) [59] and Irwin (1979) [60], adopted a series of triangular barriers (referred to as "spires") in place of both the vortex generators and the barrier at the same time (Figure 2.7e). In order to fully design the spires-roughness device for a specified power law mean velocity profile (see the power law in equation (2.1)), quantitative relations are explicitly provided. This was not the case for the other devices presented above, which were designed to be used with particular flow configurations and did not require to be adapted to different configurations. Although the authors claim that the resultant turbulent intensity profile appears to be close to neutral ABL conditions, the Irwin technique only controls the mean flow profile and does not govern the turbulent intensity profile. The flow characteristics achieve a satisfactory lateral

homogeneity after a streamwise distance of about 6 boundary layer thickness from the spires [18]. Irwin was able to reproduce mean flow and turbulent intensity profiles representative of the neutral ABL, as well as integral length scales of the correct order of magnitude compared to those in the real atmosphere.

2.5.3.2 Passive grids over the whole wind tunnel section

The use of grids, which fill the whole wind tunnel section, to tune incoming flow characteristics was initially examined in a situation not related to ABL subjects, such as by Owen & Zienkiewicz (1957) [52]. They achieved a uniform mean shear flow by using an array of parallel circular rods that were not equally spaced in the flow's transverse direction. (as shown in Figure 2.7d). Rose (1966) [61] extended this work by establishing that the local blockage ratio of such grid devices should not exceed a defined threshold, over which the flow regime shifts from wakes-interacting to jets-interacting (referring to a remark by Corrsin 1963 [62]). The works by Elder (1959) [63] and McCarthy (1964) [21] have suggested theoretical quantitative relations that make possible to conceive, a priori, such grid devices for a prescribed mean flow. The lack of a comparable theory for predicting turbulent intensity, as well as the low turbulent intensity obtained, appear to be the two main reasons for the community's growing disinterest in only grid-based ABL reproduction (Armitt & Counihan 1968 [44], Cook 1978 [10]). Recent works on grids with specific geometries (introduced by [11]) may lead to a questioning of these conclusions since they may enable an independent control of mean flow and turbulent intensity. Such devices are the starting point for the research carried out by Thomas Huret within his PhD project and during this internship.

2.5.3.3 Thermal stratification in wind tunnel

Several experimentalists have examined techniques to recreate distinct thermal stratification situations (stable or unstable) in dedicated meteorological wind tunnels by generating thermal forcings, in addition to the various neutral-ABL production devices described above (see for instance [20]). The installation of heated or cooled walls and downstream grids in the wind tunnel allows for the creation of the desired temperature gradient, despite the fact that this arrangement is far more complex to construct and manage than neutral ABL devices.

2.5.4 The remaining difficulties in the reproduction of ABL characteristics in wind tunnel

The majority of the techniques described in the previous section may be used to recreate a realistic mean flow profile and longitudinal turbulence intensity for specified configurations

(such as "rural" or "urban" flow). However, they experience three key issues in their applications:

- These configurations were created by trial-and-error, and extending them to other predefined scenarios without reverting to trial-and-error methods remains challenging. This was remarked by Cook (1978) [10], who evaluated his device's sensitivity to the height of the barrier in order to produce a slight variation in the flow produced. Figure 2.8 shows the results of the turbulent intensity profiles and integral length scales. Even though the studied range of roughness is modest compared to the large range of effective roughness described in the classifications of Figure 2.5, these results allow for a preliminary design of the Counihan-type turbulence producing device. Here the roughness range is representative of "urban flows";

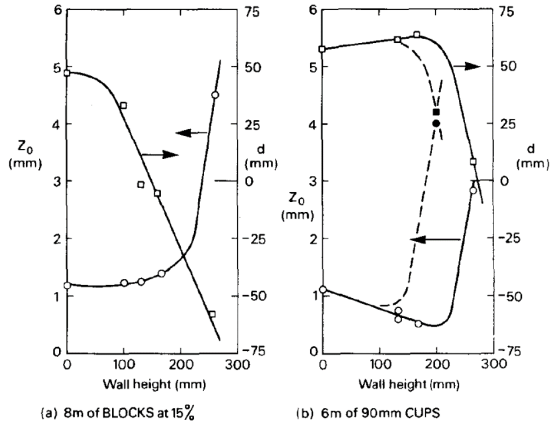

(a) The effective roughness height h_0^r and displacement height d as a function of the barrier height as measured by Cook (1978) [10] for two different roughness scenarios: (left) a 8 m fetch of cubes with a surface density of 15%, (right) a 6 m fetch of 90-mm high reversed cups.

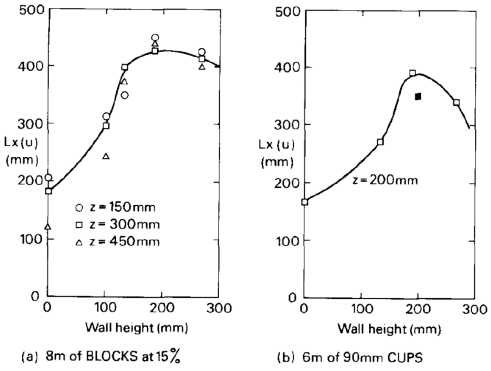

(b) The maximum-energy containing length scale (computed after fitting measured energy spectrum) as a function of the barrier height as measured by Cook (1978) [10].

Figure 2.8: Sensitivity analyses by Cook (1978) [10] for the roughness characteristics and the energy-containing scales as a function of the barrier height for two different roughness scenarios: (left) a 8 m fetch of cubes with a surface density of 15%, (right) a 6 m fetch of 90-mm high reversed cups. The employed wind tunnel facility is 1-meter high (representing one third of the simulated ABL).

- The majority of the producing devices are built for thermally neutral situations, which is a rather unusual condition in nature. Indeed, it is only representative of the ABL when shear dominates over thermal effects, therefore it is mostly observed during long-term cloudy weather, especially over seas, or during storms with substantially greater wind speeds than the typical situations. The diurnal cycle, on the other hand, causes the ABL to deal with a constantly fluctuating and non-negligible heat flow for the majority of the time [14] [64]. It is a source of non-equilibrium behavior (which is outside the scope of our investigation) as well as a suitable environment for

stable and unstable quasi-equilibrium configurations. These dominant configurations' properties are not replicated by the above-mentioned short wind tunnel devices.

- Finally, the ABL generation devices described above do not fully reproduce the Integral Length Scales profiles of the full-scale ABL. This is clearly showed for instance by Kozmar (2011) [19] for Counihan-type methods. The resulting integral lengths scales have an adequate order of magnitude, but do not follow the correct profiles. It was already noticed by previous experimentalists, such as Farell & Iyengar (1999) [65], Varshney & Poddar (2011) [66] and recently by Du *et al.* (2020) [67].

The PhD project of Thomas Huret attempts to solve at least some of these three issues. The PhD project focuses primarily on the Surface Layer of a neutral ABL, with the goal of reproducing and controlling both the mean velocity and turbulence intensity profile of this region of the Atmospheric Boundary Layer independently, inspired by the promising results of Zheng *et al.* (2018) [11].

My internship project, on the other hand, was planned to investigate the potential of controlling the mean velocity profile of a full-depth atmospheric boundary layer using partial and full-section grids in parallel, applying the same methodologies. To do so, the interaction between free-stream turbulent flow and grid-produced boundary layers must be investigated, particularly for partial grids where a mixing layer forms between the grid's top part and the upper section.

Chapter 3

Theoretical and experimental methods

This chapter describes briefly the tool used to reproduce a full-depth atmospheric boundary layer (ABL) in a wind tunnel. The chapter's first section, in particular, focuses on the experimental facility's presentation and the measuring methods applied for the projects. Instead, in the second section, attention is put on the Multiscale Inhomogeneous Grids (MIG) applied to replicate the ABL in the available wind tunnel. Finally, a brief explanation of the theoretical model which relates the grids' geometry to the produced mean velocity profile is given.

3.1 The main experimental setup

In order to better understand how the experimental investigation of the Atmospheric Boundary Layer is carried out during the project, a brief description of the experimental facilities and instrumentation will be provided in this section. Moreover, the measurement techniques used to capture the flow field's properties will be discussed, together with calibration techniques for different methods and devices.

3.1.1 The wind tunnel

It is worth noting that the experiments for my internship project at Onera center in Lille were conducted in the same wind tunnel but with two configurations. Although the majority of the results that will be presented in the paper were obtained in the new setup, which was specifically designed to perform grid experiments, in the following sections the two configurations will be described highlighting the differences.

3.1.1.1 The old configuration of the SCL-PIV wind tunnel

The SCL-PIV ("Soufflerie de Couche Limite" - Particle Image Velocimetry) is an open circuit wind tunnel from the ONERA center at Lille (France): a schematic representation

of the wind tunnel is presented in figure 3.1a taken from [68]. It consists in a closed $H \times W = 0.29\ m \times 0.3\ m$ test section where the flow is sucked from the wind tunnel room by a downstream centrifugal fan. After passing via a seeding device and a honeycomb that reduces entering turbulence, the incoming flow reaches the test section through a convergent. After passing through the fan, the downstream flow is expelled outside. In comparison to air pressure, the wind tunnel causes a depression in the surrounding chamber. The operational velocity range of the wind tunnel is between 10 m/s and 30 m/s. However, all the results that will be presented in the next chapters are obtained for a velocity $U_{pitot} = 15\ m/s$, which leads to a global Reynolds number $\mathcal{R} = \frac{U_{pitot} H}{\nu} \approx 2.78 \times 10^5$.

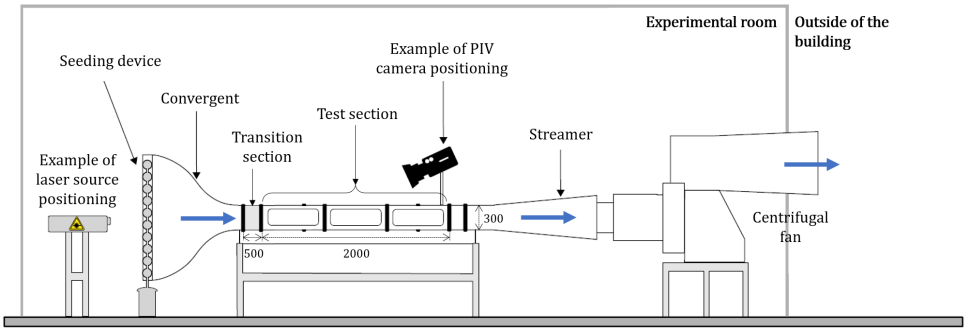

(a) Scheme of the wind tunnel. Length unit: *mm*. Source: Ott (2019) [68].

(b) Entrance of the convergent with the seeding device.

(c) The wind tunnel test section.

Figure 3.1: The SCL-PIV wind tunnel at the ONERA center in Lille

Particle Image Velocimetry (PIV) or other optical measures such as Laser Doppler Velocimetry (LDV) can be used to examine the turbulent boundary layer in the wind tunnel. However, in the current project the optical measures are not used. The flow's properties are measured only using the Hot Wire Anemometry (HWA) technique. The main wind tunnel components are shown in Figure 3.1 and can be listed as follows:

- A particle release device, consisting of a mesh of perforated tubes, is inserted upstream of the contraction (Figure 3.1b);
- The wind tunnel test section is divided in three parts with modular wall panels: transparent glass, perforated slots for probe insertion or opaque material. In this way it is possible to perform measurement with both PIV and Hot Wire Anemometry (HWA) techniques;

- A $10mm$ thick aluminium plate covers one of the wind tunnel's lateral walls, allowing researchers to observe boundary layer evolution on a flat surface over the whole test section. Before reaching its full thickness in the test section, it is bevelled at the transition section. Because it is less affected by surface imperfections than the other three walls, this plate has been used to represent the Earth surface in Atmospheric Boundary Layer investigations;
- A 3D traverse system specialised to probe installation and flow profile measurements;
- The seeds are not accumulated in the wind tunnel chamber because the downstream flow is expelled outside of the structure.

3.1.1.2 The new configuration of the SCL-PIV wind tunnel

The SCL-PIV wind tunnel has been modified and adapted to our requirements about one month after the beginning of the internship. The main modification was the insertion of a new wind tunnel segment between the transition and the test sections. This new part presents a removable panel for the insertion of the 3D printed grid through two slots ($15mm$ wide and $5mm$ depth) that also holds the grid itself avoiding vibrations (see Figure 3.2a).

This upgrade brought some interesting advantages:

- It efficiently maintains the grid's location in the operating wind tunnel. This ensures repeatability of the experiments and reduces the human error;
- It allows for the quick insertion and removal of 3D printed grids with minimal handling and, at the same time, the access from both sides of the grid (see Figure 3.5c);
- The system does not obstruct incoming flow since it is flush with the wall when installed, causing no disturbances to the smooth aluminium plate wall (standing for the Earth surface), as shown in Figure 3.2b.

The second update in the wind tunnel is the honeycomb in the converging section, indeed the previous one included a square hole for the insertion of a laser that was formerly employed for PIV measurements but is no longer in use.

The new SCL-PIV configuration maintains the same structure as the previous one, but with a longer transition section that is helpful not only for the quick insertion and removal of the grid, but also to improve the flow quality. In Figure 3.3, it is possible to notice that the wind tunnel is particularly flexible since it is accessible through three separate "windows" that can be closed using different panels, allowing the Hot Wire Anemometry (HWA) probe to be inserted in the test section and to measure the velocity's profiles in the three directions and at several streamwise locations. In particular it is possible to obtain three different profiles:

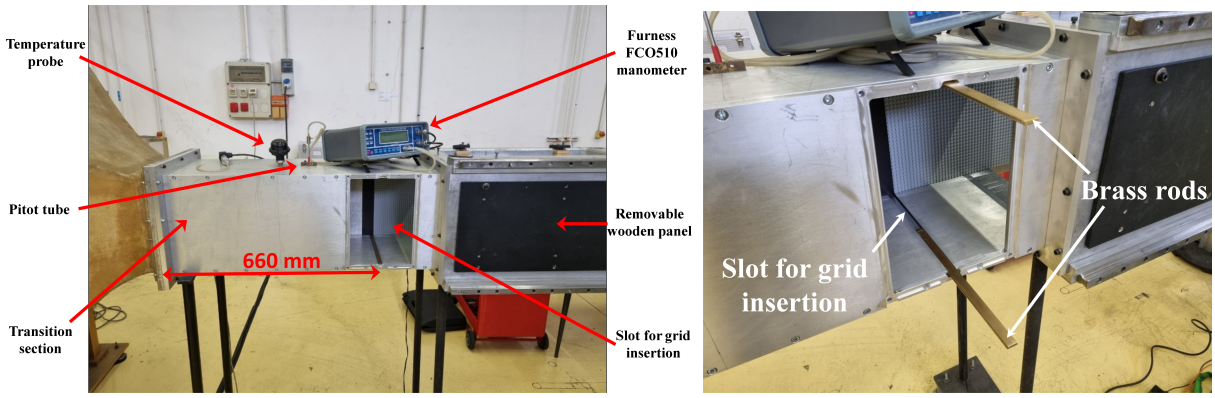

(a) The new wind tunnel transition section with the removable panel.

(b) Open panel with brass rods that keep the surfaces flush preventing uncontrolled turbulence generation.

Figure 3.2: New wind tunnel transition section with drawer.

- **Vertical profile**: the velocity evolution is measured moving the HWA along the z direction, perpendicular to the smooth wall, in order to obtain information about the boundary layer generated in the wind tunnel. This is the most important profile for the project purpose and it is usually measured by using the panel which presents 9 vertical slots (Figure 3.4b), which is sealed off thanks to the 3D printed "covers" (Figure 3.4c) and which allows to obtain information at different y positions;

- **Longitudinal profile**: the velocity evolution is measured moving the HWA along the x direction, which is the streamwise direction in which the air is flowing. This profile can be only measured using the panel with a long horizontal slot in the middle (shown in Figure 3.4a) and it can provide interesting information about the evolution of the turbulent intensity and integral length scales in the streamwise direction. Brushes and rubbers are inserted in the slot to limit air penetration (which might result in a jet in the z direction). The rubber was eventually removed since it had a strong resistance to the 3D traverse mechanism and did not appear to affect the flow;

- **Transverse profile**: the velocity evolution is measured moving the HWA in the y direction. This profile gives information about the symmetry of the velocity field along the y direction and it require the use of the panel with vertical slots.

3.1.2 The Hot Wire Anemometry (HWA)

The variables occurring in turbulent flows, such as mean and fluctuating velocity components, mean and fluctuating temperature, and so on, can be measured using hot-wire and hot-film anemometers. Thin metallic components are heated by an electric current (Joule effect) and cooled by the incident flow, which acts due to its mass flux and temperature (through various effects, but with forced convection usually predominant). It is thus

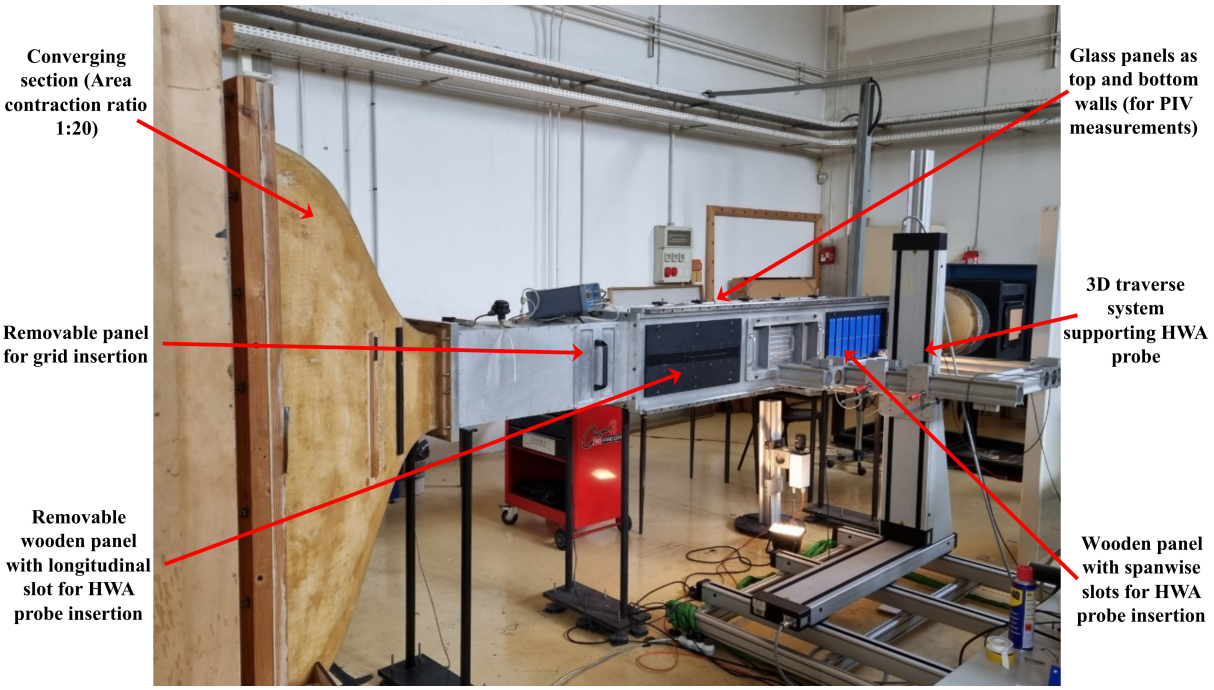

Figure 3.3: New wind tunnel configuration. From left to right, the first panel is used for measuring streamwise velocity profiles, the second panel works as "wall" and the third one allows to measure spanwise and normal-wall profiles at nine different streamwise positions.

feasible to extrapolate information about the flow from the temperature (or resistance) achieved by the sensor (Comte-Bellot G., 1976 [69]). However, this is an intrusive measurement technique wherein a probe is introduced into the fluid stream to be measured. To adequately analyse a turbulence field, more than one sensor or more than one value of the heating current is sometimes required. As a result, multi-wire probes were developed, allowing for the measurement of two or even three velocity components (3D Hot Wire Anemometry), whereas Single Hot Wire Anemometry (S-HWA) could only detect the velocity component in the streamwise direction.

In our analysis only the Single Hot Wire Anemometer (S-HWA) and the Cross Hot Wire Anemometer (X-HWA) will be used. Both are constant temperature anemometers (CTA), where the electrical circuitry's purpose is to keep the sensor's temperature constant when heat is convected from it to the fluid flow. From the calibration of the hot-wire probe, a link between the rate of heat transfer and flow velocity can be determined [70]. The probes in the SCL-PIV wind tunnel are moved in three directions by a hydraulic system controlled by a computer with an accuracy of up to 1 mm in the y and z directions and up to 0.1 mm in the x direction. This system moves a mounting mechanism, linked to a bended guiding tube, which in turn holds the probe. Although the guiding tubes for the two probes are different, the mounting mechanism is the same, and switching from one anemometer to the other requires only minimal changes to the acquisition chain. The cables inserted in the bended guide tube are connected via BNC cables to the two channels of a DANTEC Streamline Pro conditioner, that also controls the wires. Each of the two

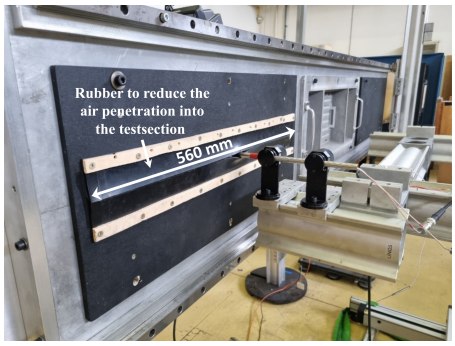

(a) Lateral panel with a long horizontal slot (width = 560 mm) used to measure the evolution of the flow properties in the streamwise direction.

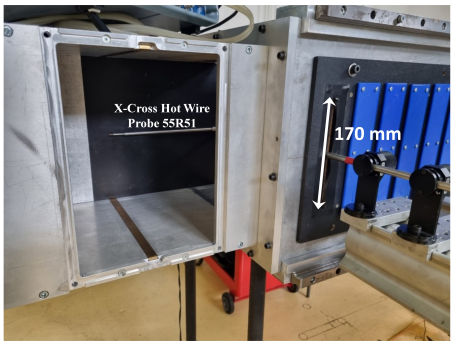

(b) Removable wooden panel with nine vertical slots (height = 170 mm) for measuring normal-wall and spanwise profiles.

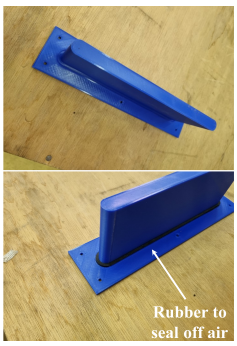

(c) 3D printed slot covers and rubber to prevent air penetration.

Figure 3.4: Different types of lateral panels to study the evolution of the flow properties in the three directions.

output channels leads to a National Instruments acquisition card CDAQ-9171, connected to the main computer via a USB port. Finally, the wind tunnel parameters (temperature and dynamic pressure) are acquired on a Furness FCO510 manometer. Figure 3.5 shows the temperature probe, the Pitot tube and the manometer.

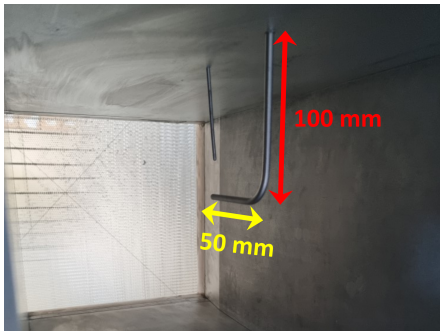

(a) The Pitot tube and the temperature probe inside the wind tunnel.

(b) Pitot tube and temperature probe from outside the wind tunnel transition section.

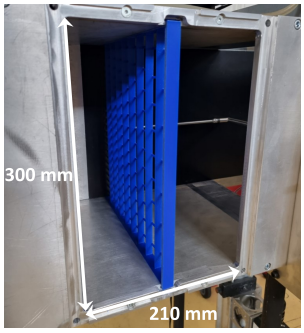

(c) Open panel with the grid inserted and the X-HWA probe.

Figure 3.5: Grid inserted in the open panel, Pitot tube and temperature probe.

All the experiments were carried out using an acquisition frequency of 100 KHz. Then, the signals from the anemometers were passed through the low-pass filters and were sampled using A.D. converter at 30 kHz, to remove any noise and disturbances. Finally, the acquisition time of the signals was limited to 30 *seconds* since the available hardware could not process larger amount of data.

3.1.2.1 The Single Hot Wire Anemometry (S-HWA)

A single hot wire probe measures the streamwise velocity component. The anemometer used during the experimental campaigns is a miniature wire (DANTEC 55P15) which presents a diameter of 5 μm and plated tungsten wire sensors 1.25 mm long (as shown in

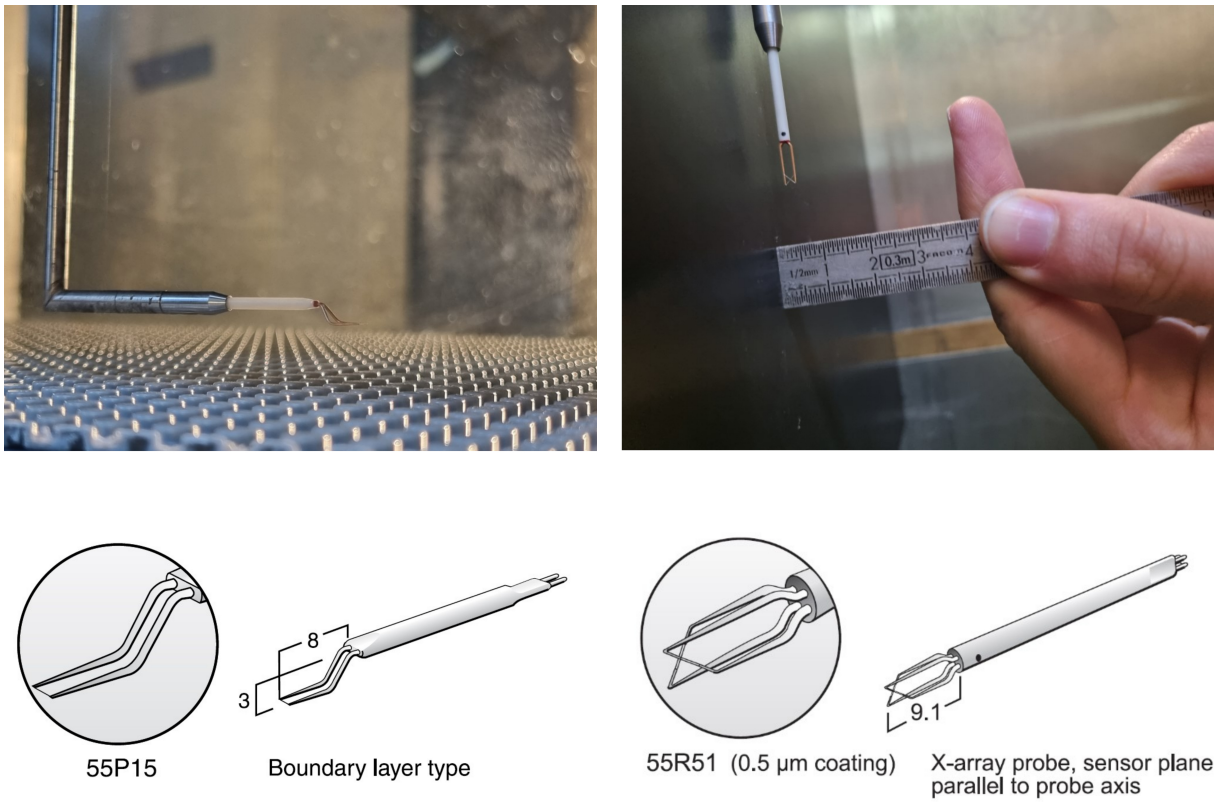

Figure 3.6: The two Hot Wire Anemometers used in the experiments.

Figure 3.6).

For two major reasons, this device was used in the project. First, due to the lower characteristic size of the probe compared to the X-cross wire probe, it has a higher precision in measuring the longitudinal fluctuation velocity gradient, which is important for estimating the turbulent dissipation rate. Furthermore, it has the ability to reach regions closer to the wall, allowing it to provide additional information about the inner layer. Indeed, the $1D$ anemometer 55P15 is designed particularly for measuring boundary layers since the shape of the prongs permits measurements close to a solid wall without disturbance from the probe body, which is out of the boundary layer.

3.1.2.2 The Cross Hot Wire Anemometry (X-HWA)

A two-wire probe (X wire) measures two velocity components that are in the plane formed by the two sensors. The anemometer used during the experimental campaigns is a X-cross hot wire (DANTEC 55R51) which presents a diameter of 70 μm and plated tungsten wire sensors 3 mm long, with a thin coating of 0.5 μm (see Figure 3.6).

The X-cross wire probe was used for the majority of the internship experiments since it enables for the measurement of the majority of the parameters of interest: velocity fluctuations moments, Reynolds stress, longitudinal spectrum, autocorrelation, and longi-

tudinal integral scales. Another advantage of the X-cross wire anemometer is that the probe support has been designed to be longer in order to reach the region very close to the grid. This was necessary because the grid is located at around 20 *cm* from the slot within which the guide tube moves (see Figure 3.4b). Getting as near to the grid as possible enables to get data at the typical locations of the turbulent intensity peaks.

3.1.2.3 HWA calibration

The calibration of single and X-cross probes were carried out in a specific nozzle-calibration facility (connected to a DANTEC Streamline Pro conditioner). The process is the same for 1D and 2D probes as well as the velocity range which is $0-50\ m/s$. The range is very large considering that the mean velocity imposed during the experiments is $U_{mean} = 15\ m/s$ (which is realistic value for the analysis of an Atmospheric Boundary Layer), however this is done to be conservative since in some points the local velocity might be high due to high turbulence intensity.

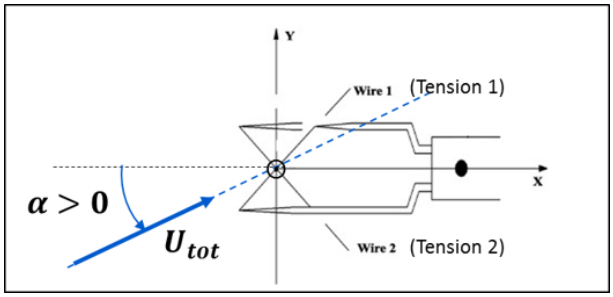

Figure 3.7: Scheme of the X-Cross HWA used for the calibration.

Figure 3.7 shows a schematic representation of a X-cross HWA, in which α represents the angle between the flow velocity direction and the probe axis, crucial in the calibration procedure for relating the tensions measured in the wires to the velocity components. The difference is that the S-HWA is calibrated only with the wire aligned along the flow direction (angle $\alpha = 0°$), while for the X-HWA the process is repeated for seven different angles ($\alpha = -45°, -30°, -15°, 0°, 15°, 30°, 45°$).

As already mentioned, through calibration a relationship between the rate of heat transfer and flow velocity can be determined [70]. Therefore, the aim is to determine coefficients, which include all the temperatures effects and which link the measured voltages to the flow velocity. To do that, two polynomial laws are used, one for the total velocity and one for the angle α, in which the polynomial degree can be chosen (in our analysis the values $d_I = 6$ and $d_J = 6$ are considered):

$$U_{tot} = \sum_{i=0}^{d_I} \sum_{j=0}^{d_J} \alpha_{ij} \left(E_1^2 - E_{10}^2\right)^i \left(E_2^2 - E_{20}^2\right)^j$$

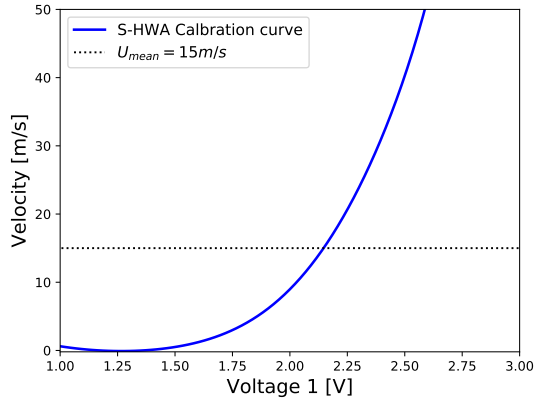

(a) Relationship between voltage and velocity for a single hot wire anemometer (S-HWA).

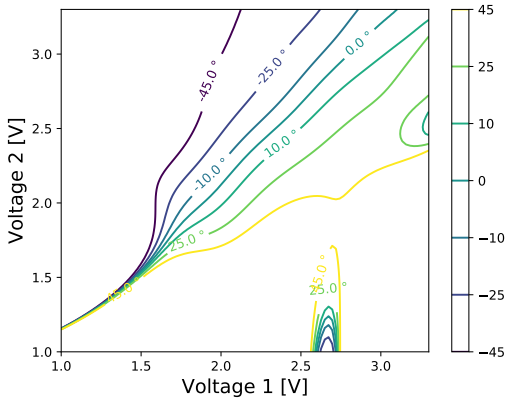

(b) Relationship between voltages and angles α for a X-cross hot wire anemometry (X-HWA).

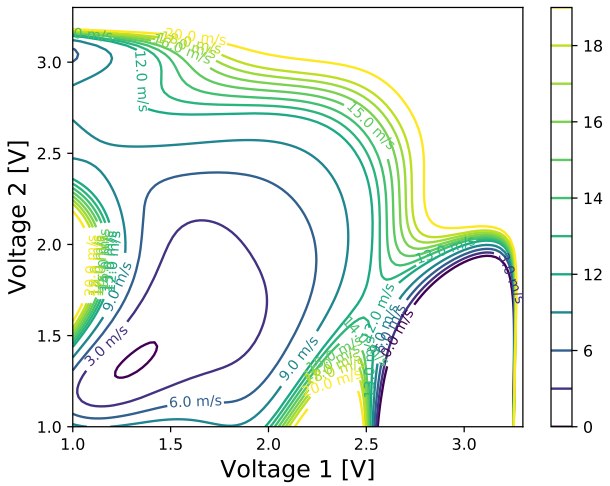

(c) Relationship between voltages and velocities for a X-cross hot wire anemometry (X-HWA).

Figure 3.8: Calibration plots obtained after the determination of α_{ij} and β_{ij}.

$$\alpha = \sum_{i=0}^{d_I} \sum_{j=0}^{d_J} \beta_{ij} \left(E_1^2 - E_{10}^2\right)^i \left(E_2^2 - E_{20}^2\right)^j$$

where $E_{10} = E_1\,(U_{tot} = 0)$ and $E_{20} = E_2\,(U_{tot} = 0)$ are the voltages measured when the flow velocity is zero. Through the calibration, the coefficients α_{ij} and β_{ij} are determined. Before and after each experiment, the values E_{10} and E_{20} are measured, and the average value is used to determine the velocities from the voltages. In the case of a single HWA, the same expressions can be used with $E_2 = E_{20} = 0$ and with the quantities j and d_J that have no relevance, since only the wire 1 is available. Figure 3.8 presents the results of the calibration for single probe (Figure 3.8a) and for the X-cross anemometer (Figures 3.8b and 3.8c) are presented. Since a polynomial function of sixth degree is used, it is possible to observe that the solutions for the X-cross wire are physical only for a certain range of voltages; when too high or too low values are approached, the results lose their

physical meaning.

3.2 Multiscale Inhomogeneous Grids (MIG)

The grids considered are Multiscale Inhomogeneous Grids (MIG) which were introduced by Zheng *et al.* (2018) [11] to extend an investigation that was first undertaken on fractal grids. In order to design the grid and apply the theoretical model to describe the turbulent flow formed, it is convenient to divide it into a certain number of layers. As previously mentioned, these grids have the potential of controlling independently the mean flow velocity and the turbulent intensity.

3.2.1 Geometric characteristics of the grids

Figure 3.9 shows an example of a Multiscale Inhomogeneous Grid, together with the main geometric characteristics that define its overall design. Table 3.1 summarizes the various notations for parameters that characterize a grid. In bold, the minimal set of independent parameters that define a grid design. The notations are similar to those used by Zheng *et al.* (2018) [11].

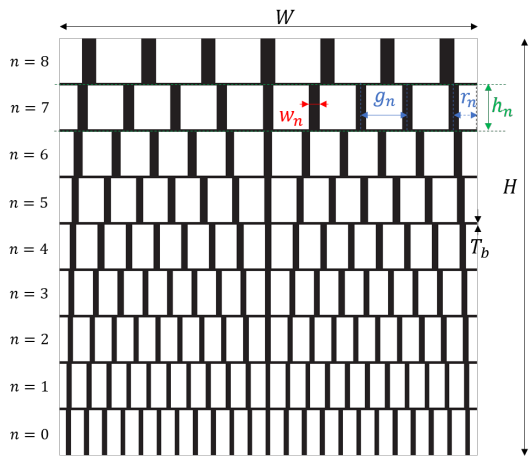

Figure 3.9: Grid design parameters definition. Adapted from: Zheng *et al.* (2018) [11].

Notation	Definition
N	Number of layers
W	Width of the grid section
H	Height of the grid section
$\mathbf{T_b}$	Width of the horizontal bars
$\mathbf{h_n}$	Height of layer n
$\mathbf{g_n}$	Distance between adjacent vertical bars at layer n (center to center)
$\mathbf{r_n}$	Distance from the wall of the first vertical bar of layer n (center to wall)
$\mathbf{w_n}$	Width of the vertical bars at layer n
$\mathbf{d_n}$	Streamwise depth of the vertical bars at layer n
$\mathbf{d_b}$	Streamwise depth of the horizontal bars
c_n	Number of vertical bars at layer n
σ_n	Blockage ratio (solidity) of layer n

Table 3.1: Grid parameters notation. Derived from Zheng *et al.* (2018) [11].

The 10 first parameters of Table 3.1 (in bold) are independent and characterizes completely a grid design. The following relationship is used to relate the number of vertical bars c_n to the distance between them (g_n and r_n):

$$\frac{W}{2} = \frac{c_n - 1}{2} g_n + r_n, \quad \text{with } 0 \leq r_n < g_n \text{ and } c_n \text{ an odd natural number} \tag{3.1}$$

In Zheng *et al.* (2018) [11], the implicit decision was to consider $r_n = \frac{1}{2} g_n$ to take advantage of the lateral wind tunnel wall's mirror effect on the flow and get closer to a

periodic condition in the lateral direction. This setting is expected to maximize downstream flow lateral homogeneity, which is why we shall use it by default unless otherwise specified.

In addition, the blockage ratio, often known as solidity, is defined as the ratio of the area obstructed by matter to the entire area of a region. The solidity σ_n of MIG grids is defined over the area between the center lines of two consecutive horizontal bars:

$$\sigma_n = \begin{cases} \frac{c_n w_n (h_n - T_b) + T_b W}{h_n W} & \text{for } n \in [|1, N-2|] \\ \frac{c_n w_n (h_n - T_b) + \frac{1}{2} T_b W}{\left(h_n - \frac{T_b}{2}\right) W} & \text{for } n = 0 \text{ or } n = N-1 \end{cases} \tag{3.2}$$

In particular, by inverting this equation, it is possible to compute w_n from σ_n, c_n, T_b and h_n :

$$w_n = \begin{cases} \frac{W}{c_n} \frac{\sigma_n h_n - T_b}{h_n - T_b} & \text{for } n \in [|1, N-2|] \\ \frac{W}{c_n} \frac{\sigma_n h_n - (1+\sigma_n)\frac{T_b}{2}}{h_n - T_b} & \text{for } n = 0 \text{ or } n = N-1 \end{cases} \tag{3.3}$$

The grid area is distributed in the vertical bars according to (3.3). Figure 3.9 shows that at each layer, the vertical bars are evenly separated by a distance g_n, and are positioned symmetrically about $y = 0$. Moreover, it is possible to define the aspect ratio of the vertical bars as $a_n = d_n/w_n$. The drag coefficient C_D of each bar is dependant of a_n and affects the wake characteristics. In order to achieve a uniform C_D over the grid's layers, the bars' aspect ratio is kept constant by adjusting d_n and w_n.

3.3 Theoretical models for tailoring the mean velocity profile

The MIG grids represent a new potential tool for overcoming some of the challenges related to the generation of an ABL in the wind tunnel: the ability to derive theoretical tools that do not require trials and errors to aid the design process, as well as independent control of mean flow and turbulent intensity profile. The project's major goal is to create a prescribed mean velocity profile representative of a neutral Atmospheric Boundary Layer, without attempting to tailor the turbulent intensity. This will be done using grids and spires with different geometries in order to explore the differences between full-section grids and partial-section devices. Therefore, this section explores the theoretical tools at our disposal to generate a prescribed mean flow profile using grids and spires.

3.3.1 First hypotheses and theoretical situation considered

The considered grid (such as the MIG grid discussed above) affects an originally undisturbed upstream parallel flow and creates a particular downstream mean flow (see figure 3.10), which is expected to be a parallel flow far enough away from the grid-perturbed area.

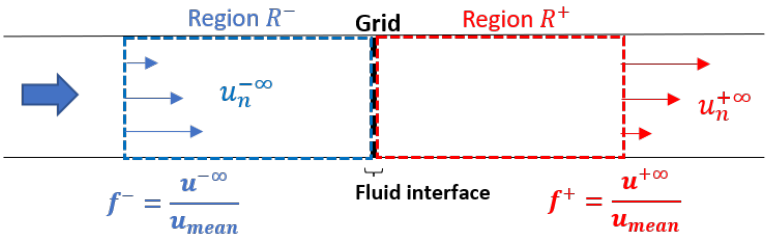

Figure 3.10: Schematic illustration of the regions examined around a grid in a wind tunnel. The stream flows from left to right. Region R^- and R^+ are defined to be long enough in comparison to the grid-disturbed regions they contain.

The upstream and downstream flows must be defined sufficiently far from the grid. Indeed, two regions of disturbance are generated near the grid, both upstream and downstream, where the flow cannot be expected to be exactly parallel (due to the deflections of streamlines). A far upstream mean flow $\overline{u}^{-\infty}$ and a far downstream mean flow $\overline{u}^{+\infty}$ can be defined when evaluated sufficiently far from these two regions, as shown in Figure 3.10.

The analysis that follows consists of identifying the relationships between the grid geometry parameters and these "far upstream" and "far downstream" velocity profiles. Taylor & Batchelor (1949) [71] were the first to offer such reasoning in order to quantify the impact of a grid on small perturbations of a uniform flow. Their goal was to apply the result to turbulent fluctuations.

In agreement with Taylor & Batchelor (1949) [71], the grid is assumed to be sufficiently thin to be considered as a fluid interface. This assumption implies that the velocity component normal to the grid is constant across the grid, but the tangential components have a discontinuity. Furthermore, the grid will be assumed to be perpendicular to the longitudinal direction of the wind tunnel.

3.3.2 Significant design parameters

Taylor and Batchelor (1949) [71] developed a theoretical expression relating the two velocity profiles to two grid parameters (assumed to have uniform properties throughout the wind tunnel section), such as the pressure drop coefficient at the grid K (or resistance coefficient) and the refraction coefficient α, defined by:

$$\begin{cases} K = \frac{p^{-0} - p^{+0}}{\frac{1}{2}\rho \overline{u}_0^2} \\ \alpha = \lim\limits_{v_{spanwise}^{-0} \to 0} \left(\frac{v_{spanwise}^{+0}}{v_{spanwise}^{-0}} \right) \end{cases}$$

The indice 0 stands for the value of each quantity when evaluated at the grid, seen as a fluid interface (-0 for "upstream", $+0$ for "downstream" and 0 for cases where upstream and downstream values coincide); ρ stands for the fluid density.
In the general situation, these two variables are dependent on the grid shape and may be

non-uniform across the grid section. Several experimental research have looked into the relationship between K and α and the grid's local characteristics.
Firstly, the resistance coefficient K can be related to the local solidity (or blockage ratio) σ of the considered grid by the relation suggested by Wieghardt (1953) [72] and reused by McCarthy (1964) [21] :

$$K = \frac{r\sigma}{(1-\sigma)^2} \tag{3.4}$$

where r is a coefficient depending only on the *Interstitial Reynolds number* [1] associated to each bar. The value of r as a function of Reynolds number was investigated in particular by Wieghardt (1953) [72], Cornell (1958) [73] and McCarthy (1964) [21]. In particular, Elder (1959) [63] considered $r = 1.0$ to be a reasonable choice for its purely theoretical purpose, although McCarthy (1964) [21] preferred to consider the value $r = 0.78$ for the relevant range of Reynolds number (which is frequently higher than 600). Based on the same investigations, $r = 0.7$ was chosen by Zheng *et al.* (2018) [11]. In order to have comparable results, the value of $r = 0.7$ will be considered for the entire analysis.

Other empirical expressions were derived to relate K with the blockage ratio σ (several other approaches are presented in Karnik & Tavoularis, 1987 [74]).
Regarding the refraction coefficient α, Taylor & Batchelor (1949) [71] have shown that it was possible to link it to the value of K through the empirical expression:

$$\alpha = \frac{B}{\sqrt{1+K}} \qquad \text{with } B = 1.1 \tag{3.5}$$

The expression (3.5) should be used carefully since it is demonstrated to be valid only for $K > 0.7$. The equation (3.4) associated with the usual value of σ that is encountered ($\sigma \in [0.1, 0.5]$) shows that K will mainly concentrate in the range $[0.0, 1.0]$. This might cause a mismatch between our models and the results of future measurements. Several other models have been suggested (Schubauer *et al.* (1950) [75], Elder (1959) [63], McCarthy (1964) [21], Reynolds (1969) [76], Gibbings (1973) [77], Li *et al.* (2018) [78]), but none of them was completely satisfactory for the range considered here.

Even if Laws & Livesey (1978) [79] in their review indicated some other expressions (for instance Gibbings (1973) [77]) to be more satisfactory, our choice is to conserve the equation (3.5) first introduced by Taylor & Batchelor (1949) [71], with results not severely different, in order to compare our results with Zheng *et al.* (2018) [11].

3.3.3 Generation of prescribed mean velocity flow

Taylor & Batchelor (1949) [71] considered the case of a uniform grid to evaluate the influence of the grid on the mean flow profile, deriving the following relation valid at each

[1] $r = r\left[\frac{u_0 w}{(1-\sigma)\nu}\right]$ where u_0 is the mean velocity at the grid, and w is the width of the grid bar

position on the transverse section:

$$\frac{d\overline{u}^{+\infty}}{d\overline{u}^{-\infty}} = \frac{1+\alpha-\alpha K}{1+\alpha+K} \tag{3.6}$$

It is worth to mention that this expression is valid only in a differential form, which means that it can only be used to characterize the grid's effect on upstream non-uniform disturbances. Therefore, an incoming non-uniform flow must be considered. More general conditions were studied by Elder (1959) [63], then by McCarthy (1964) [21] and applied during my internship. In particular in the project, the set of equations derived by McCarthy (1964) [21] has been used in order to tailor the mean flow profile. The whole derivation processes will not be detailed in the following sections; instead, the focus will be on the important assumptions and outcomes achieved.

The following are the requirements that must be met in order to use the McCarthy [21] model:

- Steady state flow and high Reynolds number, i.e. viscosity effects are limited to boundary layers and to the immediate vicinity of the grid. Moreover, the Reynolds number must be high enough to have viscosity effect restricted to a very thin sheet which could be seen as part of the fluid interface around the grid;
- The Reynolds stresses terms are implicitly neglected in the Reynolds Averaged Navier-Stokes (RANS) equations;
- The streamlines deflections caused by the grid are sufficiently small to consider the streamlines to be approximately rectilinear (i.e. $\overline{v} << \overline{u}$ and $\overline{w} << \overline{u}$);
- The resulting mean flow has no swirling components;

Starting from the Reynolds Averaged Navier-Stokes equations, applied both upstream (region R^-) and downstream (region R^-), and introducing the aforementioned hypothesis, McCarthy (1964) [21] derived the following system of equations which relates the local grid properties K and α to the mean flow profiles upstream ($u^{-\infty}$) and downstream ($u^{+\infty}$) from the grid:

$$\boxed{\begin{cases} \frac{u_0}{2} dK + K du_0 = d\left(u^{-\infty} - u^{+\infty}\right) \\ u_0 = \frac{u^{+\infty} + \alpha u^{-\infty}}{1+\alpha} \end{cases}}$$

By plugging u_0 expression into the first equation, the set of equations can be rewritten as only one equation:

$$\left[1 + \tfrac{K}{1+\alpha}\right] du^{+\infty} + \underbrace{\left[\frac{K\alpha}{1+\alpha} - 1\right] du^{-\infty}}_{=0 \text{ for McCarthy (1964)}} + \underbrace{\frac{u^{-\infty} - u^{+\infty}}{(1+\alpha)^2} K d\alpha + \frac{1}{2}\left[\frac{1}{1+\alpha} u^{+\infty} + \frac{\alpha}{1+\alpha} u^{-\infty}\right] dK}_{=0 \text{ for Taylor \& Batchelor (1949)}} = 0 \tag{3.7}$$

It is straightforward to show that this equation gives the result (3.6) of Taylor & Batchelor (1949) [71] when applied to a grid with uniform properties ($dK = 0$ and $d\alpha = 0$).

To solve equation (3.7), McCarthy (1964) [21] used the empirical expression of α as a function of K (Equation (3.5)), moreover he introduced the assumption of a uniform incoming flow (i.e. $du^{-\infty} = 0$ and $u^{-\infty} = u_{mean}$) avoiding constraints in the grid properties distribution. As a result, he could reduce the problem to an Ordinary Differential Equation (ODE) which can be solved analytically leading to the following expression:

$$f^+ = 1 - \mathcal{N}\mathcal{A}(K)\left(\mathcal{B}(K) - \gamma\right) \tag{3.8}$$

$$\text{With: } \begin{cases} \mathcal{N} \approx 1.01 \\ \mathcal{A}(K) = \frac{1+\sqrt{1+K}}{\left(1+(1+K)^{3/2}\right)^{2/3}} \\ \mathcal{B}(K) = \frac{\frac{1}{6}+(1+K)^{3/2}}{1+K} \\ \gamma = \dfrac{\displaystyle\int_{section} \mathcal{A}(K)\mathcal{B}(K)\mathrm{d}S}{\displaystyle\int_{section} \mathcal{A}(K)\mathrm{d}S} \end{cases}$$

where $f^+ = \frac{u^+}{u_{mean}}$ is the normalized downstream mean flow, $u_{mean} = \frac{1}{S}\int_{WTsection} \overline{u} dS$ the integral mean velocity, with S being the section area of the wind tunnel.

Chapter 4

Design process for atmospheric flow generators

The internship project has followed the six main steps listed:

- The study of the characteristics and experimental methods of the atmospheric boundary layer, guided by an ABL literature's review conducted by the PhD student Thomas Huret and summarized in chapter 2;
- The application of theoretical analysis on Multiscale Inhomogeneous Grids (MIG) to the task of creating a full-depth Atmospheric Boundary Layer in a wind tunnel, by using full-section grids, partial-section grids and spires;
- The design and production of grids and spires characterised by different geometries and prescribed velocity profiles;
- Preparation and execution of two main experimental campaigns in the boundary layer wind tunnel (SCL-PIV) at ONERA Lille using the Hot Wire Anemometry (HWA) technique;
- Implementation of artificial roughness in the wind tunnel to fulfill the similarity condition (see 2.5.1) and analysis of its interaction with the grid-generated flow;
- Post-processing and analysis of the data;

The first part of this chapter describes the main theoretical features of MIG grids model applied to the atmospheric boundary layer, modelled using the "Law of the wake" (2.3). This law is chosen because the goal is to reproduce a Neutral ABL in the wind tunnel, which is analogous to a classical turbulent boundary layer over a rough surface [26]. Coriolis forces and the Ekman layer, which would require large rotating facilities to be replicated, cannot be taken into account by this model.

The grid design technique is then discussed, with a focus on the differences between partial-section and full-section grid models. It is worth to mention that the grids' design

algorithm can be adapted to produce spires which are able to replicate the same velocity profiles even if they have a completely different geometry.

The second section of the chapter explains the importance of simulating the Earth's surface roughness in the wind tunnel in order to satisfy the similarity criterion defined by Jensen & Franck (1963) [50]. To determine which method will work best for the experimental campaigns, two different methods for simulating roughness in the wind tunnel are examined.

The last section presents the 3D printed grids and spires that will be tested in the wind tunnel, highlighting the goals and the geometric characteristics of the various configurations. The devices are presented in the chronological order in which they were manufactured, in order to emphasise the design decisions and the development of the experimental study.

4.1 Grid design

This section describes the main steps required to design a MIG grid by applying the McCarthy (1964) [21] model. Moreover, it explains how to implement the "Law of the wake" (2.3) to produce the required mean velocity profile. Finally, the properties of the 3D printed grids are presented and discussed.

4.1.1 Application of McCarthy model to a MIG grid

In section 3.3.3 a brief explanation of the theoretical model derived by McCarthy (1964) [21] is given, which leads to the Equation (3.8). This theory enables to design a grid for a prescribed downstream mean flow. The wind tunnel section is discretized into N horizontal layers due to the layout of a MIG grid. As a result, the problem may be expressed as a set of N coupled equations, derived by applying the equation (3.8) on each middle points of the N layers. The obtained system of equations can be written as:

$$\forall n \in [|0, N-1|], \quad f_n^+ = 1 - \mathcal{N}\mathcal{A}(K_n)\left(\mathcal{B}(K_n) - \gamma\left((K_n)_{n\in[|0,N-1|]}\right)\right) \tag{4.1}$$

$$\text{with : } \begin{cases} \mathcal{N} \approx 1.01 \\ \mathcal{A}(K_n) = \frac{1+\sqrt{1+K_n}}{\left(1+(1+K_n)^{3/2}\right)^{2/3}} \\ \mathcal{B}(K_n) = \frac{\frac{1}{6}+(1+K_n)^{3/2}}{1+K_n} \\ \gamma\left((K_n)_{n\in[|0,N-1|]}\right) = \dfrac{\sum_{n=0}^{N-1}\mathcal{A}(K_n)\mathcal{B}(K_n)h_n}{\sum_{n=0}^{N-1}\mathcal{A}(K_n)h_n} \end{cases}$$

The vector $(f_n^+)_{n\in[|0,N-1|]}$ contains the desired downstream mean flow profile, while the unknown of this set of N non-linearly coupled equations is the vector $(K_n)_{n\in[|0,N-1|]}$.
More precisely, the real unknown we are interested in is the distribution of blockage ratio $(\sigma_n)_{n\in[|0,N-1|]}$, since it is the quantity directly related to the grid geometry. It is possible to derive the blockage ratio from the resistance coefficient through the inversion of a modified version of equation (3.4). Indeed, the latter is only applicable to grids consisting of arrays of circular rods, since MIG grids have very different properties. The law that can be used in our case is the following (from Roach, 1987 [80]):

$$K = A\left[\frac{1}{(1-\sigma)^2 - 1}\right]^B \tag{4.2}$$

$$\text{with : } \begin{cases} A = 0.98 \\ B = 1.09 \end{cases}$$

which leads to:

$$\sigma_n = 1 - \frac{1}{\sqrt{1 + \left(\frac{K_n}{A}\right)^{1/B}}} \tag{4.3}$$

This equation allows for the construction of a specified constraint on the mean blockage ratio throughout the whole grid, which in turn results in a constraint on the distribution of K_n:

$$\sigma_{mean} := \frac{1}{H}\sum_{n=0}^{N-1}\sigma_n h_n = \frac{1}{H}\sum_{n=0}^{N-1}\left(1 - \frac{1}{\sqrt{1 + \left(\frac{K_n}{A}\right)^{1/B}}}\right)h_n \tag{4.4}$$

In fact, there are several distributions with various mean solidities σ_n that might provide the same downstream mean flow profile, hence the solution to the system (4.1) alone is not unique. Therefore, Equation (4.4) is necessary to close the system and to have a unique solution.
As a result, the optimization problem may be expressed using a least-squares cost function like the one shown below:

$$\begin{aligned} \underset{(K_n)_{n\in[|0,N-1|]}}{\text{Minimize}} \quad & \sum_{n=0}^{N-1} \mathbf{f_n^{+,prescribed}} - \left[1 - \mathcal{NA}(K_n)\left(\mathcal{B}(K_n) - \gamma\left((K_n)_{n\in[|0,N-1|]}\right)\right)\right]\Big|^2 h_n \\ \text{Subject to} \quad & \forall n \in [|0, N-1|],\ \boldsymbol{\sigma_{min}^{prescribed}} \leq \sigma_n := 1 - \frac{1}{\sqrt{1 + \left(\frac{K_n}{A}\right)^{1/B}}} \leq \boldsymbol{\sigma_{max}^{prescribed}}, \\ & \boldsymbol{\sigma_{mean}^{prescribed}} = \frac{1}{H}\sum_{n=0}^{N-1}\left(1 - \frac{1}{\sqrt{1 + \left(\frac{K_n}{A}\right)^{1/B}}}\right)h_n \end{aligned}$$

In this way, the user can decide the range of possible values for σ_n (and so for K_n) in

order to get a unique and physical solution. However, there are some constraints in the choice of σ_n bounds:

- $\sigma_{min}^{prescribed}$ must ensure that $c_n w_n \geq 0$ (which is the case of the smallest possible solidity at layer n). Considering the expression (3.2) it is possible to prove that σ_n cannot be lower than $\sigma_{min}^{prescribed}$;
- $\sigma_{max}^{prescribed}$ has to be chosen not to exceed the physical threshold where the flow regime experiences a transition from "wakes-interaction" to "jets-interaction", as suggested by Rose (1966) [61] after Corrsin (1963) [62]. This threshold has been explored during the research and it will be discussed in the next chapters.

It is worth to notice that when we consider partial grids, designed to reproduce a prescribed mean velocity profile over the full section, it is not possible to select a predefined mean solidity σ_{mean}. Indeed, for this case the condition is directly applied to the vector K_n. The latter is constrained to have null values for the section's layers that are not occupied by the grid. This is reasonable because in the region without grid there is not obstruction, and by definition, we must have $K_n = \sigma_n = 0$. Moreover, the solidity bounds ($\sigma_{min}^{prescribed}$ and $\sigma_{max}^{prescribed}$) are reasonable only in the grid region since in the empty part the solidity is null due to the constraint.
In the early phases of the project, the two constraints were combined to resolve the minimization problem, but they proved to be incompatible. In particular, the algorithm generated grids with a velocity profile that was very different from what was desired. The final choice has been to avoid controlling the σ_{mean} value in favor of the mean velocity profile and the distribution of K_n (or σ_n) along the wind tunnel section.

It is possible to introduce the new parameter l which is the number of effective layers of the partial grid. This quantity is always smaller than N, which remains the number of layers that partition the test section of the wind tunnel. In the case of full-section grids the two parameters coincide ($N = l$). As a result, the problem to minimize for partial-section grids can be stated as follows:

$$\begin{aligned}
&\underset{(K_n)_{n\in[|0,N-1|]}}{\text{Minimize}} \quad \sum_{n=0}^{N-1} \mathbf{f_n^{+,prescribed}} - \left[1 - \mathcal{NA}(K_n)\left(\mathcal{B}(K_n) - \gamma\left((K_n)_{n\in[|0,N-1|]}\right)\right)\right]\Big|^2 h_n \\
&\text{Subject to} \quad \forall n \in [|0, N-1|],\ \boldsymbol{\sigma_{min}^{prescribed}} \leq \sigma_n := 1 - \frac{1}{\sqrt{1 + \left(\frac{K_n}{A}\right)^{1/B}}} \leq \boldsymbol{\sigma_{max}^{prescribed}}, \\
&\text{Subject to} \quad \forall n \in [|l, N-1|], \quad \boldsymbol{\sigma_n = 0}
\end{aligned}$$

4.1.2 The design process of a MIG grid for a prescribed mean flow

Now the major procedures for designing a Multiscale Inhomogeneous Grid (MIG) will be provided emphasizing the distinction between partial-section and full-section grids.

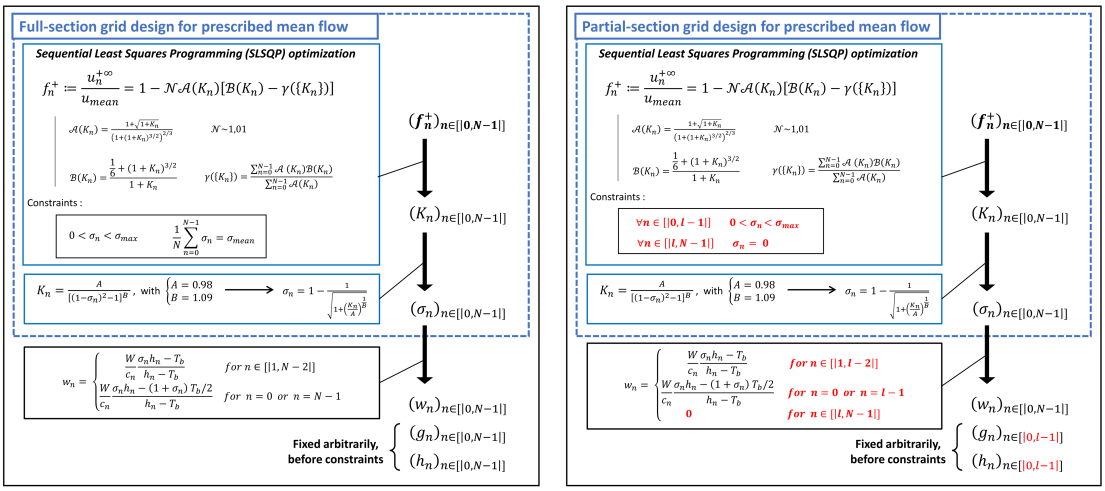

(a) Full-section design. **(b)** Partial-section grid.

Figure 4.1: Main steps for the grid design of full-section and partial-section grids. The main differences between the two methods are highlighted in red.

The essential steps are illustrated in both situations in Figure 4.1 and can be summarized as follows:

1. First of all, it is important to decide the number of layers of the grids, N for a full-section grid and l for a partial-section grid. Then the designer can choose the mean velocity profile (non-dimensionalized as $f_n^{+,prescribed} = \frac{\overline{u}_n^{+\infty,prescribed}}{\overline{u}_{mean}}$), a mean blockage ratio $\sigma_{mean}^{prescribed}$ (in the case of full grid) and a maximum blockage ratio ($\sigma_{max}^{prescribed}$). It is possible to utilize the SLSQP optimization algorithm from the Python SciPy module to solve the previously mentioned optimization problem, with different constraints for the two cases, in order to obtain the required values for K_n;

2. The distribution of K_n leads to the distribution of σ_n through the equation (4.3);

3. Once the values of h_n and c_n are fixed, for instance by choosing $h_n = \frac{H-T_b}{N}$ and $c_n = 2(n+3)+1$, the distribution of σ_n leads to a constraint on the geometrical parameters of the grid. Indeed, the computed value of σ_n leads to a value of w_n through equation (3.3). Although the latter equation is valid for the full-section grid, for the partial-section grid it can be only used for the physical layers (up to the layer $l-1$). In the empty section w_n assumes null values since there are no bars. Equation (3.3) can be adapted to the partial grid leading to the following expression:

$$w_n = \begin{cases} \frac{W}{c_n}\frac{\sigma_n h_n - T_b}{h_n - T_b} & \text{for } n \in [|1, l-2|] \\ \frac{W}{c_n}\frac{\sigma_n h_n - (1+\sigma_n)\frac{T_b}{2}}{h_n - T_b} & \text{for } n = 0 \text{ or } n = l-1 \\ 0 & \text{for } n \in [|l, N-1|] \end{cases} \tag{4.5}$$

As shown also in Figure 4.1b, the quantities h_n and c_n have physical meaning only in the region occupied by the grid.

4.1.3 Method for the computation of the normalized velocity profile

As described in the previous section, one of the first steps of the design process is the choice of the prescribed non-dimensional mean flow profile. This section explains how to derive $f_n^{+,prescribed}$, which can be computed with Equation (4.6), knowing the mean velocity u_{mean} imposed in the wind tunnel. It is important to mention that this method requires knowledge of the $\Pi(x)$ function and the desired surface roughness properties (k_s or h_0).

$$f_n^{+,prescribed} = \frac{\overline{u_n^+}^{\infty,prescribed}}{\overline{u}_{mean}} \tag{4.6}$$

The desired mean velocity profile used in the optimization algorithm to get the grid's geometrical characteristics is derived in the same way for each design approach. The goal, in fact, is to obtain four different grids in terms of geometry producing the same velocity profile, but with different boundary layer heights.

As briefly explained in section 2.2.1.3, the law used to describe the artificial boundary layer flow is the "law of the wake", since it is a physical law which yields correct results both in the inner layer (except for the "viscous sublayer" part of the boundary layer which is negligibly thin) and outer layer.

The mean velocity is imposed and, therefore, known in wind tunnel tests, but the free stream velocity U_∞ and friction velocity u_* are unknowns. To deduce the two unknowns and achieve the prescribed wind tunnel normalized velocity profile (4.6), the system of two equations (4.7) must be solved.

$$\begin{cases} u_{mean} = \frac{1}{H} \cdot \left[u_* \int_d^{\delta+d} \frac{1}{\kappa} \ln\left(u_* \frac{z-d}{\nu}\right) + C - \Delta U^+ + \frac{\Pi(x)}{\kappa} \cdot \omega\left(\frac{z-d}{\delta}\right) dz + \int_{\delta+d}^{H+d} U_\infty dz \right] \\ U_\infty = u_* \left[\frac{1}{\kappa} \ln\left(u_* \frac{\delta}{\nu}\right) + C - \Delta U^+ + 2\left(\frac{\Pi(x)}{\kappa} \sin\frac{\pi\delta}{2\delta}\right)^2 \right] \end{cases} \tag{4.7}$$

where ΔU^+ is a function of the roughness Reynolds number (k_s^+), C_s, κ and the two limit values of the roughness Reynolds number k^+_{Smooth} and k^+_{Rough}, as shown in Equation (2.5).

Because all of the other variables that compare in the equation are known when the grids are designed, the second equation of the system (4.7) expresses U_∞ as a function of just u_*. Therefore, it is possible to compute u_* by plugging the second equation into the first one and solving the problem numerically. Once u_* is known, it is straightforward to derive U_∞ from the second equation. However, in the first equation of (4.7), the unknown u_* compares inside the integral in the first term on the right hand side, therefore this integral must be solved analytically. By doing so, the final expression of u_{mean} is obtained

(4.8):

$$u_{mean} = \frac{1}{H}\left\{\frac{u_*}{\kappa}\delta\left[\ln\left(u_*\frac{\delta}{\nu}\right)-1\right]-\frac{u_*}{\kappa}\delta\Delta U^+(u_*)+u_*\delta C+u_*\int_d^{\delta+d}\frac{\Pi(x)}{\kappa}\cdot\omega\left(\frac{z-d}{\delta}\right)dz\right\} + \left(1-\frac{\delta}{H}\right)u_*\left[\frac{1}{\kappa}\ln\left(u_*\frac{\delta}{\nu}\right)+C-\Delta U^+ + 2\left(\frac{\Pi(x)}{\kappa}\right)^2\right] \tag{4.8}$$

At this point, it is possible to move all the terms to the left hand side of the equation and solve it numerically, for example using the optimization algorithm ***"fsolve"*** from the Python *"scipy.optimize"* module. This method requires the introduction of a cost function, which is indicated as $g(u_*)$ in (4.9).

$$g(u_*) = u_{mean} - \frac{1}{H}\left\{\frac{u_*}{\kappa}\delta\left[\ln\left(u_*\frac{\delta}{\nu}\right)-1\right]-\frac{u_*}{\kappa}\delta\Delta U^+(u_*)+u_*\delta C+u_*\int_d^{\delta+d}\frac{\Pi(x)}{\kappa}\cdot\omega\left(\frac{z-d}{\delta}\right)dz\right\} - \left(1-\frac{\delta}{H}\right)u_*\left[\frac{1}{\kappa}\ln\left(u_*\frac{\delta}{\nu}\right)+C-\Delta U^+ + 2\left(\frac{\Pi(x)}{\kappa}\right)^2\right] = 0 \tag{4.9}$$

The friction velocity u_* is derived from (4.9) and plugged into the U_∞ equation, in order to obtain the free stream velocity (U_∞). Finally, from (4.6) the prescribed normalized velocity profile can be determined and utilized for the the grid geometry design.

4.1.4 The velocity scale for a prescribed mean velocity flow

The neutral atmospheric boundary layer (ABL) can be usually described considering the *Ekman Boundary Layer* (see section 2.3), which is the result of a force balance between three main contributions: Coriolis force, pressure force and turbulent friction. As suggested by Monin & Obukhov, the region close to the Earth surface (up to about 50 m to 100 m, according to J. C. Kaimal and J. J.Finnigan (1994) [5]) is referred as "*Surface Layer (SL)*". Furthermore, the SL contains in its inner part (very close to the surface) the "*Roughness SubLayer (RSL)*". The latter, with a thickness of around $2-3$ times the roughness element height, may be ignored in the subsequent study since it is so little in comparison to the ABL's overall height.

The surface layer in neutral conditions is characterized by a logarithmic mean flow profile described by the equation:

$$\overline{u}(z) = \frac{u_*}{\kappa}\ln\left(\frac{z-d}{h_0^r}\right) \tag{4.10}$$

where the dependency on surface roughness is reflected by the "roughness height" h_0^r and also (generally), by a "displacement height" d, which redefines the origin of the altitudes. Furthermore, both these two length scales are non-trivial functions (because aggregated by aerodynamic effects) of the roughness geometry.

It is important to relate the experimental results obtained in the wind tunnel to the

full scale Atmospheric Boundary Layer (ABL). In the following analysis, the subscript "ABL" stands for full scale quantities, while its absence stands for wind tunnel quantities. If the scale S is known, it is straightforward to determine the altitudes and roughness height in the full scale ABL. Indeed, it is sufficient to multiply the quantities in the wind tunnel by the scale S: $z_n^{ABL} = Sz_n$ and $h_0^{ABL} = Sh_0^r$. Knowing these relations, it is easy to notice that the same logarithmic law applies both in the wind tunnel and at natural scale:

$$\overline{u_n}^{ABL} = \frac{u_*^{ABL}}{\kappa} \ln\left(\frac{z_n^{ABL} - d^{ABL}}{h_0^{r,ABL}}\right) \Rightarrow \overline{u_n} = \frac{u_*}{\kappa} \ln\left(\frac{z_n - d}{h_0^r}\right) \tag{4.11}$$

At this point, the wind tunnel normalized objective velocity profile can be computed, adding the term that takes into account the free stream turbulence effect on the mean velocity profile:

$$f_n^+ = \frac{ln\left(\frac{z_n - d}{h_0^r}\right) + \frac{\Pi(x)}{\kappa}\omega\left(\frac{z_n}{\delta}\right)}{\frac{1}{H}\sum_{n=0}^{N-1}\left[ln\left(\frac{z_n - d}{h_0^r}\right) + \frac{\Pi(x)}{\kappa}\omega\left(\frac{z_n}{\delta}\right)\right]h_n} \tag{4.12}$$

The normalized objective profile is not dependant of u_*, meaning that a specific grid producing a law of the wake profile is not linked to a specific u_*. It is now possible to define a specific velocity scale which enables us to calculate u_*^{ABL} knowing u_*. A Strouhal number similarity related to the shear timescale might be used:

$$\frac{L^{ABL}\left(\frac{\partial \overline{u}^{ABL}}{\partial z^{ABL}}\right)}{U^{ABL}} \underset{\text{Strouhal similarity}}{=} \frac{L\left(\frac{\partial \overline{u}}{\partial z}\right)}{U} \tag{4.13}$$

Note that the Strouhal number similarity is valid if all the essential similarity criteria (presented in subsection 2.5.1) are fulfilled.

The length scales L^{ABL} and L are arbitrary length scales of the system, and in the same fashion, the two velocity scales U^{ABL} and U can correspond to any arbitrary velocity of the system. The equation (4.13) can be rewritten as follows:

$$\frac{U}{U^{ABL}} = \underbrace{\frac{L}{L^{ABL}}}_{\frac{1}{S}} \frac{\left(\frac{\partial \overline{u}}{\partial z}\right)}{\left(\frac{\partial \overline{u}^{ABL}}{\partial z^{ABL}}\right)} \tag{4.14}$$

Let us now define the following quantity:

$$S_T = \frac{\left(\frac{\partial \overline{u}}{\partial z}\right)}{\left(\frac{\partial \overline{u}^{ABL}}{\partial z^{ABL}}\right)}$$

It corresponds to a constant scaling for timescales, equivalent to the role of S for length scales. There is currently no information available to say whether this number is dependent or independent of the other scaling S variable. The last two equations lead to the following relation:

$$U = \frac{S_T}{S} U^{ABL} \tag{4.15}$$

This is a general expression, valid for any velocity, which gives the scaling relation for the velocities between wind tunnel and full-scale. Applying it to $U = u_n$ and taking the average over n of the expression, it leads to:

$$u_{mean} = \sum_{n=0}^{N-1} \frac{u_*}{\kappa} \left[ln\left(\frac{z_n - d}{h_0^r}\right) + \Pi(x) \cdot \omega\left(\frac{z_n}{\delta}\right) \right] \frac{h_n}{H}$$

Considering the relations (4.11) and (4.15), it is possible to derive the following expression:

$$u_{mean} = \frac{S_T}{S} \left\{ \sum_{n=0}^{N-1} \frac{u_*^{ABL}}{\kappa} \left[ln\left(\frac{z_n^{ABL} - d^{ABL}}{h_0^{r,ABL}}\right) + \Pi(x) \cdot \omega\left(\frac{z_n^{ABL}}{\delta^{ABL}}\right) \right] \frac{h_n}{H} \right\}$$

So that:

$$u_{mean} = \frac{S_T}{S} \left\{ \sum_{n=0}^{N-1} \frac{1}{\kappa} \left[ln\left(\frac{z_n^{ABL} - d^{ABL}}{h_0^{r,ABL}}\right) + \Pi(x) \cdot \omega\left(\frac{z_n^{ABL}}{\delta^{ABL}}\right) \right] \frac{h_n}{H} \right\} u_*^{ABL}$$

It is equivalent to:

$$\boxed{u_{mean} = \frac{S_T}{S} \left\{ \sum_{n=0}^{N-1} \frac{1}{\kappa} \left[ln\left(\frac{z_n - d}{h_0^r}\right) + \Pi(x) \cdot \omega\left(\frac{z_n}{\delta}\right) \right] \frac{h_n}{H} \right\} u_*^{ABL}}$$

This last expression reveals that for a given grid and a given distribution of z_n, the time scaling S_T is only dependent on the mean velocity chosen in the wind tunnel. It directly implies that in such wind tunnel tests, the duration Δt of an experiment in the wind tunnel is representative of a full-scale experiment of duration $\Delta t^{ABL} = S_T \Delta t$, where S_T is chosen by the user through the choice of u_{mean}. In particular, the equation (4.15) can be applied to the friction velocity : $u_* = \frac{S_T}{S} u_*^{ABL}$. Moreover, since the velocities achieved in the wind tunnel (about 15 m/s) are almost the same as the characteristic values in the atmosphere, $S_T \approx S$.

4.2 Roughness fetch

4.2.1 Reason of the introduction of roughness

The "Jensen number" should be preserved between the full scale atmospheric boundary layer and the wind tunnel flow in order to fulfill the similarity criteria specified by Jensen & Franck (1963) [50]. It is defined as $J_e = D/h_0^r$, where h_0^r is the roughness length and D is a characteristic length of an object of interest within the ABL or even directly the height of the layer of interest. In practice, this criterion may be seen as the usual geometric

similarity criterion, but applied to roughness elements, which requires the introduction of a roughness fetch in order to reproduce the ABL in the wind tunnel.

The designed MIG grids aim at reproducing the mean flow described by the law of the wake, which in the lower part (close to the wall) follows a logarithmic law. In this case, the grid itself is introducing a "ghost" roughness length $h_0^{r,grid}$, necessary for the definition of the logarithmic profile. However, it is expected that a grid-generated flow without a roughness fetch (qualified as "fully artificial" ABL generated flow by Cook, 1978 [10]) would not follow the prescribed flow (in our case, the law of the wake) for an infinitely long distance in the streamwise direction. Indeed, there would be insufficient wall roughness to mantain a turbulent production as in the full scale. Instead, such situation could likely lead to the prescribed mean flow profile for a finite downstream region, followed by a different mean flow profile. It would be interesting to estimate the length of the region where the prescribed law of the wake is valid.

A second potential configuration consists of adding a roughness fetch downstream of a MIG grid (with a roughness length h_0^r very close to the $h_0^{r,grid}$ of the grid itself). In this case, the configuration becomes more similar to those outlined by Cook (1978) [10] but with some differences: Cook (1978) [10] looked at the scenario of a uniform grid with a wall and a roughness fetch, which works in a similar way but provides less tailoring possibilities. Indeed, the combination of MIG grid with roughness could lead to two improvements:

- To tailor both mean flow and turbulence intensity (in this paper the focus will be on the mean flow);
- To adapt the design to any prescribed flows, with a reduced amount of trial-and-error process;

4.2.2 Roughness fetch design

It is necessary to set the rough surface in proportion to the needed roughness length (h_0^r) in order to analyze the interaction of MIG grids with a roughness fetch during our experimental campaign.

Considering the "law of the wake" in the form given by Coles (1956) [32]:

$$U^+ = \frac{1}{\kappa} \ln z^+ + C - \Delta U^+ + \frac{\Pi(x)}{\kappa} \omega \left(\frac{z}{\delta} \right) \tag{4.16}$$

It is possible to notice that the "wake function" $\omega \left(\frac{z}{\delta} \right)$, which can be expressed as a sine-squared function as suggested by J. Hinze (1975) [33] (2.4), is negligibly small in the logarithmic-layer, where $\frac{z}{\delta} \approx 0.1$. Indeed, the Coles (1956) is a superposition of the "law of the wall" (also termed as "log-law") due to the wall shear stress and the law of the wake due to the free turbulence at the core. It is of interest to relate the different formulations of logarithmic profile (expressed by the "law of the wall") derived by the two scientific communities interested in rough turbulent boundary layers: atmospheric scientists and

fluid dynamicists. For the fluid dynamicist community, the "law of the wall" over a rough surface was historically expressed on the form given by Raupach et al. (1991) [81]:

$$U^+ = \frac{\overline{u}(z)}{u_*} = \frac{1}{\kappa}\ln\left(z^+\right) + C_0 - \frac{\Delta U}{u_*}\left(h^+, L_i^+\right) \tag{4.17}$$

where $z^+ = \frac{zu_*}{\nu}$ is the altitude (z) normalized by the friction length scale ($\delta_\nu = \nu/u_*$), $h^+ = \frac{hu_*}{\nu}$ stands for the normalized roughness geometric height h and $L_i^+ = \frac{L_i u_*}{\nu}$ represents the normalization of all the other possible length L_i characterizing the roughness geometry. The expression (4.17) is explicitly dependent on the roughness Reynolds number $k_s^+ = \frac{u_* k_s}{\nu}$, hidden inside $\Delta U^+ = \frac{\Delta U}{u_*}$.

The preferred formulation of the mean flow profile for researchers interested in the ABL is based on the fact that at very high Reynolds numbers, the flow characteristics are no longer dependent on Reynolds number. As a result, it is convenient to normalize the altitude by the roughness height h instead of δ_ν, as explained in Raupach et al. (1991) [81]:

$$U^+ = \frac{\overline{u}(z)}{u_*} = \frac{1}{\kappa}\ln\left(\frac{z-d}{h}\right) + c\left(h^+, \frac{L_i}{h}\right) \tag{4.18}$$

The equation (4.18) is generally rewritten as the following:

$$U^+ = \frac{\overline{u}(z)}{u_*} = \frac{1}{\kappa}\ln\left(\frac{z-d}{h_0^r}\right) \tag{4.19}$$

which can be seen also as a definition of h_0^r and d.
According to Raupach et al. (1991) [81], the velocity of this profile is equal to zero for $z = d + z_0$, implying that:

$$\ln\left(\frac{h_0^r}{h}\right) = -\kappa c\left(h^+, \frac{L_i}{h}\right) \tag{4.20}$$

By applying the equation (4.17) at the same altitude, the following relation is derived:

$$\ln\left(\frac{h_0^r}{h}\right) = -\kappa\left[C_0 - \frac{\Delta U}{u_*}\left(h^+, \frac{L_i}{h}\right)\right] - \ln\left(h^+\right) \tag{4.21}$$

which relates the function c to the well-known function $\frac{\Delta U}{u_*}$ (which can be expressed as in (2.4)).

Finally, the equation (4.20) can be applied to the Fully Rough Regime where the flow does not depend anymore on the Reynolds number for $h^+ \to +\infty$. In practice, this condition is reached when $h^+ > 70$ (Nikuradse (1933 [82]), Sutton (1949) [47], Jimenez (2004) [26], Kundu (2016) [83]). The equation leads to:

$$\frac{h_0^r}{h} = e^{-\kappa c_\infty\left(\frac{L_i}{h}\right)} \tag{4.22}$$

This expression leads to the important conclusion that in Fully Rough Regime, h_0^r is only a

function of the roughness geometry. At this point, it is important to derive an expression of c_∞ depending on the geometry. Two "rough configurations" will be compared to determine which is the better choice for our experimental campaign (see figure 4.2). Finally, some of the experiments will be conducted in the "smooth configuration", represented by the flat-plate at the wall.

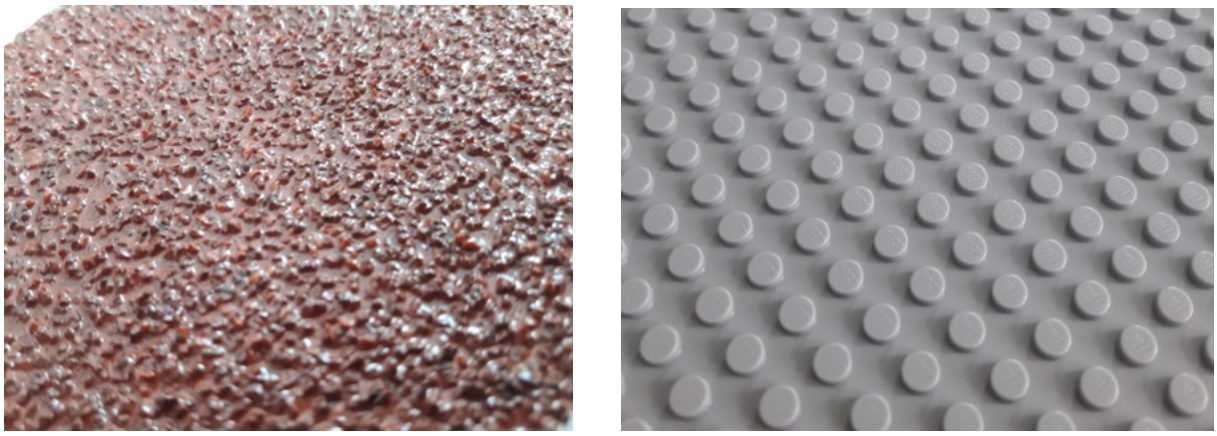

(a) Abrasive paper with grit P24 from NORTON Abrasives

(b) A classical LEGO® baseboard

Figure 4.2: Two different roughness elements useful in wind tunnels

4.2.2.1 Sand covered surface (e.g. sandpaper)

Nikuradse (1933) [82] conducted many experiments on pipes uniformly covered with sand grains, yielding the conclusion $c_\infty = 8.5$, suggesting that:

$$\frac{h_0^{r,sand}}{h} \sim \frac{1}{30} \tag{4.23}$$

The height of the roughness elements h coincides with the "equivalent sand-grain roughness height" k_s and corresponds to the grain size. Moreover, this expression is very close to the expression, given by Schlichting (1937) [84], to define an “equivalent sand grain” for every rough surface: $k_s = 32.6 \cdot h_0^r$.

4.2.2.2 LEGO® baseboard

Counihan (1969) derived the following relation for LEGO® baseboard:

$$\frac{h_0^{r,baseboard}}{h} \sim \frac{1}{13} \tag{4.24}$$

This relation is derived considering that LEGO® boards and bricks have geometrically standardized properties (shown in Figure 4.3).

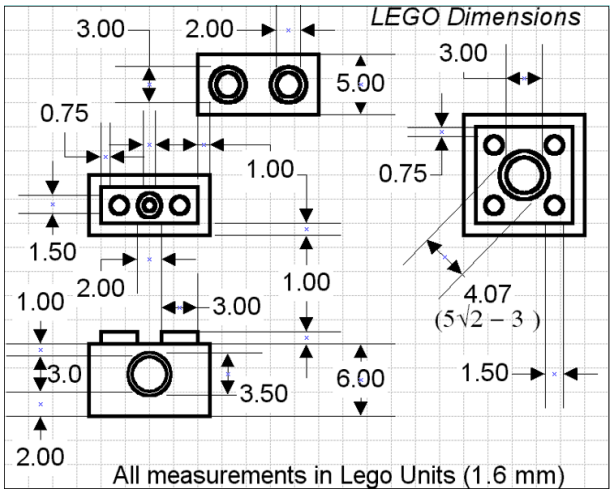

Figure 4.3: LEGO® elements geometry

4.2.2.3 Dynamically smooth surface

According to Raupach *et al.* (1991) [81], it is possible to define a roughness height h_0^r when the flow is dynamically smooth ($h^+ < 4$), even though it becomes dependent on the Reynolds number:

$$\frac{h_0^r}{h} \sim \frac{0.14\frac{\nu}{u_*}}{h} \sim \frac{0.14}{h^+} \tag{4.25}$$

4.2.3 Introduction of roughness in the wind tunnel

Two potential methods for simulating roughness in the wind tunnel were examined before the start of the experimental campaigns. The two possibilities taken into account were sandpaper and LEGO® baseboard, both already studied in the past (as mentioned in the previous sections). The experiments were carried out with the same mean velocity $U_{mean} = 15\ m/s$ and at the same location in the y direction (in the wind tunnel reference system). Firstly, near the center of the section ($y \approx 0$) to reduce the influence of the non-physical wind tunnel walls. After, at a distance of about 85 mm from the center, to evaluate the symmetry of the flow in the y direction (the width of the test section is 300 mm). Considering the same conditions, it was possible to compare the results of the two configurations.

It is important to mention that these preliminary measurements were taken in the old configuration of the SCL-PIV wind tunnel and at a distance of 1810 mm from the beginning of the rough surface (coincident with the start of test section). The results in terms of normalized mean velocity, turbulent intensity and streamwise length scales are presented in Figures 4.4 (Sandpaper) and 4.5 (LEGO® baseboard). In particular, the integral length scales are computed using two different methods. The zero crossing statistics method (Mora *et* Obligado, 2020 [85]) which also allows to compute the Taylor microscales. The other approach is based on the interpolation of the turbulence kinetic

energy spectrum ($E_{11}(k)$, where $k = 2\pi f/\overline{u}$ is the wave number) by using the von Karman model [13]. These two methods are carefully explained in Appendix A.

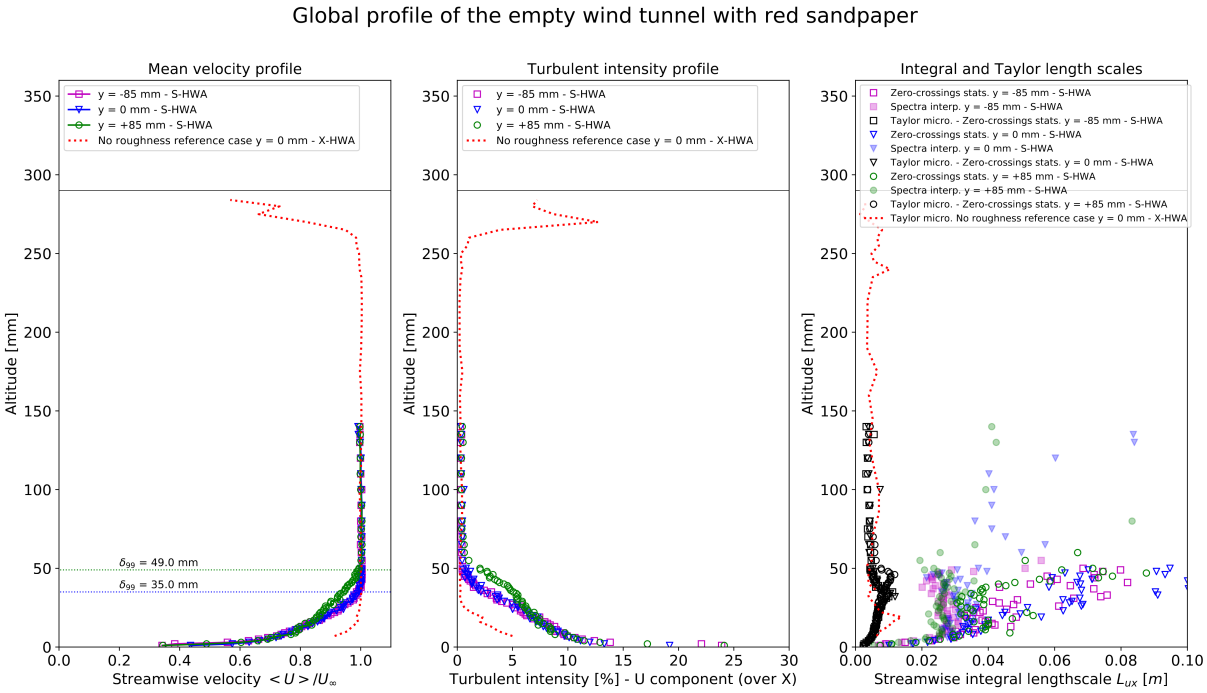

Figure 4.4: Results in terms of normalized streamwise velocity, turbulent intensity (%), integral length scales and Taylor microscale. The measurements were taken at $y = -85\ mm$, $y = 0\ mm$ and $y = 85\ mm$ with the red sandpaper at the wall.

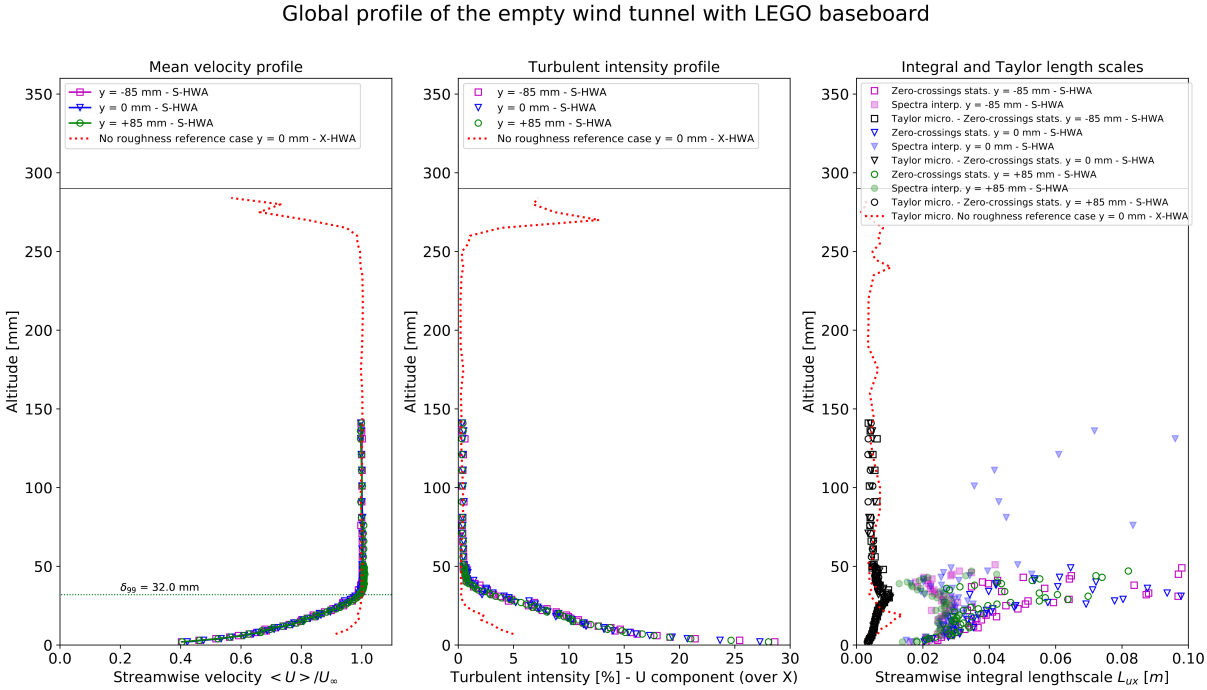

Figure 4.5: Results in terms of normalized streamwise velocity, turbulent intensity (%), integral length scales and Taylor microscale. The measurements were taken at $y = -85\ mm$, $y = 0\ mm$ and $y = 85\ mm$ with the LEGO® baseboard at the wall.

The results show that the LEGO® baseboard (Figure 4.5) is capable of producing a symmetric flow in the test section; indeed, the three profiles at various y positions precisely collapse. This is not the case for the sandpaper (Figure 4.4), where the profile measured at $y = 85\ mm$ shows a completely different boundary layer depth (δ), significantly larger than in the other two profiles.

The different behaviour of the two rough surfaces is due to the difficulty in sticking the sandpaper layer to the wall. Both LEGO® baseboard and sandpaper sheet were attached to the wall using double-sided adhesive tape. However, because the red sandpaper is so flexible, it can be difficult to prevent the formation of an air flow between it and the wall. This can have unpredictable effects on the results, altering the boundary layer height, the friction velocity, and the equivalent roughness height. Moreover, the red sandpaper layer from the wall cannot be removed without causing irreparable damage. Conversely, because the LEGO® baseboard is rigid, it may be removed and reused for several tests while still adhering efficiently to the wall and preventing air penetration.

For these reasons, it was decided to not use the red sandpaper anymore for the reproduction of the Earth's roughness in the wind tunnel.

4.3 Estimation of $\Pi(x)$, k_s and u_* from mean velocity profile

In subsection 4.1.3, a mathematical method for the computation of the normalized objective function $f_n^{+,prescribed}$ is presented. The $f_n^{+,prescribed}$ function is crucial for the grid's design since it will directly affect its geometry through the optimization algorithm described in subsection 4.1.2. However, to get the objective function, some quantities are necessary: the *roughness height* (h_0^r) and the *wake function* ($\Pi(x)$). This section describes a method for estimating these two crucial parameters, together with the *friction velocity* (u_*), in a turbulent flow over a rough surface using experimental data obtained from HWA measurements. The following approach, in particular, is used to estimate the *equivalent sandgrain roughness height* (k_s), which can be related to h_0^r through the Schlichting [84] relation: $k_s = 32.6 \cdot h_0^r$.

The two parameters k_s and u_* are strongly dependent on the surface roughness, while Π is theoretically more affected by the streamwise position x and more generally by the Reynolds number ($Re_x = \frac{U_\infty \cdot x}{\nu}$). The method has been applied to estimate the characteristics of the LEGO® baseboard by using the data obtained from experiments in the empty wind tunnel, without grids or other obstacles. The characterization of the new SCL-PIV empty test section was carried out at the velocity $U_{pitot} = 15\ m/s$ (detected by the Pitot tube upstream of the LEGO® baseboard). The HWA probe was positioned at a distance of about 1960 mm from the virtual grid, and approximately at the center of the section ($y \approx 0\ mm$). The goal was to reduce the influence of the non-physical wind tunnel walls. For the experiments with grids, the hot wire probe will be placed in the

same location in order to compare the results. The experiment was done using the Single Hot Wire Anemometry (S-HWA) in order to reach the region very close to the wall, which has a strong influence on the parameters u_* and k_s.

4.3.1 Mathematical methodology

Considering the "law of the wake" (2.3), the expressions for the functions $\omega\left(\frac{z}{\delta}\right)$ (2.4) and ΔU^+ (2.5) and knowing the z positions from measurements, it is possible to identify 4 unknowns: δ, $\Pi(x)$, k_s and u_*. However, using a standard technique in fluid mechanics, the number of unknowns may be reduced to three, by estimating δ (the boundary layer thickness) as the distance from the wall where the 99% of U_∞ is achieved, or in other words, where $U = 0.99 \cdot U_\infty$. The velocity of the undisturbed flow (U_∞) is derived by computing the average value of the last 10 measured velocities, since the mean velocity plot clearly shows that they are outside of the boundary layer.

The theoretical velocity can be easily derived from (2.3) knowing that $U^+ = U/u_*$, where U is the local velocity and in this case, is the theoretical velocity (U_{theo}) obtained using the "law of the wall".

$$U_{theo} = u_* \cdot \left[\frac{1}{\kappa}\ln\left(u_*\frac{z-d}{\nu}\right) + C - \Delta U^+ + \frac{\Pi(x)}{\kappa}\cdot\omega\left(\frac{z-d}{\delta}\right)\right]. \tag{4.26}$$

At this point, it is convenient to define a vector of the three unknowns as: $\overline{\chi} = [u_*, k_s, \Pi(x)]$ and to apply a "least squares method", for instance by using the ***minimize "SLSQP"*** Python *"scipy.optimize"* module, to minimize numerically the expression (4.27) and derive an estimate of the three unknowns. In particular, the Python ***minimize "SLSQP"*** was applied without imposing constraints and by only defining the lower bounds. The goal was to prevent negative solutions, which are not physical (except for $\Pi(x)$ which can assume negative values, as shown by Dogan, 2016 [86]).

$$F(\overline{\chi}) = \frac{1}{\delta}\int_d^{\delta+d}\left[U_{measured}(z) - U_{theo}(z,\overline{\chi})\right]^2 dz \tag{4.27}$$

Knowing $U_{measured}$ from the S-HWA data, estimating δ as previously explained and computing U_{theo} with the equation (4.26), a solution in terms of vector $\overline{\chi}$ and a fit of the experimental data are obtained.

4.3.2 Characterization of the wind tunnel with LEGO® baseboard

By applying the method explained in the previous section, the three parameters (k_s, u_* and $\Pi(x)$) of the LEGO® baseboard have been determined. The already mentioned Schlichting [84] relation can be used to derive h_0 knowing k_s.

This procedure required many trials and errors and proved that the measurement of these three quantities is particularly challenging and sensitive to uncertainties about the distance between the LEGO® surface and the first measured point (i.e., HWA initial position). Since this distance is measured manually in the SCL-PIV wind tunnel, it is difficult to achieve a very high degree of precision. However, after various attempts, satisfactory results were achieved. Figure 4.7 shows a comparison of normalized mean velocity profile, turbulent intensity, and integral length scales for the empty wind tunnel in the rough configuration (LEGO® baseboard) and the smooth configuration (Aluminium flat-plate). The two wind tunnel configurations are shown in Figure 4.6.

(a) Smooth configuration (Aluminium flat-plate). **(b)** Rough configuration (LEGO® baseboard).

Figure 4.6: The two wall configurations. The rough case consists in LEGO® baseboard glued to the aluminium flat-plate.

The results clearly demonstrate that the introduction of roughness increases the boundary layer depth (δ) from 40 mm to 63 mm. This is visible mainly in the velocity and turbulent intensity profiles but also in the Taylor microscales. The second important effect is an increase in the turbulent intensity in the boundary layer region. The least squares method leads to the findings and to the fit presented in Figure 4.8.

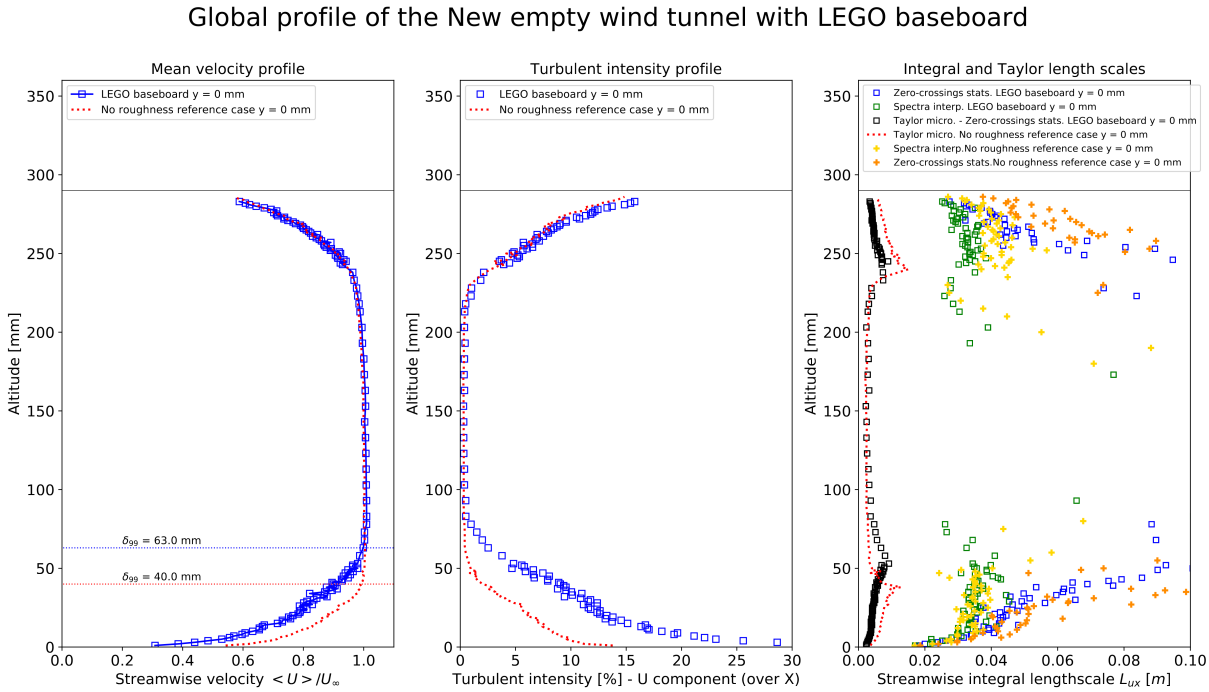

Figure 4.7: Results in terms of normalized streamwise velocity, turbulent intensity (%), integral length scales and Taylor microscale. The measurements were taken at $y = 0$ *mm* in the new SCL-PIV wind tunnel.

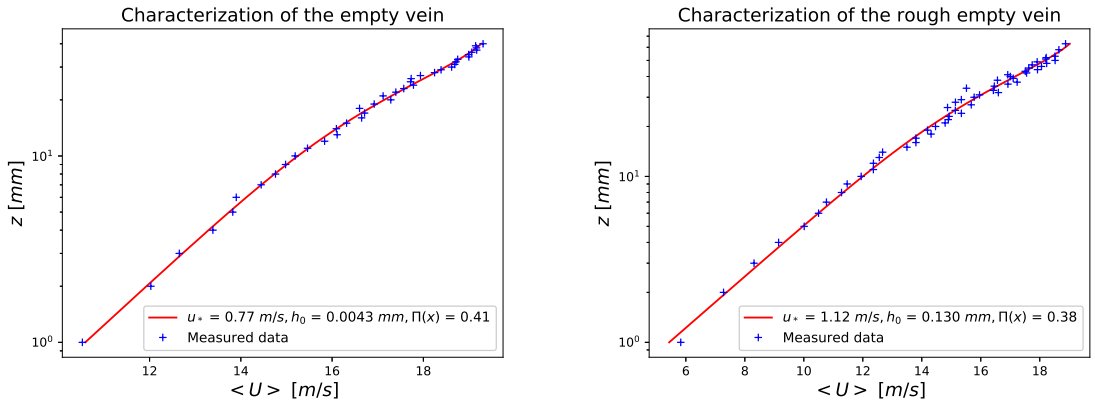

(a) Smooth configuration. **(b)** Rough configuration.

Figure 4.8: Fit of mean velocity profile obtained for the characterization of the empty wind tunnel using the least squares method.

It is now possible to highlight the differences between the two obtained boundary layers, introducing also the *"Momentum Reynolds number"* $Re_\theta = \frac{U_\infty \theta}{\nu}$, where θ[1] is the *"momentum thickness"*, useful for the calculation of skin friction losses. Another important parameter is the *"Displacement Reynolds number"* $Re_{\delta^*} = \frac{U_\infty \delta^*}{\nu}$, where δ^*[2] is the *"displacement*

[1] $\theta = \int_0^\delta \frac{U}{U_\infty}\left(1 - \frac{U}{U_\infty}\right) dy$, where U is the streamwise mean velocity

[2] $\delta^* = \int_0^\delta \left(1 - \frac{U}{U_\infty}\right) dy$

thickness", which is introduced to compare the real flow and an equivalent inviscid flow. From these two parameters, it is possible to obtain the *"shape factor"* $H = \delta^*/\theta$ which gives information about the boundary layer conditions, typically for a turbulent boundary layer $H = 1.2 - 1.5$.

Table 4.1 offers a comparison between the natural boundary layer produced in the wind tunnel with and without roughness at the wall (θ and δ^* are computed numerically by using the *"trapezoidal method"*):

Table 4.1: Comparison between the two rough configuration of the wind tunnel.

Configuration	$y[mm]$	$u_*[m/s]$	$h_0[mm]$	$\Pi(x)$	Re_θ	Re_{δ^*}	H	$\delta_{99}[mm]$
Smooth	0	0.77	0.0043	0.41	5188	6650	1.28	40
Rough	0	1.12	0.130	0.38	9236	13674	1.48	63

The results presented in Table 4.1 are satisfactory. Indeed, the roughness heights for the two cases $h_0^{smooth} = 0.0043\ mm$ and $h_0^{LEGO} = 0.13\ mm$ don't differ a lot from the values available in the literature $h_0^{smooth} = 0.0025\ mm$ [81] and $h_0^{LEGO} = 0.123\ mm$ [16]. According to Chauhan *et al.* (2009) [87], $\Pi(x) \to 0.42$ for high Re_x numbers (of the order of 10^7). Since the experiment in the rough configuration was characterised by $Re_x \approx 2 \cdot 10^6$, the estimated values $\Pi(x)^{smooth} \approx 0.41$ and $\Pi(x)^{LEGO} \approx 0.38$ seem to be physical.

Finally, the shape factor H shows that in both cases the boundary layer is turbulent, as expected. The boundary layer is wider in the rough configuration than in the smooth case, and as a result, the momentum and displacement thickness are greater. This results in higher Reynolds number values.

4.3.3 Roughness height of the simulated full-depth ABL

The estimated h_0 of the LEGO® baseboard has to be scaled to obtain the *roughness height* of the real ABL. Following the recommendations of Counihan (1975) [88], the average height of a neutral ABL can be taken as $\delta^{ABL} \approx 600\ m$, while the boundary layer thickness that we want to generate in the wind tunnel is equal to $\delta^{SCL} \approx 0.145\ m$. Therefore, the required scale is $S = \delta^{ABL}/\delta^{SCL} \approx 4100$, which leads to $h_0 \approx 0.53\ m$ which is representative of the *"Very rough"* configuration according to the Davenport's classification [29] (see Figure 2.5b).

4.4 Grids and spires production

In the preceding sections, the whole procedure for designing full or partial section grids, which attempts to create a certain mean velocity profile in a wind tunnel, was discussed. The two methods shown in Figures 4.1a and 4.1b can be adapted to design spires that provide the same objective grids' flow.

From the estimation of h_0 and $\Pi(x)$ (Table 3.1) some conclusions can be made:

- The estimated LEGO® baseboard *"roughness height"* is really close to the one measured by Counihan (1969) [16], therefore $h_0^{LEGO} = 0.130\ mm$ was chosen as input for the grids design;
- As a first approximation, the asymptotic value suggested by Chauhan *et al.* (2009) [87] $\Pi(x) = 0.42$ was used for the grids design. The reason is that the difference in terms of prescribed velocity profile was negligible for modest variations of $\Pi(x)$ (results not shown);

The methods shown in Figure 4.1 employ these two values as input together with the mean velocity imposed in the wind tunnel, which in our studies is always $u_{mean} = 15\ m/s$.

In the current project, two set of atmospheric flow generators were designed and tested in the SCL-PIV wind tunnel at Onera Lille. The two set of devices led to two main experimental campaign, whose results are presented and discussed in Chapter 5. In the first experimental campaign only MIG grids were tested, while spires were introduced during the second one.

4.4.1 Definition of the four grid configurations

In the current project, four different grid configurations were designed to be inserted into the SCL-PIV wind tunnel slot (see Figure 3.2). To facilitate the insertion, a 3-side frame is built around the grid.

The four grids share the same geometry for the horizontal bars (width $T_b = 1.66\ mm$ and depth $d_b = 10\ mm$). The values of T_b and d_b are arbitrarily selected in order to minimize the deflection of the vertical bars, caused by the wind during the experiments. This decision has no impact on the velocity profile generated by the grid since, as explained in paragraph 4.1.2, the vertical bars' geometry will adjust to them preserving the required objective function.

The sets of four grids tested in the two experimental campaigns present different geometric characteristics. However, they share the same objective mean velocity profile. For this reason, the same numbers are used to identify the grids with the same objective profile, in the two experimental campaigns:

1. Full-section grid producing a mean velocity profile following the law of the wake (Figure 4.9a left);
2. Partial-section grid producing the law of the wake profile in the lower half of the section without any constraint in the upper part (Figure 4.9b left);
3. Full-section grid producing a law of the wake profile in the lower half section and a constant velocity profile in the upper half (Figure 4.9c left);
4. Partial-section grid producing a law of the wake profile in the lower half section and a constant velocity profile in the upper half (Figure 4.9d left);

Overall, height MIG grids were designed and tested in wind tunnel. In order to distinguish the grids tested in the two experimental campaigns, the letters "a" and "b" are utilized to refer to the first and second set of grids, respectively.

Figure 4.9 shows the sketches of the of grids "a" and the actual velocity profile that they attempted to reproduce. In particular, the pictures show the real turbulent flow created over a rough surface, which cannot be exactly recreated by the law of the wake. The latter, indeed, gives only an approximation of the "Roughness sub-layer" region.

The four grids design and their objective functions have been chosen to investigate the potentiality of the McCarthy (1964) [21] method. This is applied to partial and full-section grids for the reproduction of a full-depth turbulent boundary layer. More specifically, each grid has a specific task:

- The grid 1 represents the reference for the other three grids, when the velocity profile is scaled with the boundary layer height;
- The grid 2 represents an application of the full-section grid design process (described in Figure 4.1a) to a partial-section grid, without taking into account the free stream flow. The goal is to see if the latter has a significant impact on the artificial boundary layer flow;
- Grids 3 and 4 have the same objective function enabling a comparison between a full-section grid and a partial-section grid (which have benefits in terms of production costs, weight, and wind tunnel obstruction). It is also interesting to compare the profiles created by these grids and grid 2;
- Although the objective velocity profiles of the two partial-section grids and the two full-section grids differ, they should collapse into the same curve when scaled with the boundary layer depth δ. The reason is that the produced boundary layers are expected to be self-similar.

As explained in section 3.3.1, the grid introduces a perturbation both upstream and downstream of itself, which is strongly related to the obstruction given by horizontal and vertical bars. In order to have comparable obstructions, the grids must have the same mean blockage ratio σ_{mean}, even though their geometries and objective functions differ. Grids 1, 2 and 3 were designed by using the algorithm shown in Figure 4.1a, so it was possible to choose the desired σ_{mean}. Grid 4 is designed using the procedure described in Figure 4.1b. Therefore, the σ_{mean} is imposed by the optimization code and can only be controlled by modifying the number of grid's layers. As a result, the number of layers was the first parameter to be chosen.

The next sections describe the geometric characteristics of the two set of grids ("a" and "b"), tested in the two experimental campaigns. The differences between the two and the reasons that led to the new grids design are emphasized.

4.4.1.1 Geometric characteristics of grids "a"

In the grid design algorithm there is always a trade-off between the blockage ratio σ which should not be higher than a certain threshold (σ_{max}) [61] and the number of layers which should be sufficient to provide a satisfactory resolution in the boundary layer region. In the first stage, the main goal of the design was to obtain a good resolution in the region close to the wall. In grids "a", a power law (with exponent equal to 3.5) was used to define the height of each layer (h_n), in order to have more layers in the inner region and fewer layers in the outer region of the boundary layer. This resulted in a large blockage in the area next to the wall, where high σ values were achieved.

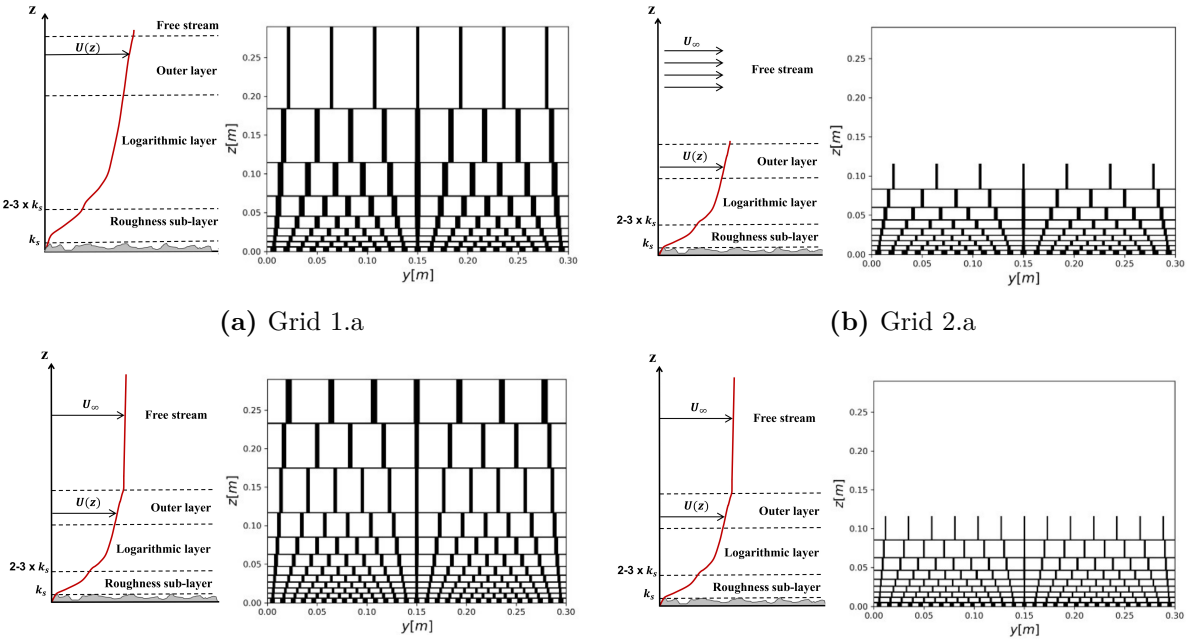

(a) Grid 1.a

(b) Grid 2.a

(c) Grid 3.a

(d) Grid 4.a

Figure 4.9: Schemes of the four grids and turbulent velocity profiles over a rough surface. The boundary layer sketch is inspired from Kadivar (2021) [12].

As previously mentioned, the number of layers was the first parameter to be chosen. Past preliminary experimental tests suggested that 9 layers are sufficient to provide a smooth objective velocity profile in the logarithmic region of the boundary layer. As a result, grids 1.a, 2.a, and 4.a were produced with 9 layers, whereas grid 3.a was constructed with 12 layers. Indeed, since a high resolution is not required in the outer layer and free stream region, grid 3.a was specifically separated into two parts: the bottom portion (occupying the 40% of the section) made up of 9 layers (indicated as l in Table 4.2) and the higher portion (occupying the remaining section) made up of just 3 layers. The lower portion is primarily responsible for reproducing the boundary layer profile, hence the number of layers has been set to be equivalent to that of the other grids.
More precisely, these layers have been designed to have the same height as in the grid 4.a, enabling a direct comparison between the two (see Figure 4.9).

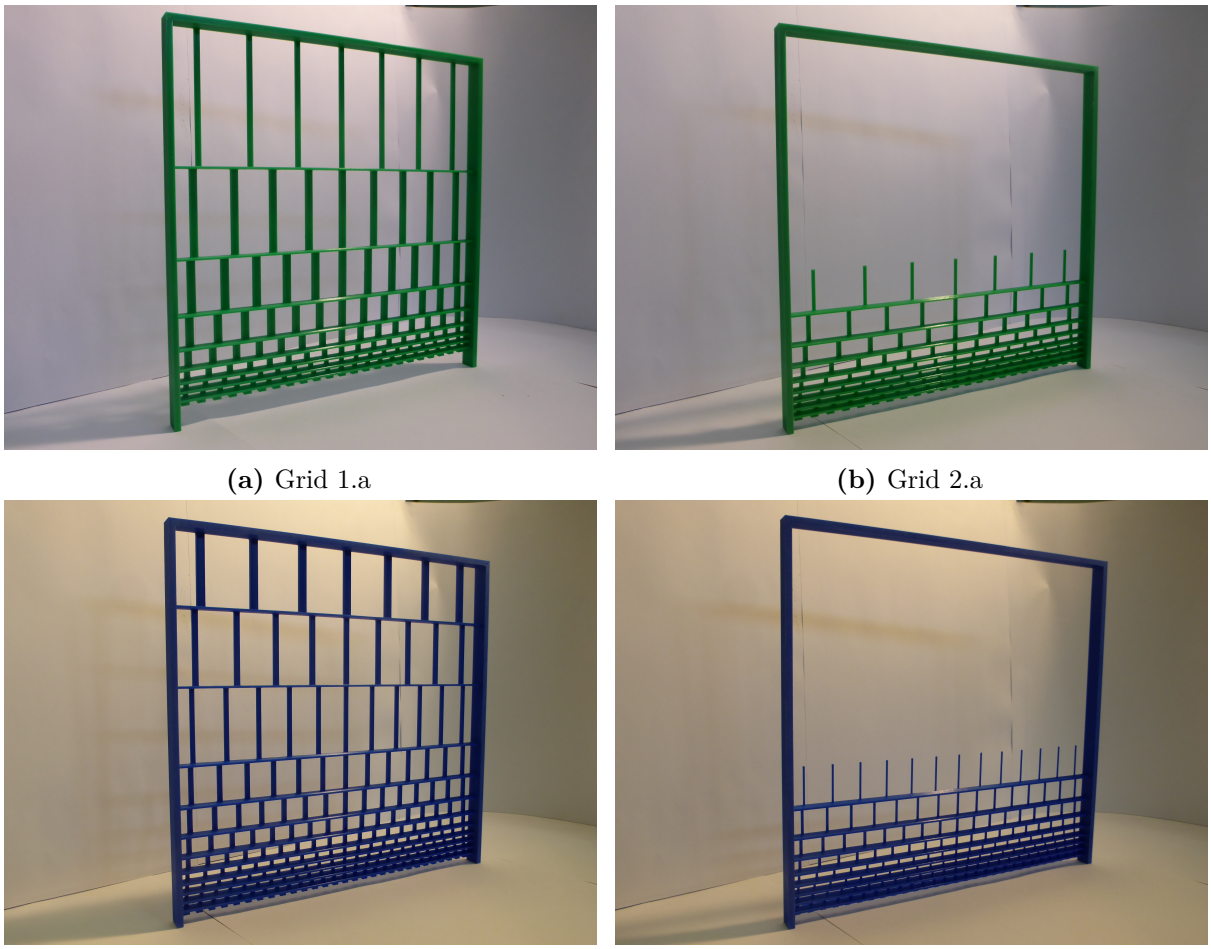

(a) Grid 1.a **(b)** Grid 2.a

(c) Grid 3.a **(d)** Grid 4.a

Figure 4.10: Pictures of the four 3D printed grids.

After the aforementioned pre-design study, the grids were produced by additive manufacturing. Figure 4.10 shows the 3D printed grids in PLA with 100% fill.

4.4.1.2 Geometric characteristics of grids "b"

The experiments of the previously described grids showed no satisfactory results in terms of mean velocity profile (as shown in Figure 5.2). The post processing of the experimental data (shown in Chapter 5) revealed that one potential cause may have been the high *blockage ratio* σ and *resistance coefficient* K in the vicinity of the wall. In particular, the Reynolds stress profiles (see Figure 5.4) show that the significant obstruction, registered in the first MIG grids' layers, may have caused jet-like structures near the wall.

This can happen in grid-generated flows when the maximum blockage ratio σ_{max} exceeds a certain physical threshold ($\sigma \approx 0.4$), suggested by Rose (1966) [61]. The distribution of blockage ratio throughout the various levels of "grid 3.a" is shown in Figure 5.6. It is clearly visible that in the first three grid layers $\sigma > 0.4$. However, this condition should be avoided in the McCarthy model (1964) [21] because it can affect the produced mean velocity profile.

The grids "b" design aims at reducing as much as possible the *blockage ratio* in the vicinity of the wall, in order to not exceed the physical threshold .

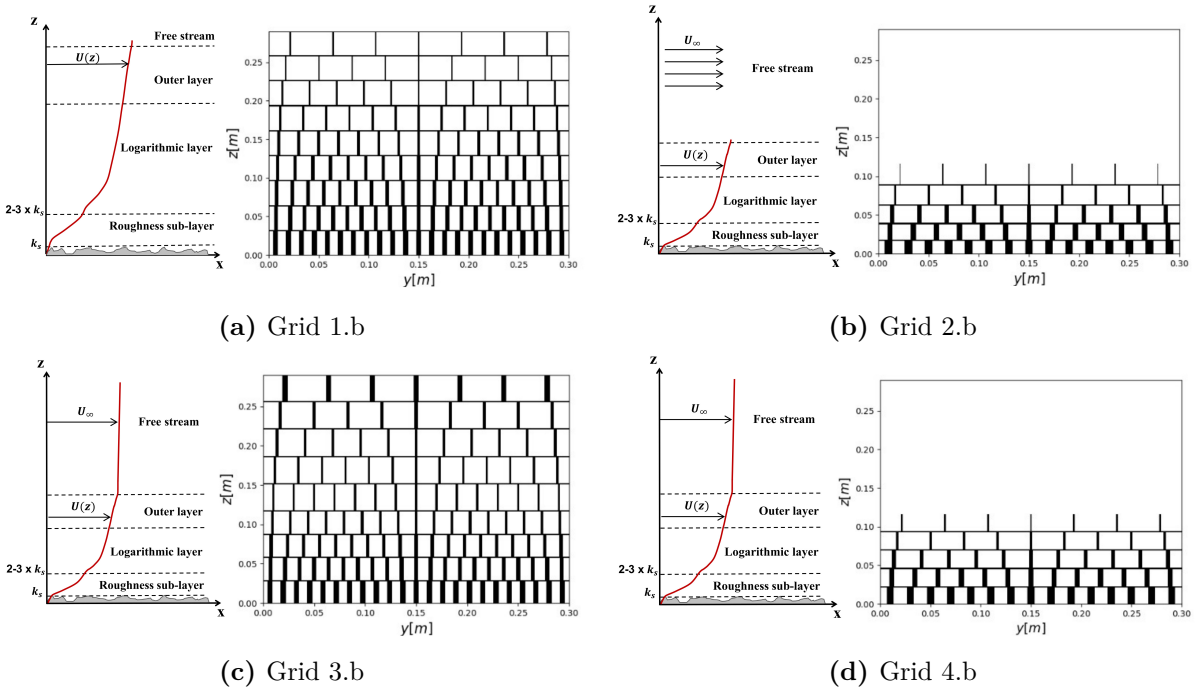

(a) Grid 1.b

(b) Grid 2.b

(c) Grid 3.b

(d) Grid 4.b

Figure 4.11: Schemes of the new four grids and turbulent velocity profiles over a rough surface. The boundary layer sketch is inspired from Kadivar (2021) [12].

In order to reduce the grids obstruction near the wall, the following modifications were implemented:

- The *mean blockage ratio* have been reduced from $\sigma_{mean} = 0.22$ to $\sigma_{mean} = 0.2$;
- The number of grids levels in the boundary layer region was reduced from 9 to 5 in grids 2.b and 4.b and from 9 to 4 for grid 3.b, while grid 1.b keeps the same number of levels as grid 1.a;
- The distance between the first horizontal bar and the wall has been increased to reduce the blockage ratio and to avoid a possible interaction with the LEGO® baseboard;
- In grids 1.b, 3.b and 4.b, the layers are equally spaced, resulting in a uniform resolution for the mean velocity profile over the whole wind tunnel section (see Figures 4.11a, 4.11c and 4.11d);
- In grid 2.b, the heights of the levels (h_n) increase progressively with the distance from the wall, following a power law with an exponent of 0.8 (Figure 4.11b). This decision was taken after many trials to ensure the required number of layers and a sufficient mechanical resistance of the vertical bars;

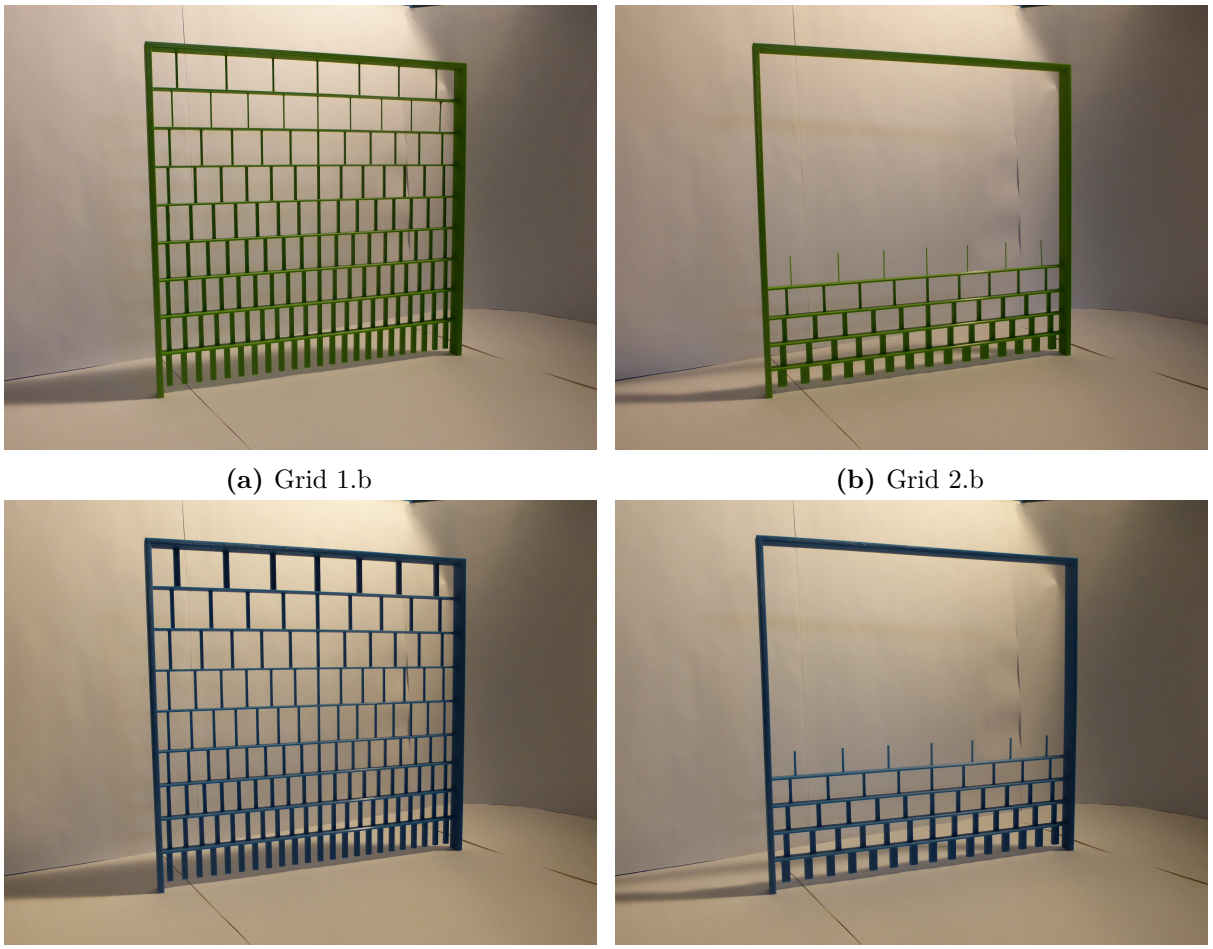

(a) Grid 1.b **(b)** Grid 2.b

(c) Grid 3.b **(d)** Grid 4.b

Figure 4.12: Pictures of the four 3D printed grids.

- The number of vertical bars in grid 4.b has been reduced to increase their width and prevent deflections;

These modifications are summarized in Table 4.2, where it is shown that σ_{max} and K_{max} are much smaller in the second set of grids.

The same material and process applied for the previous set of grids were used to 3D print these grids, which are presented in Figure 4.12.

4.4.2 Definition of the spires

Because the eddies produced by passive grids are proportional to their mesh size, which is often much smaller than the wind tunnel section, they are known to create turbulent flows with modest turbulence intensities. Indeed according to Laws & Livesey (1978) [79], the smaller are the turbulent structures the faster they decay. The higher is the decay rate the smaller is the flow's turbulence intensity. This is a complication since the Atmospheric Boundary Layer (ABL), which is intended to be replicated in a wind tunnel, is characterised by high turbulence that grows with surface roughness [7].

This limitation can be partially overcome by using spires instead of grids to reproduce the ABL in wind tunnel. Irwin (1981) [18] provided instructions for the design of simple spires (just triangles) to tailor the mean velocity profile. He showed, a posteriori, that the produced turbulent intensity profiles were representative of a real ABL (see subsection 2.5.3). However, his approach was empirical and limited to the specific flow configuration described by the "power law" (2.1). The spires represent also an interesting object of study because they produce larger vortex structures than the grids, which can interact in a different way with the LEGO® baseboard.

In the current project, the McCarthy model [21] and the MIG design code are adapted to create spires which can yield a prescribed mean velocity profile. The model utilized to derive this new device is the partial-section method summarized in subsection 4.1.2, while the objective velocity profile is the same used for grids 3 and 4, enabling a direct comparison of the results obtained with the three approaches.

The first design step consists in removing the horizontal bars to obtain the desired triangular shapes, in other words this means to impose $T_b = d_b = 0$. Then, the algorithm summarized in Figure 4.1b is followed and the same inputs are provided, except for the number of layers (l and N), the number of vertical bars at each n level (c_n) and the height (H) of the spires:

- To convert a discrete structure (MIG grid) into a continuous one (spires), the number of effective layers (l) must be increased by around two orders of magnitude ($l = 500$ was chosen for the project);
- The effective height is chosen following approximately the empirical law introduced by Irwin (1981) [18]:

$$H = \frac{1.39 \cdot \delta}{1 + \alpha/2} \tag{4.28}$$

  where δ is the required boundary layer height and α is the exponent of the power law (2.1). Then, the estimated h_0 of the LEGO® baseboard has to be scaled to obtain the *roughness height* of the real ABL. The computation was carried out in subsection 4.3.3, considering a scaling factor $S \approx 4100$. The scaled roughness height is $h_0 \approx 0.53\ m$ which is representative of the *"Very rough"* configuration, according to the Davenport's classification [29] (see Figure 2.5b).

  The corresponding α can be computed using the relation fitted experimentally by Counihan (1975) [88]:

$$\alpha = 0.096 \cdot log_{10}(h_0) + 0.016 \cdot log_{10}^2(h_0) + 0.24$$

  which leads to $\alpha \approx 0.215$. Plugging this value into Equation (4.28), it is possible to get the relation between the spires height and the prescribed boundary layer depth:

$H \approx 1.25 \cdot \delta$. Since Equation (4.28) is empirical and limited to a specific geometry, the height of the spires is chosen to be equal to the prescribed boundary layer depth ($H = \delta$);

- The number of spires is controlled by the c_n parameter which must be constant. To be consistent with the grid design, c_n is chosen to be odd in order to have a spire in the centre of the test section and a symmetric structure around it. The number of spires is chosen in order to meet the geometric proportions suggested by Irwin (1981) [18]. He stated that if d is the distance between the tips of two adjacent spires and H their heights, then $d \approx H/2$. The latter condition can't be exactly achieved with an odd number of spires, however the choice of $c_n = 5$ enables to get close to the requirement, because $H = 145\ mm$ and $d = 60\ mm$ (as shown in Figure 4.13a).

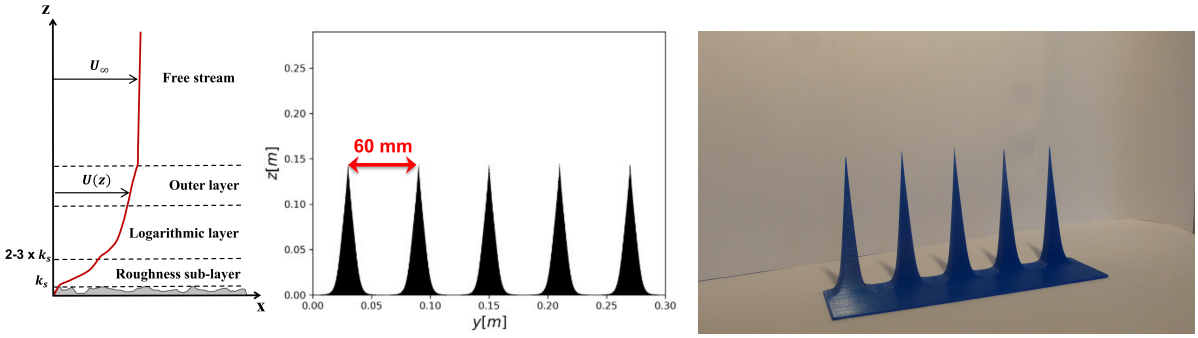

(a) Schemes of the spires and turbulent velocity profiles over a rough surface (adapted from [12]).

(b) Picture of 3D printed spires.

Figure 4.13: Sketch and picture of the spires.

4.4.3 Comparison of the geometric characteristics

A comparison of the main characteristics of the devices tested in the wind tunnel is given in Table 4.2. As shown in the table, the algorithm enables to choose independently the grid's overall height and the boundary layer depth δ. One of the post-processing goals is to discover if the measured boundary layer has the expected height.

Table 4.2: Main geometric characteristics of grids and spires.

Device	N	l	$H[mm]$	σ_{mean}	σ_{max}	K_{max}	$\delta[mm]$	$h_0[mm]$
Grid 1.a	9	9	290	0.218	0.556	4.52	290	0.13
Grid 2.a	9	9	116	0.218	0.539	4.09	116	0.13
Grid 3.a	12	9	290	0.218	0.563	4.74	145	0.13
Grid 4.a	12	9	116	0.215	0.511	3.48	145	0.13
Grid 1.b	9	9	290	0.200	0.408	1.92	290	0.13
Grid 2.b	5	5	116	0.200	0.411	1.95	116	0.13
Grid 3.b	9	4	290	0.200	0.414	1.99	145	0.13
Grid 4.b	9	5	116	0.210	0.379	1.63	145	0.13
Spires	510	10	145	0.181	0.800	31.3	145	0.13

The most important difference between the two set of grids concerns the values of σ_{max} and K_{max}. Indeed, for the "b" grids the maximum *blockage ratio* σ_{max} is much closer to the threshold of 0.4 suggested by Rose (1966) [61]. While in the new set of grids, the maximum *resistance coefficient* K_{max} (dependent of σ_{max}) decreases by a factor of more than two. In order to reduce these two parameters, the prescribed mean *blockage ratio* have been decreased from $\sigma_{mean} \approx 0.218$ to $\sigma_{mean} \approx 0.200$ in the second set of grids.

The spires present a totally different geometry which creates a very large obstruction in the region close to the wall, where σ and K reach values much higher than those of the grids. However, the mean blockage ratio obtained using spires is lower.

Chapter 5

Results of the experimental campaigns

This chapter presents and evaluates the findings from the two experimental campaigns that allowed to investigate the flow produced by the grids and the effect of adding artificial roughness to the wall. As previously explained in section 4.4, two main set of grids and spires with identical objective were designed.

During the first experimental campaign, the first set of grids was studied in the two wall configurations with and without LEGO® baseboard (see Figure 4.6). The second campaign focused on the analysis of the new set of grids and spires in the same roughness conditions, with objective of improving the results obtained during the previous campaign.

The following sections will present the results taken in the new SCL-PIV wind tunnel configuration (see section 3.1.1) which has three windows enabling the exploration of the flow through a total streamwise distance of 1950 mm (for the X-HWA) and 1960 mm (for the S-HWA) from the grid insertion slots. These windows are closed by adaptable wooden panels with slots of different orientations depending on the required profile.

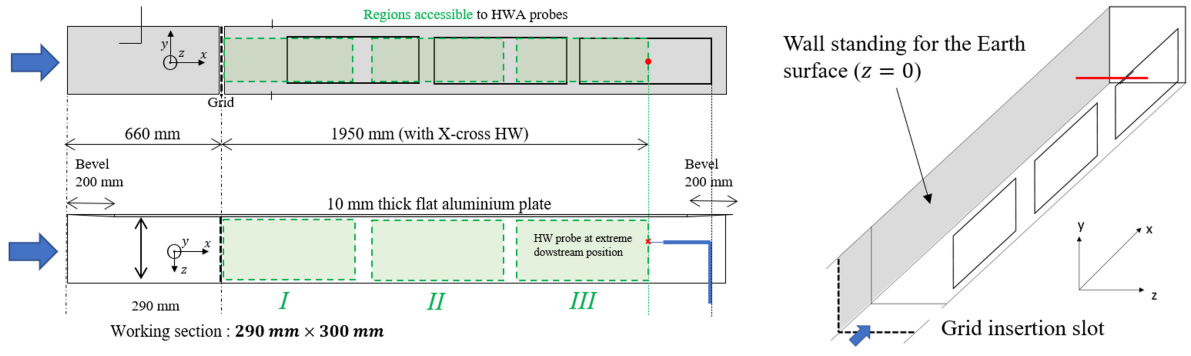

Figure 5.1: Schematic visualization of the wind tunnel working section. The *"IIIT9-center"* profile is highlighted in red

Figure 5.1 shows a sketch of the wind tunnel test section highlighting the position of the X-HWA probe. The normal-wall profiles were studied at the furthest possible

position from the grids, in order to reach the turbulence homogeneity which is required for the McCarthy model [21]. This was possible using the panel with vertical slots and inserting the probe in the furthest available slot (the ninth); this profile is referred to as *"IIIT9-Center"* and it is highlighted in Figure 5.1. The image solely depicts the X-HWA configuration. However, the S-HWA setup is comparable to the X-HWA one, with the exception that it uses the sixth slot of the wooden panel, since the probe supports in the two configurations have different lengths. The profile measured with the S-HWA probe is thus referred to as *"IIIT6-Center"*.

The experiments were carried out with the same reference velocity used for the characterisation of the empty vein (i.e. $U_{pitot} = 15\ m/s$) and at the same location in the y direction, in particular near the center of the section ($y \approx 0$) to reduce the influence of the non-physical wind tunnel walls.

5.1 First experimental campaign

The first experimental campaign started with the analysis of the flow produced by the first four grids (presented in 4.4.1) in the smooth wind tunnel configuration. The investigation then continued in the rough configuration.

The following goals guided the post-processing of the data measured in the wind tunnel experiments:

- The key objective of the internship is to control the mean velocity profile in order to reproduce a full depth atmospheric boundary layer in a wind tunnel. Therefore, the mean flow profile is the first flow quantity to be analyzed. The goal is to see if MIG grids and spires, designed using the McCarthy (1964) model [21], are capable to reproduce a full-depth boundary layer;
- It is necessary to compare the flow's characteristics acquired using partial and full-section grids to see whether the free stream has an impact on the artificial boundary layer flow;
- It is crucial to understand if the boundary layer depth and the grid's geometric height can be controlled independently;
- The turbulence intensity, the integral length scales and the Reynolds stresses (described in section 2.5.2) have to be analyzed and compared for the four grids, in order to comprehend physically the flow's behaviour;
- The interaction between grid and LEGO® baseboard must be studied, especially in the region near the wall;

5.1.1 Analysis of the normalized mean velocity profiles

Figure 5.2 shows a comparison of the normalized mean velocity profiles produced by the four grids "a". The distance from the wall (z) is scaled with the estimated boundary layer depth (δ_{99}) and the mean velocity $\langle U \rangle$ with the measured undisturbed velocity (U_∞). Moreover, the logarithmic scale is employed for the z/δ_{99} axis to better visualize the logarithmic and the outer layers, as well as the interaction between the wall and the artificial boundary layer flow. The analysis focuses on the boundary layer region, because the mean velocity profile is normalized by U_∞ leading to a perfect match with the objective profile in the free stream region.

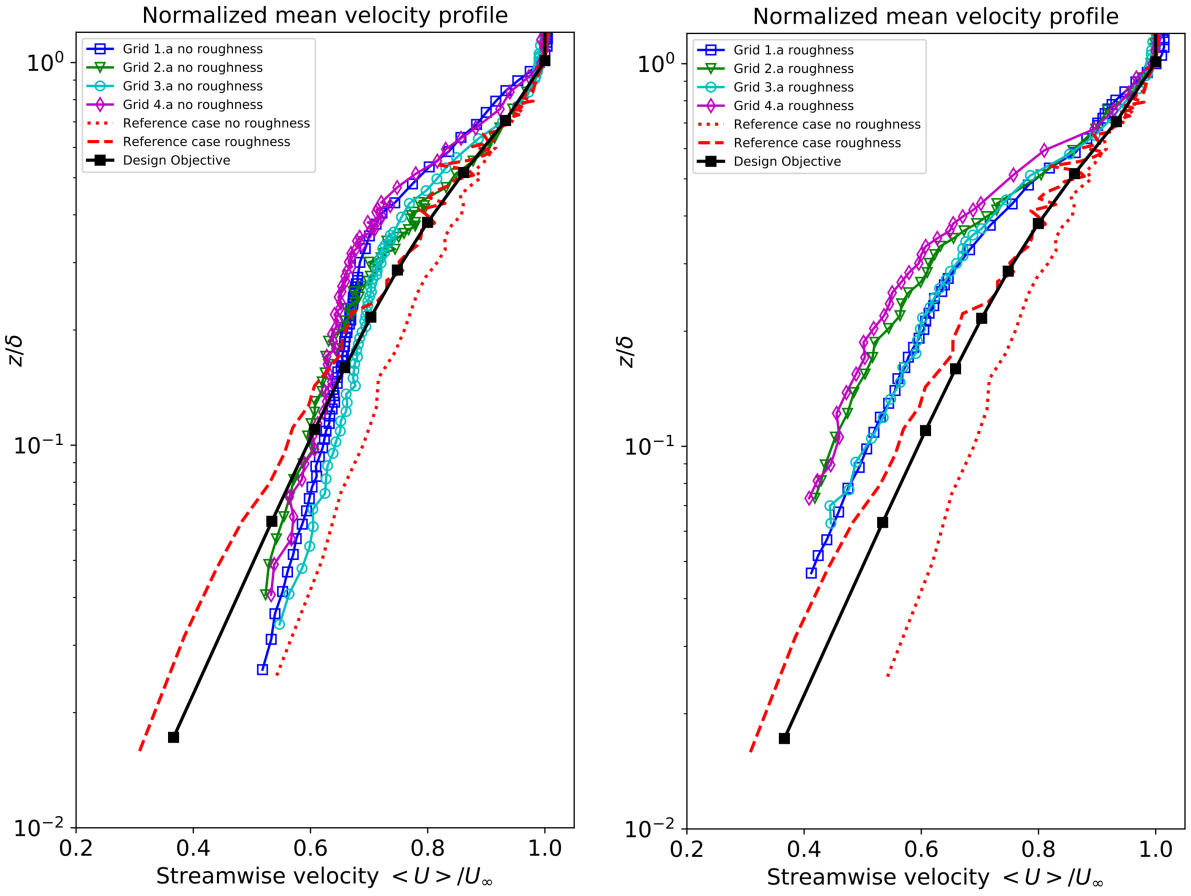

(a) Smooth configuration. **(b)** Roughness configuration.

Figure 5.2: Comparison of the normalized mean velocity profiles in the boundary layer produced by grids "a". The measurements were taken using the X-HWA.

5.1.1.1 Smooth configuration

The measurements by X-cross hot-wire at the *"IIIT9-Center"* profile (see Figure 5.1) downstream of each grid is presented in Figure 5.2a.

In the boundary layer it is possible to distinguish two main regions: a wall-region of approximately the same height as the natural boundary layer growing in empty vein

configuration, and an outer region (roughly between $0.4 \times \delta$ and δ). In both regions the mean flow profile show a logarithmic evolution.

The grids have been designed to be in roughness similarity with the LEGO® baseboard, in order to satisfy the Jensen similarity criterion (see subsection 2.5.1). Therefore, the measured u_* and h_0 in the grid-generated flow are smaller than those in the objective profile and the velocity higher than expected in the wall-region. Moreover, near the wall the grid-generated normalized velocity profiles get close to the reference case obtained for the empty vein smooth configuration (dotted red line). However, this roughness incompatibility at the wall does not explain completely the error in the outer region, where the mean velocity is smaller than expected (particularly in grids 1 and 4).

The experiments with roughness at the wall are thus required to understand if the problem comes from the grid design or from the lack of similarity in the wall-region.

5.1.1.2 Rough configuration

The experiments are repeated in the same conditions as before but with the LEGO® baseboard glued to the wall. Figure 5.2b shows that the objective and observed velocity profiles appear to be slightly closer in the outer region, despite roughness has minimal influence above the equivalent boundary layer height developing in the no-grid condition. However, closer to the wall, the roughness does not seem to correct properly the h_0 discrepancy with the design input observed at the same altitudes without roughness. The roughness appears to have a too strong decelerating effect rather than the expected corrective effect that would result in similar parameters between the outer and wall regions.

A possible explanation could be that the objective function underestimates the effective roughness height (h_0) at the wall. Moreover, the full-section grids' normalized profiles are becoming closer to the "empty wind tunnel roughness reference case" (dashed red line) as they get closer to the wall. This was not expected because the four grids were designed to have the same h_0 of the LEGO® baseboard alone, rather than the same h_0/δ.

To better understand the reasons of the errors in the mean velocity profile, the Turbulence intensity and the Reynolds stresses profiles are studied in the two roughness configurations.

5.1.2 Turbulent intensity analysis

The streamwise turbulence intensity corresponding to the four grids and measured at the location “IIIT9-Center” (see Figure 5.1) is presented in Figure 5.3.

As it was the case for mean flow profiles, the outer-layer and the free stream region are very weakly affected by the roughness change. For both configurations, the turbulence is too weak compared to the atmospheric requirements in the region sufficiently far from the wall. The grid 1 stands out because it ensures a turbulent intensity near to 5% also in the outer layer, even if the flow does not seem to have reached completely the turbulence

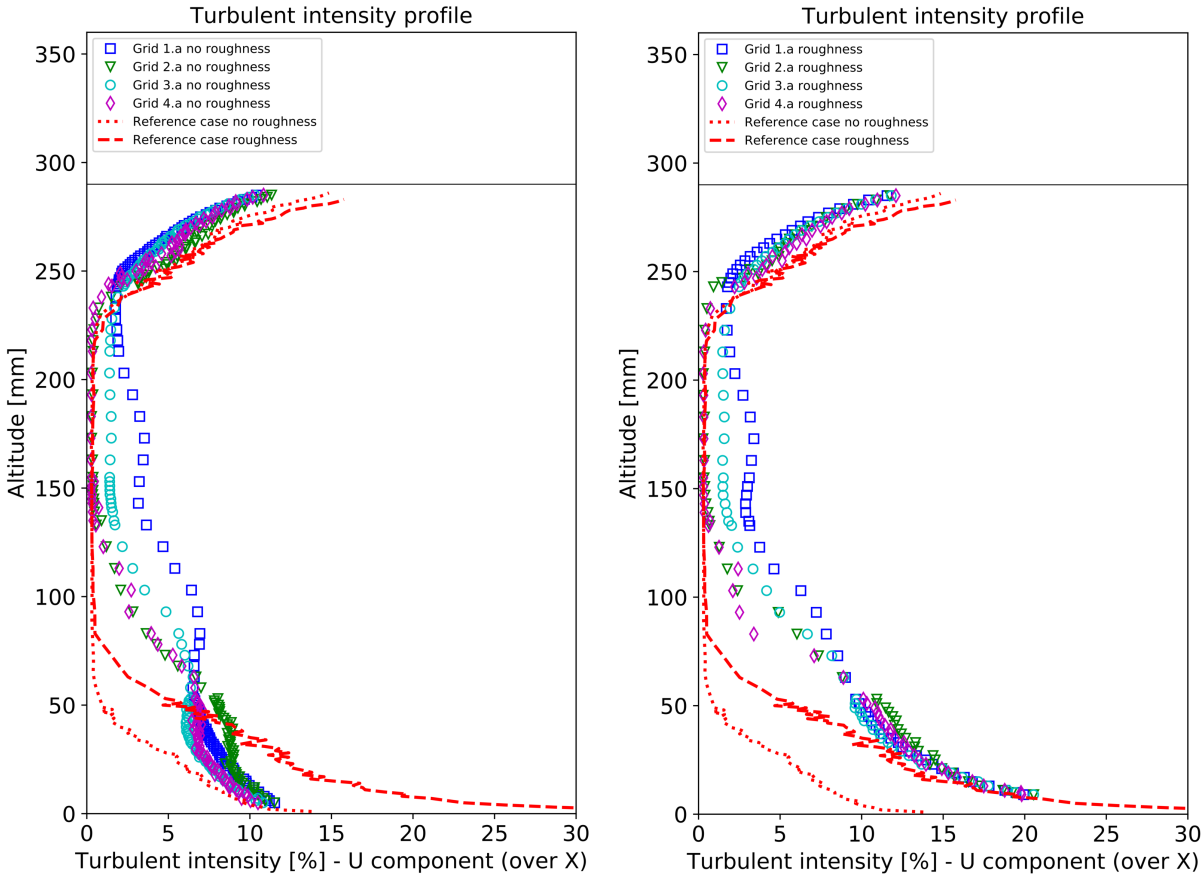

(a) Smooth configuration.

(b) Roughness configuration.

Figure 5.3: Comparison of the turbulent intensity profiles achieved with grids "a". The measurements were taken using the X-HWA.

homogeneity.

The turbulence intensity near the wall is much larger when the roughness at the wall is added. It appears that in the wall region the turbulence is regulated only by the wall, indeed the profile obtained with and without LEGO® baseboard follow the respective empty-vein characterisation trends.

A positive achievement is that the grids seems to increase the turbulence intensity generated solely by roughness in the empty vein (red dashed line). However, a crucial limitation of partial-section grids is highlighted: they cannot increase the turbulence intensity in the empty portion of the wind tunnel section.

5.1.3 Reynolds stresses analysis

The Reynolds stresses produced by the grids are compared in Figure 5.4, where the region close to the wall is highlighted. This region shows an unexpected behaviour in both the roughness configurations of the wind tunnel. In fact, moving from the outer to the inner region of the boundary layer, the Reynolds stresses' absolute value first increase, then it reduces and finally it increases again as the wall is approached. This creates a "S-shape"

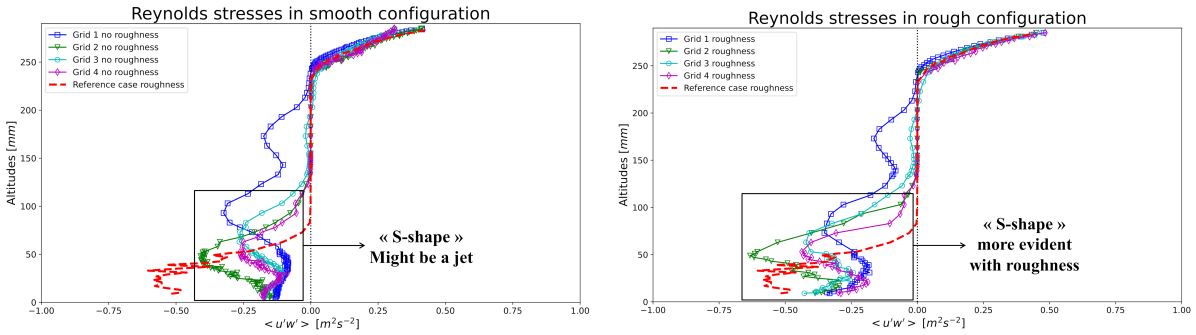

(a) Smooth configuration. **(b)** Roughness configuration.

Figure 5.4: Comparison of Reynolds stresses produced by the grids "a" with and without LEGO® baseboard on the wall. The measurements were taken using the X-HWA.

which is not visible in the empty wind tunnel with roughness, suggesting that it is caused by the grids. However, the combination of grids and LEGO® baseboard makes even clearer this phenomenon.

This shape of the Reynolds stresses may be due to a jet created by the grids in the vicinity of the wall. Indeed, the *Blockage ratio* exceeds the physical threshold of 0.4 suggested by Rose (1966) [61] in the first three layers of the grids. When the obstruction produced by the grids is too high, the flow can experience a transition from "wakes-interaction" to "jets-interaction" which could explain the observed results.

The second set of grids presented in subsection 4.4.1.2 was designed and tested during the second experimental campaign, in order to verify the actual influence of a high blockage near the wall on the flow.

5.1.4 Analysis of the boundary layer height

In the Figure 5.5, the estimated boundary layer height (δ_{99}) is emphasised along with a comparison of the mean velocity profiles generated by the grids in the two roughness configurations. The following considerations can be made from the results:

- It can be noticed that the roughness at the wall has a negligible influence on the boundary layer depth, indeed only the profile generated by grid 3 shows a slight decrease in δ_{99} when the LEGO® baseboard is added. This means that the wall has low influence on the artificial δ_{99} produced by the grids;
- The grid 1 produces a boundary layer which is smaller than expected. The reason could be that in the design the natural boundary layer created by the upper wall (located at $z = 290\ mm$) is not taken into account;
- In the partial grids δ seems to be related to the actual grids' height. Indeed, even if the objective's profiles have a different boundary layer depth, the measured δ_{99} is exactly the same in both the roughness configurations. In particular, it is slightly larger than the grid's height (116 mm for both grid 2 and 4).

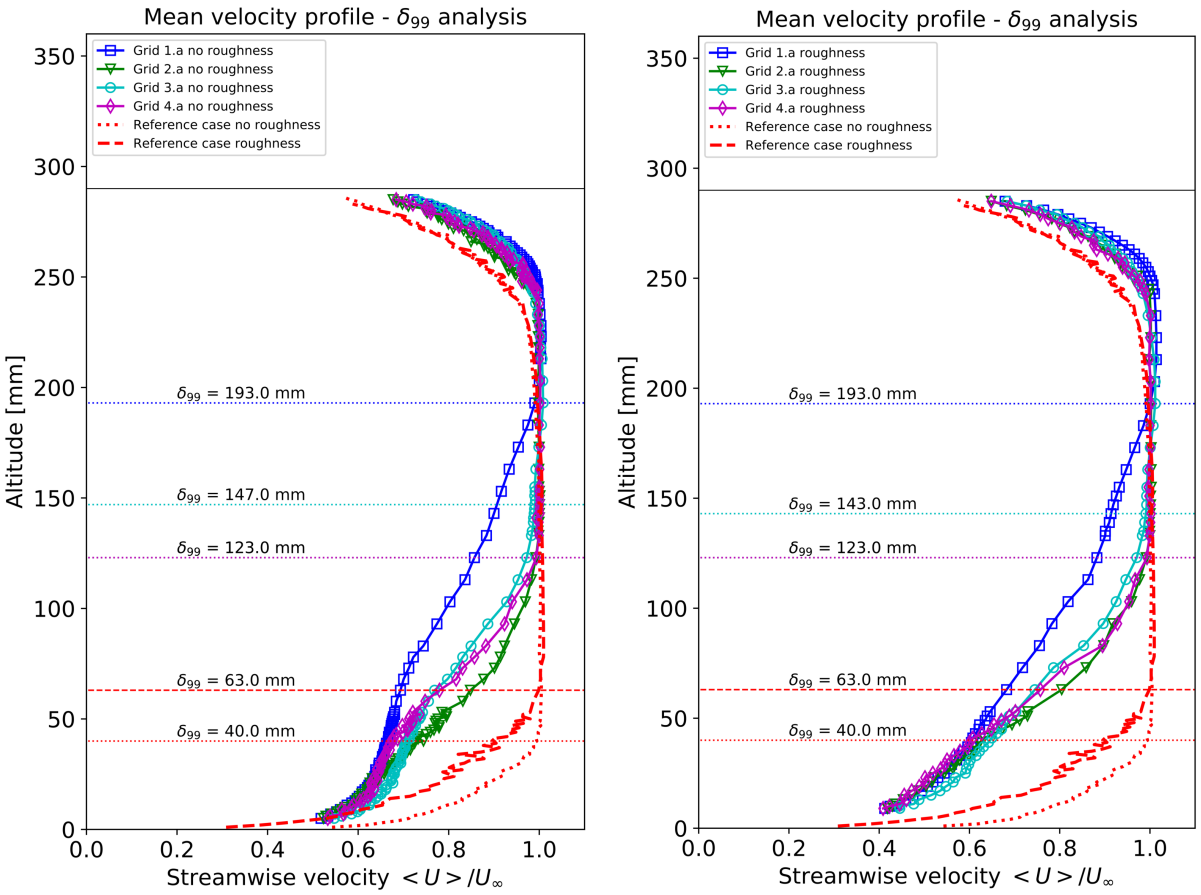

(a) Smooth configuration. **(b)** Roughness configuration.

Figure 5.5: Comparison of the measured boundary layer heights δ_{99} generated by the grids "a". The measurements were taken using the X-HWA.

5.1.5 Final considerations about the first campaign

The first experimental campaign results were not completely satisfactory. The observed mean velocity profiles had different properties from the objective profile but seemed to roughly follow the law of the wake. The Reynolds stresses showed a possible jet-like structure in the wall-region that might be explained with the high blockage ratio created by the grids in the same region.

The main goal of the second experimental campaign is to investigate whether the Reynolds stresses and the velocity profile are actually affected by the high obstruction in the wall-region.

Near the wall the results show a not perfect roughness compatibility between grid and rough surface. A new characterisation of the empty vein rough configuration will be carried out to establish if the actual h_0 at the wall is higher than expected. However, in the second campaign the roughness height in the objective profiles won't be changed in order to evaluate the effects of the geometric modifications.

The turbulence intensity recorded downstream of the grids was satisfactory and in line with predictions, indeed grids and roughness worked together to intensify the turbulence.

A minor objective of the second experimental campaign is to determine if the higher-than-expected turbulence in grid 1 was caused by incompletely achieved turbulence homogeneity.

Finally, the analysis of the velocity profiles showed that it is possible to control the boundary layer depth in the full-section grids while it appears to be more complicated in partial-section grids. It would be interesting to investigate whether the height of the generated boundary layer correlates with the grid's blockage ratio.

5.2 Second experimental campaign

The reasons that led to the new grid design have previously been discussed in section 4.4, which also provided a comparison of the main geometric properties of the nine manufactured devices in Table 4.2. Nevertheless, it is interesting to show graphically a comparison of the main design parameter for one of the four grids, in order to see how the geometric modifications listed in subsection 4.4.1.2 might affect *blockage ratio*, *resistance coefficient*, and *width of the vertical bars* .

The distribution of these characteristics throughout the various levels for "grid 3.a" is shown in Figure 5.6, along with the normalized objective velocity profile. In the graphs, horizontal dashed lines represent the grid's horizontal bars. The discrete properties are computed at the middle point of each grid's layer and are displayed as square markers.

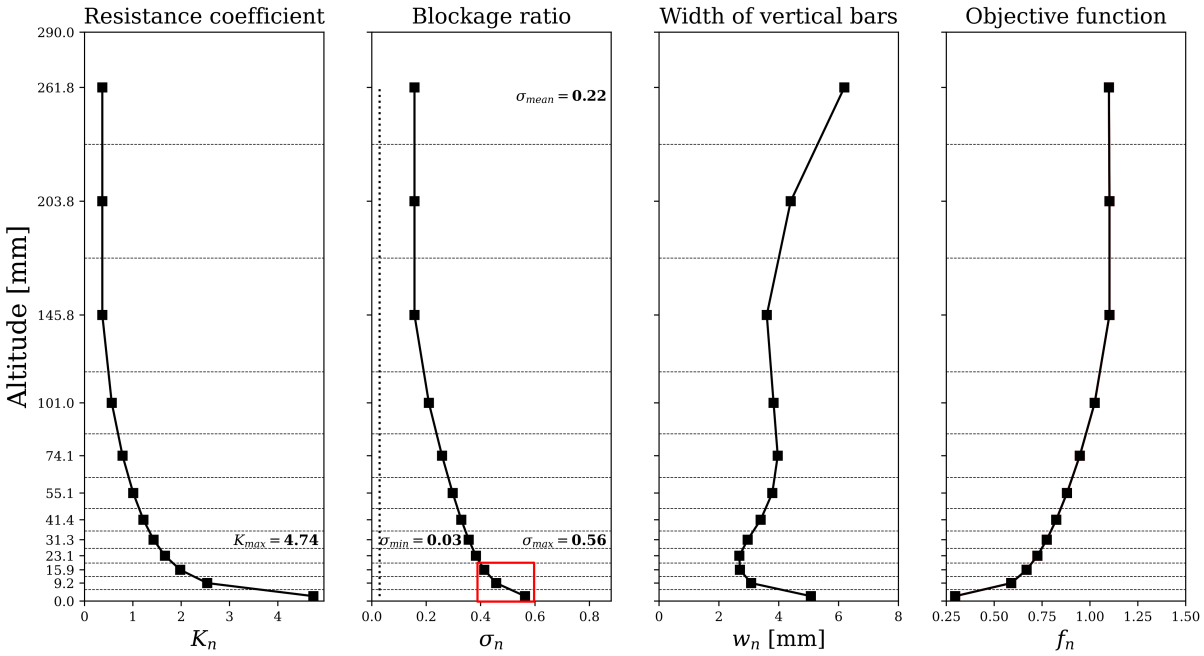

Figure 5.6: Distribution over the n layers of: K_n (resistance coefficient), σ (blockage ratio), w_n (width of the vertical bars) and f_n (objective function). The σ values larger than 0.4 are highlighted in red.

It is possible to see clearly that in the first three layers the grid produces a *blockage ratio* which exceeds the threshold given by Rose (1966) [61], i.e. $\sigma > 0.4$. Moreover,

these grid levels are very close to each other. Together, these features could explain the unexpected trend seen in the Reynolds Stresses (Figure 5.4).

These characteristics can be now compared with those obtained for "grid 3.b" which are shown in Figure 5.7. It is possible to notice that the grid's K_{max} and σ_{max} significantly decreased due to the geometric modifications and the same conclusion can be made for all the grids (as shown in Table 4.2). Another important difference concerns the trend of the vertical bars width. It is almost linear in "grid 3.b", with a minimum about in the middle of the section; but nonlinear in "grid 3.a" where the minimum is observed in the vicinity of the wall.

The vertical bars of the grids are dependant of σ which is derived directly from the optimization algorithm (see Figure 4.1) and their distribution over the grid's layers could have an influence on the flow properties. However, no connections between Reynolds Stresses and bars width were discovered in the literature, and additional research would be required to be certain that the two variables are unrelated.

Finally, the objective function f_n shows that "grid 3.a" has a greater resolution in the logarithmic layer due to the higher level number.

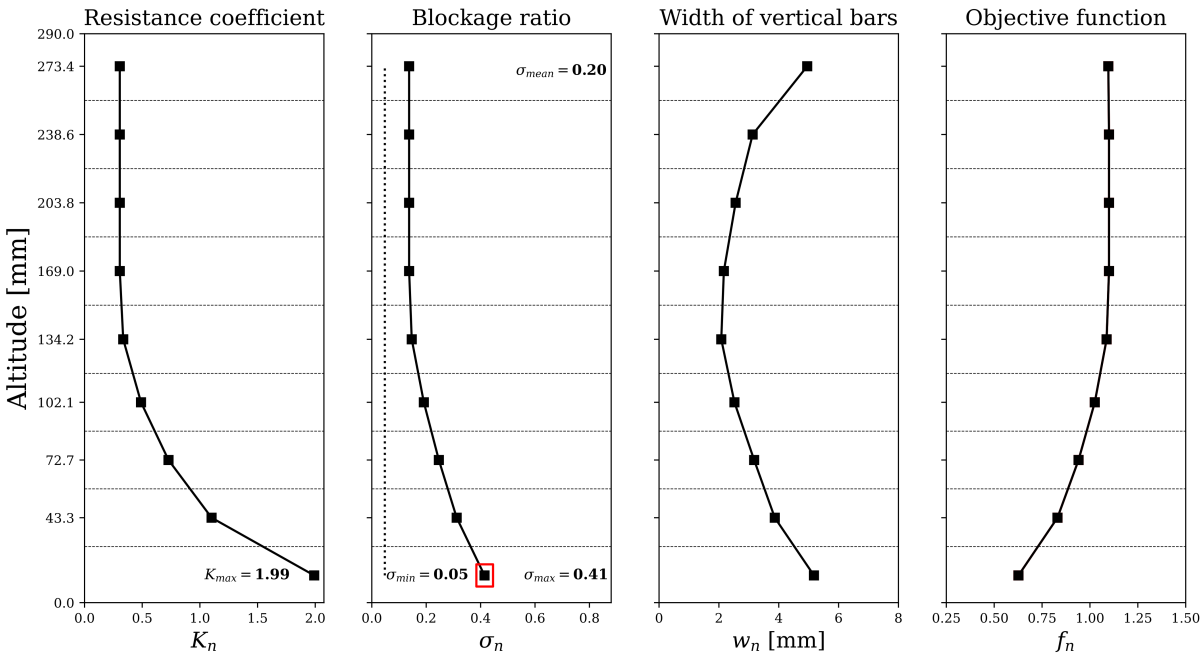

Figure 5.7: Distribution over the n layers of: K_n (resistance coefficient), σ (blockage ratio), w_n (width of the vertical bars) and f_n (objective function). The σ values larger than 0.4 are highlighted in red.

5.2.1 Estimation of roughness properties at the wall

The LEGO® surface's properties used as input in the grid design (u_* and h_0) were estimated from the empty vein characterization with roughness at the wall (as described in section

4.3.2). After this process, the LEGO® baseboard has been removed to carry out experiments in the smooth configuration of the wind tunnel.

During the removal procedure the LEGO® surface was slightly bent and damaged since the used glue was particularly strong. In the regions where it was bent, it displayed irregularities and had trouble adhering to the wall when it was reapplied to the flat plate, for the first and second experimental campaigns. Therefore, a new characterization of the empty wind tunnel with roughness is carried out to establish the consequences of the irregularities on the h_0 and u_* properties.

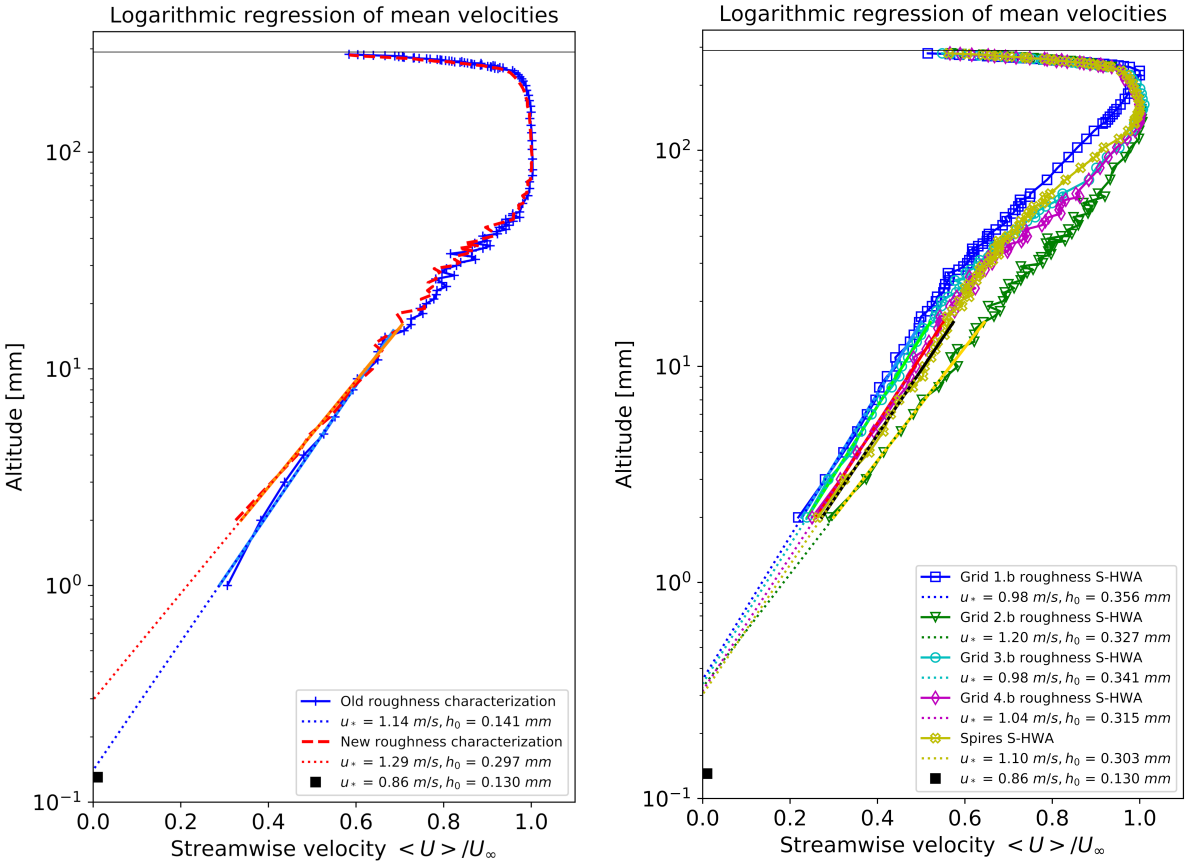

(a) Comparison between LEGO® baseboard's roughness characterizations before and after the first experimental campaign.

(b) Logarithmic fit of mean velocity profiles in the wall region produced by grids "b" and spires with LEGO® baseboard.

Figure 5.8: Logarithmic fit of mean velocities implemented for the estimation of friction velocity and roughness height at the wall. The measurements were taken using the S-HWA.

The velocity profiles in the wall-region are fitted using a logarithmic law to determine the roughness height and friction velocity. This represents a straightforward approach to estimate the surface features when the mean velocity profile deviates from the law of the wake. Such estimation by interpolation of mean profile is known to suffer from large uncertainties [10], in particular for roughness measurement (due to the exponential relation between roughness length and velocity and the difficulty to access the vicinity of the wall). Therefore, the S-HWA was used to measure the mean velocities since it can go up to 2 *mm* from the wall.

Figure 5.8a shows that this approach and the method explained in section 4.3 give comparable results in terms of h_0 and u_* (see Figure 4.8b).

The characterisation shows that the effective roughness height at the wall is about twice higher than previously estimated. This finding could explain the incompatibility between grid and LEGO® baseboard observed in the first experimental campaign. Indeed, by applying the same regression to the velocity profile produced by the new set of grids (and spires) in the rough configuration, similar h_0 values are obtained (see Figure 5.8).

Therefore, the profile obtained from this roughness characterisation will be used as "roughness reference case" in the second experimental campaign and compared with the flow generated by the second set of grids. Considering these findings, in the next section the measured velocity profiles will be compared to either the objective function used in the design code and the theoretical profile that we would obtain by plugging the measured value h_0 into the same design algorithm.

5.2.2 Mean velocity profile analysis

The turbulent flows generated by the new set of grids and spires are measured by the Single hot-wire probe at the location *"IIIT6-Center"* and at approximately the same distance from the grids. Figure 5.9 provides a comparison of the normalized mean velocity profiles measured in the smooth and rough wind tunnel configurations. By scaling the normal-wall coordinate with the estimate boundary layer thickness (δ_{99}) it is possible to compare the profiles obtained with the different devices. However, it is worth to mention that the δ_{99} estimation is affected by measurement uncertainties and it might be inaccurate. The potential errors in the δ_{99} may determine a shift of the normalized profile over the vertical axis which is not physical. Therefore, a comparison between rough and smooth not-normalized velocity profiles generated by each grid will be also provided.

5.2.2.1 Smooth configuration

The five velocity profiles seem to follow rather successfully the law of the wake when normalized, as shown in Figure 5.9a. In the outer region of the boundary layer, the five profiles essentially appear to match their objective. However in the wall-region, the lack of roughness similarity at the wall causes the flow acceleration. In fact, the smooth wall has a roughness height that is lower than the design one, and the profiles adjust to the smaller h_0 by reducing the friction velocity close to the wall. This leads to a different slope between the measured and the objective velocity profiles in the wall region. These findings justify the need for a roughness similarity of the wall surface with the required value of h_0, as expressed by the Jensen similarity criterion [50].

Moreover, it is possible to notice that the partial-section devices (grids 2.b, 4.b and spires) produce higher velocities than the full-section ones, in the region near the wall. This might imply that the free stream flow is having an impact on the artificial boundary layer

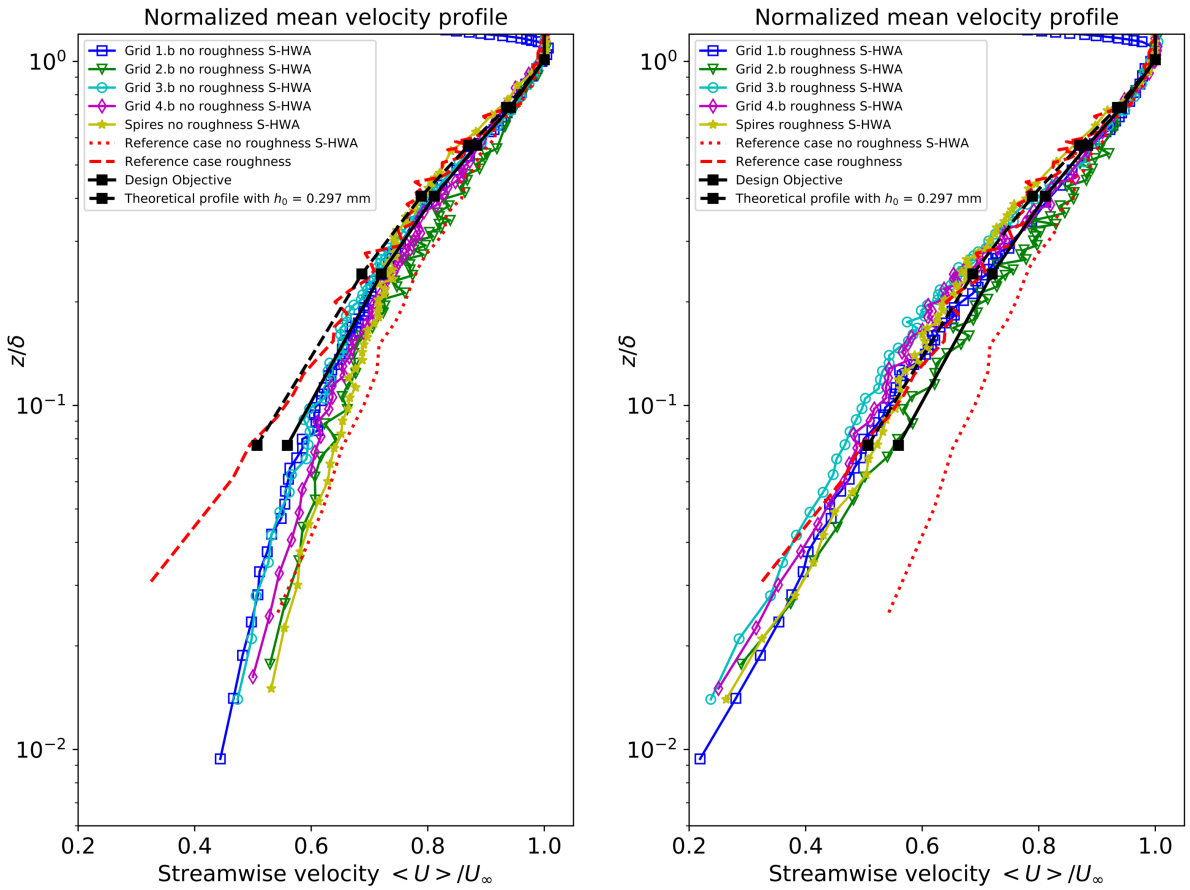

(a) Smooth configuration. **(b)** Roughness configuration.

Figure 5.9: Comparison of grids "b" and spires normalized mean velocity profiles in the boundary layer. The dashed black line indicates the theoretical profile that would be obtained if we used the input value $h_0 = 0.297\ mm$, whereas the solid black line represents the objective function. The measurements were taken using the S-HWA.

flow. Contrarily, the full section grids profiles follow rather accurately the target function up to the area very close to the wall. The five profiles will be examined independently and compared with their respective objective functions in order to more accurately assess how they behave in the near-wall region.

5.2.2.2 Rough configuration

Figure 5.9b shows that the normalized mean velocity profiles follow successfully the law of the wake also when the roughness is added to the wall. Although the match between obtained and objective profiles is not perfect throughout the full boundary layer, their trends appear to be the same. This is not the case with the mean velocities generated by grid 2.b, which are higher than expected in the boundary layer's outer area. The comparison of the not normalized profiles (presented in the next section) will clarify if this is the consequence of an inaccurate δ_{99} estimation.

It is interesting to notice that the flow generated by grids and spires is not longer dependent on the wall characteristics sufficiently far from the wall. Therefore, in the outer

region of the boundary layer all the velocity profiles (except for grid 2.b one) appear to follow the objective function and the theoretical profile obtained with the higher roughness height ($h_0 = 0.297\ mm$). The spires seem to follow the profile with $h_0 = 0.297\ mm$ over the whole boundary layer thickness. Instead, grids 1.b, 3.b and 4.b produce flows that are closer to the design objective in the outer region and then transition to higher h_0 and u_* in the wall-region. The bigger eddies created by the spires, which improve turbulence mixing and allow for a better transmission of information from the wall to the whole boundary layer, may be the reason of their different behavior.
Finally, all the trends in the vicinity of the wall seem to confirm that the roughness height utilized in the code ($h_0 = 0.13\ mm$) is less than the effective one.

5.2.2.3 Analysis of the not normalized mean velocity profiles

Figures 5.10 and 5.11 provide the not normalized velocity profiles of the four grids and spires in comparison with their objective profiles. The goal is to eliminate any ambiguities associated with the δ_{99} estimation and to visually see the achieved h_0 in the wall region. Overall, the five plots seem to confirm the previous observations. Two main regions can be observed: a wall-region of approximately the same height as the natural boundary layer growing in empty vein configuration, and an outer region. The mean velocity profiles show a logarithmic trend in both areas but with different slopes. Moreover, the comparison between smooth and rough configurations clearly show that the inner region is controlled by the wall roughness, while the outer one is determined by the characteristics of the grids (or spires).

The previously described transition to higher u_* and h_0 in the wall-region is confirmed, which is likely related to an underestimation of the actual surface roughness. Compared to partial section devices, the transition occurs farther from the wall in full section grids. The profile produced by grid 2.b stands out because it does not clearly show a shift of properties. The behaviour seen with partial-section grids might be explained by the interaction between free stream flow and artificial boundary layer.

Taking into account the roughness incompatibility between wall and LEGO® baseboard, the full-section grids seem to reproduce fairly well the desired velocity profile (see Figures 5.10a and 5.10c). The two partial-section grids have different behaviours. Figure 5.10b shows that grid 2.b is the only one that seems to follow the design objective function in the wall region. Despite this, it presents some uncertainties as we move far from the wall. The profile produced by grid 4.b (see Figure 5.10d) appears to adapt perfectly to the higher roughness height in the wall-region. However, although the trend is correct in the outer-region of the boundary layer, there is a mismatch with the objective profile. The shift between the two profiles is likely due to the different boundary layer thickness. Indeed, grid 4.b seems to produce a profile with a lower δ than expected, and this is likely due to the significant difference between the objective δ and the grid's height. A complete analysis of the reproduced boundary layer heights is presented in subsection 5.2.5.

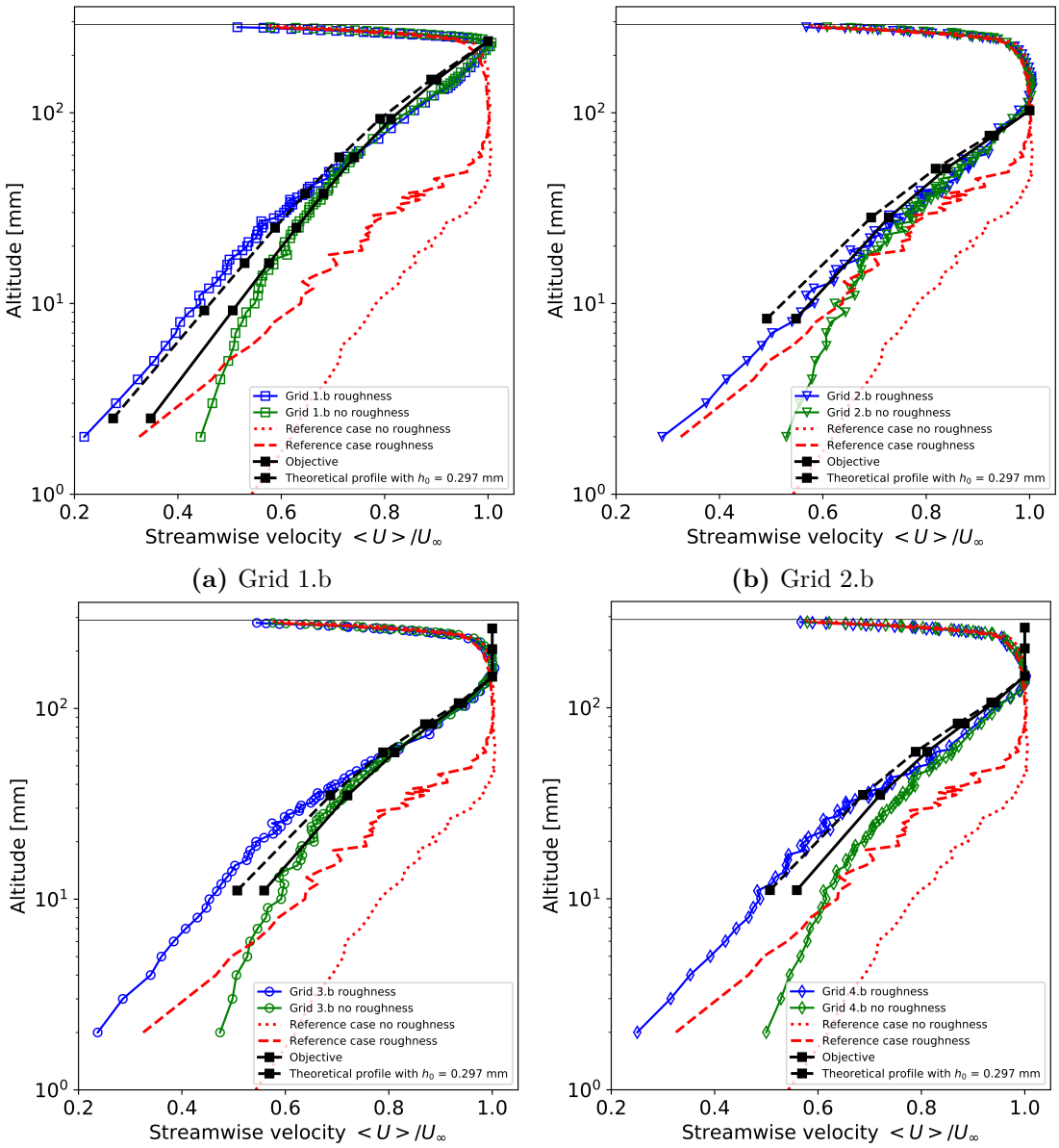

(a) Grid 1.b **(b)** Grid 2.b

(c) Grid 3.b **(d)** Grid 4.b

Figure 5.10: Comparison of the not normalized mean velocity profiles produced by grids "b". The dashed black line indicates the theoretical profile that would be obtained if we used the input value $h_0 = 0.297\ mm$, whereas the solid black line represents the objective function. The measurements were taken using the S-HWA.

To summarize, Figure 5.10 shows that the grids are really sensitive to the surface roughness in the wall region. In order to prevent incompatibilities near the wall and to obtain the desired velocity profile, a precise assessment of the roughness height of the wall surface is required. This might be considered a design difficulty that can be solved with specific measurement tools, and which is not seen in the spires-generated profiles. Indeed, Figure 5.11 shows that the not-normalized mean velocity profile (obtained in the rough configuration) seems to adapt perfectly to the actual h_0 of the wall. A nearly perfect agreement with the theoretical profile (obtained plugging $h_0 = 0.297\ mm$ into the design code) is observed, which also prove that the surface properties estimation shown

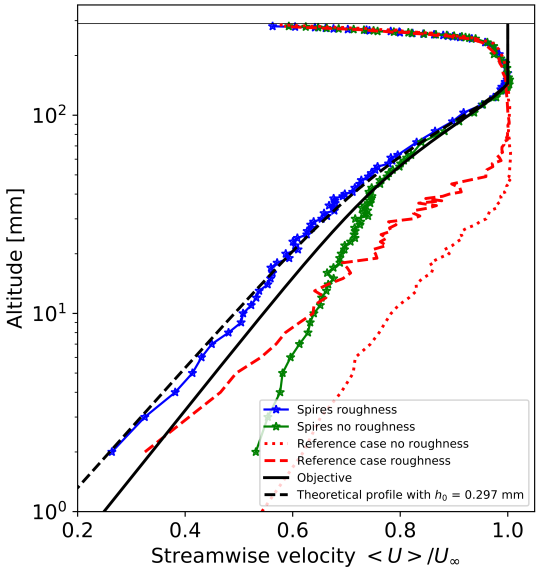

Figure 5.11: Not normalized mean velocity profile produced by the spires. The measurements were taken using the S-HWA.

in Figure 5.8b was rather accurate. As a conclusion, the spires design does not require a fully accurate estimation of the wall's roughness height to generate the correct prescribed velocity profile. Therefore, the spires ensure good results with less design complications compared to the grids.

5.2.3 Turbulence intensity analysis

Figure 5.12 shows the streamwise turbulence intensity obtained with the second set of grids and spires in the rough and smooth wind tunnel configurations. The overall profiles don't differ a lot from those generated by the first set of grids (Figure 5.3). Indeed, the turbulence profiles generated by grids 2, 3 and 4 in the two experimental campaign are very similar. Furthermore, the partial-section grids demonstrate that they are unable to influence the turbulence level in the free-stream region.

The region near the wall is mainly controlled by the surface roughness, therefore the Jensen similarity criterion [50] is necessary to reach the actual ABL turbulence intensity in the vicinity of the wall. In the rough wind tunnel configuration, at 2 *mm* it is possible to reach turbulence intensities up to about 35%. At the same location, this value decreases by more than half when the LEGO® baseboard is removed from the wall.

The turbulence intensity generated by grid 1.b seems to indicate that the flow has achieved turbulence homogeneity. In fact, the turbulence profile is smooth and nearly constant in the area far from the wall. The profile produced using grid 1.a, on the other hand, had bumps and oscillations that indicated non-homogeneity (see Figure 5.3). This result was obtained increasing the number of layers in the area of suspected non-homogeneity. This was done following the well-known dissipation law introduced by Taylor (1935) [89]:

$$\epsilon(t) = C_\epsilon \frac{u'(t)^3}{\mathcal{L}(t)} \tag{5.1}$$

where C_ϵ is a dimensionless time-independent constant, $\epsilon(t)$ the dissipation rate of turbulent kinetic energy, $u'(t)$ the velocity fluctuation and $\mathcal{L}(t)$ an integral length-scale. It is straightforward to observe that as the integral length scale decreases, the dissipation rate increases and it takes less time to reach the turbulence statistical steady state. Therefore, as the mesh size is reduced, the flow's integral length scales diminish and the flow reach the homogeneity at a smaller distance downstream of the grid.

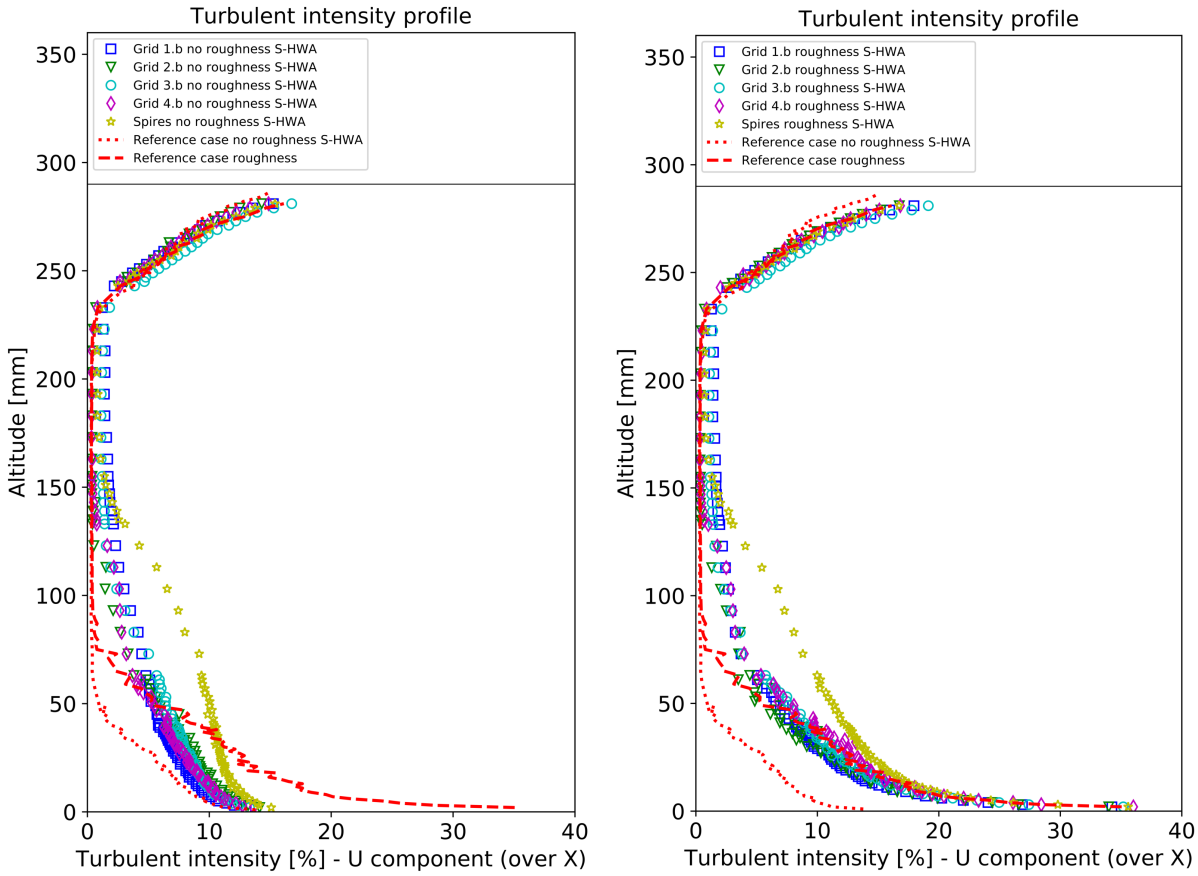

(a) Smooth configuration. **(b)** Roughness configuration.

Figure 5.12: Comparison of the grids "b" and spires turbulent intensity profiles. The measurements were taken using the S-HWA.

The drawback is that the smaller are the turbulent structures the faster they decay, reducing the flow's turbulence intensity [79]. As a result, grid 1.b produce a lower turbulence intensity than grid 1.a in the outer region of the boundary layer. For the same reason, the spires generate a visibly higher turbulence intensity over the whole boundary layer which is closer to the values actually measured in the real atmospheric boundary layer (larger than 10% according to Counihan, 1975 [88]). This is because the spires produce bigger eddy structures than the grids, as shown by the Integral length scale estimation (see Figures 5.15 and 5.16).

5.2.4 Reynolds stresses analysis

Figure 5.13 provides the Reynolds stresses generated by the second set of grids and by the spires with and without LEGO® baseboard at the wall. The odd behaviour observed in the first experimental campaign (see Figure 5.4) disappeared, suggesting that it was effectively caused by the high blockage and small layers height in the vicinity of the wall. The trend obtained with grid 1.b further confirms the achievement of the turbulence profile homogeneity.

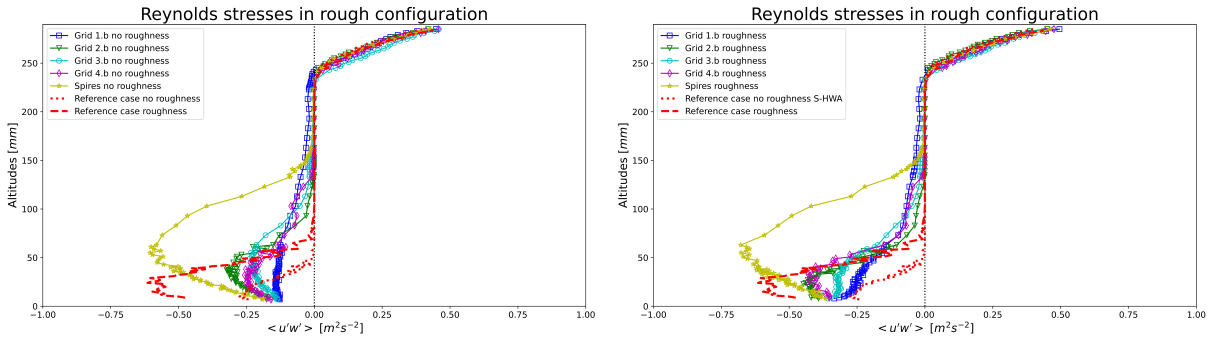

(a) Smooth configuration. **(b)** Roughness configuration.

Figure 5.13: Comparison of Reynolds stresses produced grids "b" and spires, with and without LEGO® baseboard on the wall. The measurements were taken using the X-HWA.

The five profiles exhibit the same behaviour, albeit with various orders of magnitude, as shown in Figure 5.13a. In particular, the Reynolds stresses' absolute value increases with the altitude in the wall region, it reaches a maximum and then it starts decreasing. Finally, it assumes null values in the free stream region, where $w' \approx 0$. In the rough configuration of the wind tunnel (Figure 5.13b), the partial-section devices seem to produce the same Reynolds stresses' trend and a maximum is visible at a certain distance from the wall. Contrarily, for the full-section grids 3.b and 1.b the maximum is registered near the wall. The first level of these two grids have a blockage ratio slightly higher than 0.4 which might interact with the LEGO® baseboard and produce the observed behaviour. On the other hand, the partial-section grids 2.b and 4.b produce $\sigma_n < 0.4$ everywhere.

As expected for boundary layers, the Reynolds stresses measured in the two experimental campaigns are negative, which means that the momentum flux is directed towards the wall. Indeed, by definition the Reynolds stress tensor is responsible for the transport of mean momentum due to turbulence. When the Reynolds stresses are acting diffusively on the mean flow, the mean momentum flux is always oriented in the opposite direction of the velocity gradient, since diffusion is always acting to "smear out" gradients. Because in a boundary layer $\partial U/\partial z > 0$, the Reynolds stresses have to be negative.

Moreover, it is possible to notice that the five profiles approach the same value in the vicinity of the wall, which is slightly lower than the respective reference case. As expected, in the wall-region the Reynolds stresses are higher when the LEGO® baseboard is added to the wall (since $u_* \approx \sqrt{u'w'}$). In general, grids and spires present a totally different

influence on the flow. The grids appear to reduce the Reynolds stresses of the naturally growing boundary layers. Contrarily, although the spires generate lower values near the wall, they significantly increase the Reynolds stresses absolute values over the boundary layer.

5.2.5 Analysis of the boundary layer height

The mean velocity profiles replicated in the wind tunnel together with the boundary layer height calculated using a 99 percent approximation are displayed in Figure 5.14. The estimation of the boundary layer thickness confirmed some observations made in the first experimental campaign. In particular, the different roughness at the wall does not have a relevant impact on the δ generated by the devices in the wind tunnel. The small differences seen between the rough and smooth configurations are due to small measurement uncertainties which can affect the δ_{99} estimation.

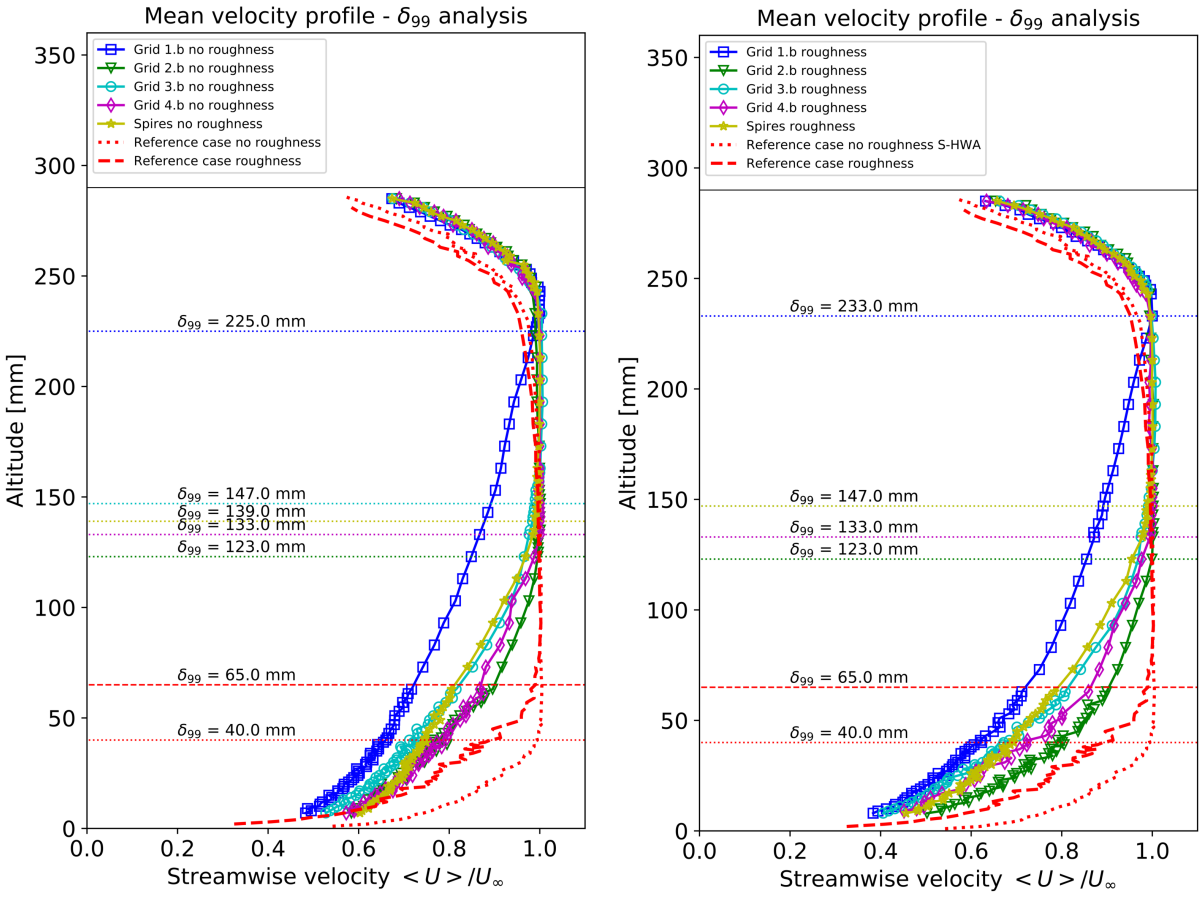

(a) Smooth configuration. **(b)** Roughness configuration.

Figure 5.14: Comparison of the measured boundary layer heights δ_{99} generated by grids "b" and spires. The measurements were taken using the X-HWA.

Moreover, the depth of the boundary layer produced by the partial section devices (grids 2, 4 and the spires) appear to be related to the effective device height. This feature has to be taken into account in the design process to obtain the required velocity profile.

It can be also noticed that the boundary layer size is not affected by the blockage ratio of the different grids' levels.

A relevant difference between the two campaigns concern the boundary layer produced by grid 1. In fact, there is a 20% difference in the boundary layer heights produced by grid 1.b and grid 1.a. Figure 5.14 shows that the obtained δ is still smaller than expected (290 mm) due to the influence of the upper boundary layer of the wind tunnel. However, the achievement of the turbulence homogeneity enables to get closer to the prescribed value of boundary layer thickness.

It is now possible to summarize the results of the second experimental campaign in the rough configuration in Table 5.1.

Table 5.1: Results of the second experimental campaign in the rough configuration.

Device	$u_*[m/s]$	$h_0[mm]$	$Height[mm]$	$\delta[mm]$	Re_θ	Re_{δ^*}	H
Grid 1.b	0.98	0.36	290	233	37816	54968	1.45
Grid 2.b	1.20	0.33	116	123	14556	19608	1.23
Grid 3.b	0.98	0.34	290	147	20723	31029	1.50
Grid 4.b	1.04	0.32	116	133	18571	26292	1.42
Spires	1.10	0.30	145	147	22984	32687	1.42

When compared to partial-section devices, the full-section grids appear to give larger roughness height close to the wall. Since the boundary layer thickness estimation can have uncertainties, a comparison of the Momentum and Displacement Reynolds numbers is provided. These two non-dimensional numbers are computed numerically as explained in section 4.3. When they have the same order of magnitude the boundary layer height is approximately the same. The comparison is consistent with the δ_{99} estimate. The highest boundary layer is obtained with grid 1.b, as expected. Grids 3.b and spires provide approximately the same boundary layer properties which are close to the prescribed ones. It is interesting to see that grid 4.b can generate a boundary layer higher than grid 2.b, but still smaller than the objective. Finally, the estimated shape factors, which are in the $1.2 - 1.5$ range, confirmed that the tested devices produced turbulent boundary layers.

Figure 5.14 showed that the boundary layer thickness is not really affected by the LEGO® baseboard at the wall. Therefore, the comparison of the results in the smooth wind tunnel configuration is not provided.

5.2.6 Integral length scales

Figures 5.15 and 5.16 display the integral length scales and the Taylor microscales obtained with the second set of grids and spires. The integral length scales are estimated using two of the methods presented in Appendix A: "Turbulence kinetic energy spectrum interpolation" and "Zero crossing of the longitudinal velocity fluctuation". The latter method is also used to compute the Taylor microscale. The "Integration of the correlation function" method is

not used because it introduces complications when the correlation function does not cross the horizontal axis (see Appendix B).

Although the two methods use completely different methodologies, they provide comparable integral length scale values. Moreover, they give better results for the full-section grids. In fact, the integral length scales obtained with grids 1.b and 3.b (Figures 5.15a and 5.15c) are proportional to the mesh size, as expected. On the other hand, the flow produced by partial-section devices show a different behaviour in the free stream region.

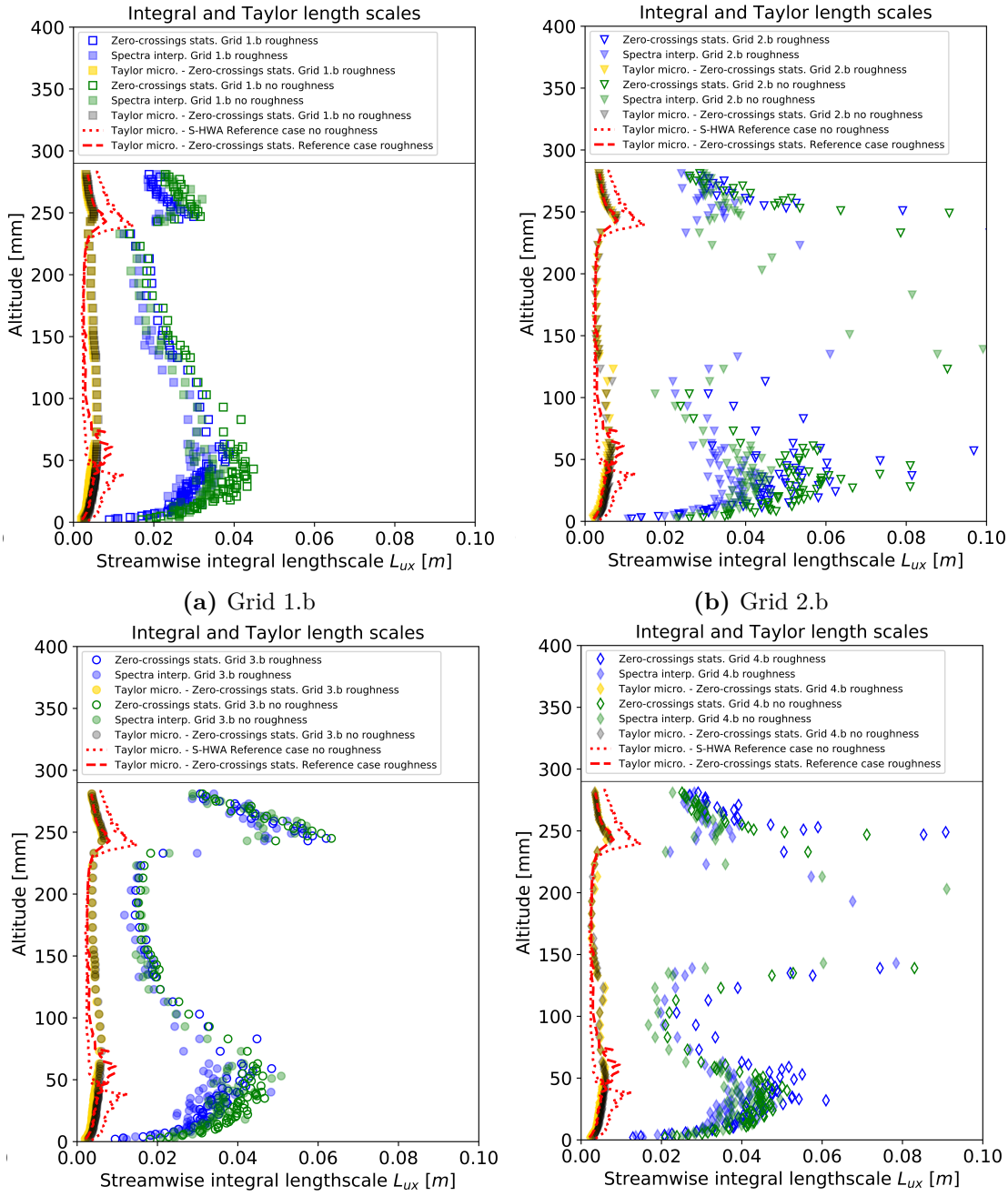

(a) Grid 1.b

(b) Grid 2.b

(c) Grid 3.b

(d) Grid 4.b

Figure 5.15: Comparison of the integral and Taylor length scales produced by grids "b". The measurements were taken using the S-HWA.

Here, the measured integral length scales reach very high values which are not physical. This happens because in this region the shear and the turbulence intensity are very low because we are far from the wall. As a result, the vortex structures are stretched and become very large, making it difficult to measure the integral length scales. A similar trend was revealed by the empty vein charaterisation, presented in Figure 4.7.

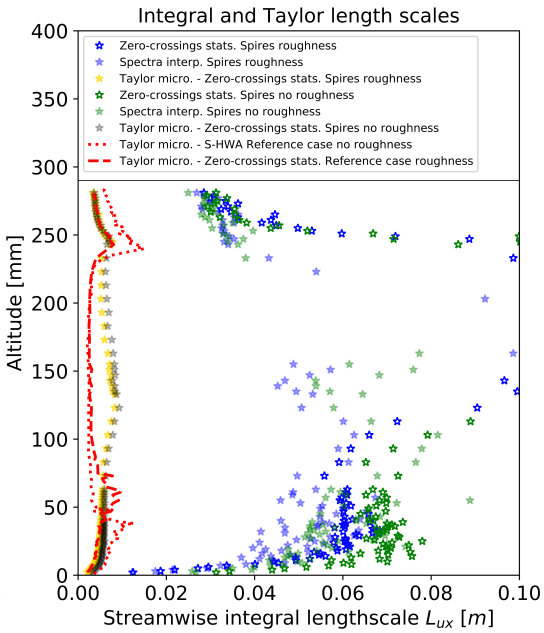

Figure 5.16: Integral and Taylor length scales produced by the spires. The measurements were taken using the S-HWA.

In the wall-region the four grids provide comparable integral length scale values, which are smaller than those produced by the spires. This was expected since the latter generates larger eddy structures. For all the devices, the trend is roughly linear with the height from the wall. Additionally, it appears that the impact of wall roughness is only significant in the area near the wall. In particular, the presence of the LEGO® baseboard seems to slightly reduce the integral length scales in the wall-region in full-section grids and spires (see Figures 5.15a, 5.15c and 5.16). However, the influence of the roughness is not completely understood for partial-section grids (Figures 5.15b and 5.15d).

Finally, the wall roughness also has an impact on the Taylor microscale. The latter seems to get smaller as the wall roughness increases, in the five devices. This effect is only evident in the wall-region.

Chapter 6

Conclusions and Future work

The purpose of the thesis project was to experimentally investigate the possibility of reproducing a full-depth atmospheric boundary layer in wind tunnel, by using MIG grids and spires. In the current project, the research focused on the neutral Atmospheric Boundary Layer (ABL) approximated using the "law of the wake". For this purpose, an existing design code was adapted to obtain both partial-section and full-section devices. Overall, nine passive devices were designed, manufactured and tested in the SCL-PIV wind tunnel at Onera Lille.

Two experimental campaigns were conducted, allowing for the evaluation of each device's advantages and disadvantages. The four grids tested in the first experimental campaign didn't give the expected results, but they enable to improve the design algorithm. This led to production of the five devices employed in the second experimental campaign. This second set of grids and spires showed that a mean velocity profile representative of an ABL could be replicated in a wind tunnel.

The second experimental campaign's results allowed to compare full-section and partial-section grids as well as grids and spires. The information obtained can be used to establish which is the best device to use for future applications. More specifically, two of the tested devices will be employed to reproduce an ABL for an industrial project in the L2 wind tunnel at Onera Lille.

6.1 Summary of the research results

Interesting conclusions are drawn from the experimental investigation that may be useful for future applications.

The Multiscale Inhomogeneous Grids (MIG), based on the McCarthy (1964) [21] model, represent a powerful tool to simulate a full-depth rough boundary layer. It can be useful for different applications either in the research or industrial fields.

The grids and the spires provided satisfactory results in terms of mean velocity profile when the wall roughness height was correctly approximated (not an easy task without specific measurement devices). However for all the grids, the turbulence intensity measured

in the outer layer was insufficient for simulating the ABL. Indeed, the turbulence profile was representative of the real phenomenon only in the region close to the wall due to the influence of the rough surface. This is not valid for the spires, since the bigger eddy structures created by their shape take more time to decay and keep the turbulence intensity sufficiently high over the whole boundary layer height.

The experimental investigation proved that it is possible to simulate the boundary layer and the undisturbed free-stream successfully with three different devices: full-section grids, partial-section grids and spires. The spires were already used for this purpose by Irwin (1981) [18] but only to generate a power-law profile, while in the current project a more general method to simulate different mean velocity profiles was successfully implemented. Moreover, the project showed the potential of partial-section grids which enables one to generate a prescribed boundary layer and to adjust it to fit the free stream flow above.

Despite providing good results for the mean velocity profile, full-section grids present drawbacks related to higher production costs, weight, and wind tunnel obstruction. These issues become crucial when the grids are designed and employed in large wind tunnel for industrial applications. Therefore, when full-section and partial-section grids give comparable results, the latter are preferred. However, the produced artificial boundary layer is about the same height as the partial-section device. So, the full-section devices are required to reproduce a boundary layer over the whole test section of the wind tunnel.

If the goal is to reproduce an artificial boundary layer with the free stream above, the ideal approach is to use partial-section grids or spires. The results of the second experimental campaign demonstrated that the spires are the preferable alternative. Indeed, they provide the desired mean velocity profile while requiring less efforts in the estimation of the roughness properties of the wall. Additionally, the spires provide stronger turbulence intensities than the grids and are more in line with measurements made in the actual atmosphere. As a consequence, they can generate a flow that is closer to the real ABL.

6.2 Proposals for future works

The internship work proved that the Multiscale Inhomogeneous Grids (MIG) can be used to produce a turbulent boundary layer with prescribed characteristics in the wind tunnel. The project focused specifically on the reproduction of a given mean velocity flow simulation. However, the investigation conducted by Zheng (2018) *et al.* [11] shows the MIG grids capability of controlling also the turbulence intensity profile. This is possible by applying a theoretical model which describes the turbulence evolution downstream of the grids.

An interesting continuation of the project might be the implementation of the theoretical method to the grids design algorithm in order to generate a specified turbulence intensity profile. This might allow to reproduce a realistic ABL with the actual turbulence level over the entire boundary layer in the wind tunnel. The tailoring of mean velocity and

turbulence independently would lead to the generation of more realistic flow's properties. Moreover, the time required for the device's design would be drastically reduced by this method, since it doesn't involve trials and errors techniques.

However, the method presented by Zheng (2018) *et al.* [11] is specific for grids. A future challenge might be the adaptation of the turbulence model to the spires design. This would allow to obtain the desired mean velocity and turbulence intensity profiles and to increase the turbulence levels.

6.3 Adaptation of grids and spires to a larger wind tunnel

The design code presented in subsection 4.1.2 is very general and adaptable to any wind tunnel section. This section will show the design of grid 2.b and spires for the L2 wind tunnel of ONERA Lille.
The ONERA L2 facility is an open-circuit wind tunnel offering a large test section: $6\ m \times 2.4\ m \times 13\ m$. Velocity is continuously adjustable up to $19\ m/s$. In September 2022, these two devices will be manufactured using wooden panels and used for reproducing the ABL in L2 for industrial applications.

In the experiment, the wall standing for the Earth surface will be the lateral wall of the wind tunnel. Therefore, the devices' width will be $2.4\ m$ and their height will be approximately equal to the prescribed boundary layer depth in L2, which can be $\delta^{L2} \approx 1\ m$ or $\delta^{L2} \approx 2\ m$. Indeed, each device will be designed twice in order to reproduce boundary layers with identical characteristics but different heights. Figure 6.1 shows the CAD of the L2 wind tunnel:

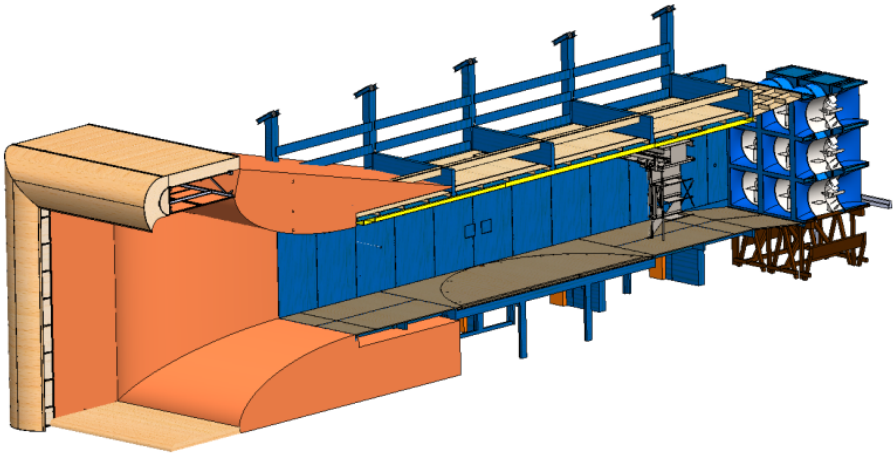

Figure 6.1: CAD of the L2 wind tunnel at Onera Lille.

Because of the different dimensions of the generated boundary layers, some of the design parameters used to build the devices for SCL-PIV wind tunnel have to be scaled.

First of all, the Jensen similarity criterion [50] (described in subsection 2.5.1) has to be respected. It is important to remember that the grid 2.b and spires heights were different (see Table 4.2), therefore a different scale and a different roughness height should be used to obtain the same characteristics in L2. However, as the objective is to achieve equivalent ABL with the two devices, the same roughness height will be adopted for both. In order to obtain larger turbulence intensities near the wall, the highest h_0 is chosen .

A scaling factor is necessary to relate the roughness properties of the wall in the two wind tunnels. This can be taken as the ratio between the heights of the devices tested in SCL-PIV wind tunnel and the desired heights of the new devices for L2. The highest scale will be used for both the devices in order to achieve larger h_0 and turbulence intensities. Therefore, the scale will be computed considering the height of grid 2.b, leading to: $H^{L2}/H^{SCL} = 1/0.116 = 8.6$ for $\delta^{L2} \approx 1\ m$ and $H^{L2}/H^{SCL} = 17.2$ for $\delta^{L2} \approx 2\ m$. Multiplying these scaling factors by the roughness height of the LEGO baseboard that is required in the L2 wind tunnel to respect the Jensen similarity, we get: $h_0^{L2}|_{\delta^{L2}=1\ m} = 1.12\ mm$ and $h_0^{L2}|_{\delta^{L2}=2\ m} = 2.24\ mm$. Considering the average ABL thickness $\delta^{ABL} \approx 600\ m$ suggested by Counihan (1975) [88], the scale between L2 and real atmosphere can be derived as $S = \delta^{ABL}/\delta^{L2}$.

In order to get the actual roughness height h_0^{ABL} that can be replicated in the wind tunnel, the S values calculated for the two desired δ^{L2} have to be multiplied by the corresponding h_0^{L2}. As a result, the same value $h_0^{ABL} \approx 0.674\ m$ is obtained for the two boundary layer depths. This corresponds to the *"Very rough"* condition according to the Davenport's classification [29], shown in Figure 2.5b.

The large test section of the L2 wind tunnel requires a different approach to reproduce the Earth roughness. One of the best alternatives is the McDonald method (1998) [90], because it was already successfully implemented in L2 for a past project. The desired h_0 is reproduced by using an array of regular cubes. The size of the cubes and their spacing are adjusted using empirical relations, in order to reproduce a specific roughness height. This approach is not limited to cubes but it can be extended to other objects like chains or cylinders, as shown by Cal *et al.* (2010) [91]. Most likely, cubes or cylinders will be used in our project.

Finally, the size of the horizontal bars has to be adjusted to keep the same proportions with the rest of the structure. Therefore, the horizontal bars width (T_b) and depth (d_b) are multiplied by the ratio H^{L2}/H^{SCL}. This is valid only for the grid, because the spires don't have horizontal bars.

Figure 6.2 show the two versions of grid 2.b for the generation of the ABL in L2 wind tunnel. The two grids have similar structures but they produce boundary layers of different sizes.

Figure 6.3 shows the two arrays of spires that will be employed in the L2 wind tunnel for the generation of boundary layers with $\delta^{L2} = 1\ m$ and $\delta^{L2} = 2\ m$. Following Irwin (1981) [18] design recommendations, a different number of spires is selected for each array,

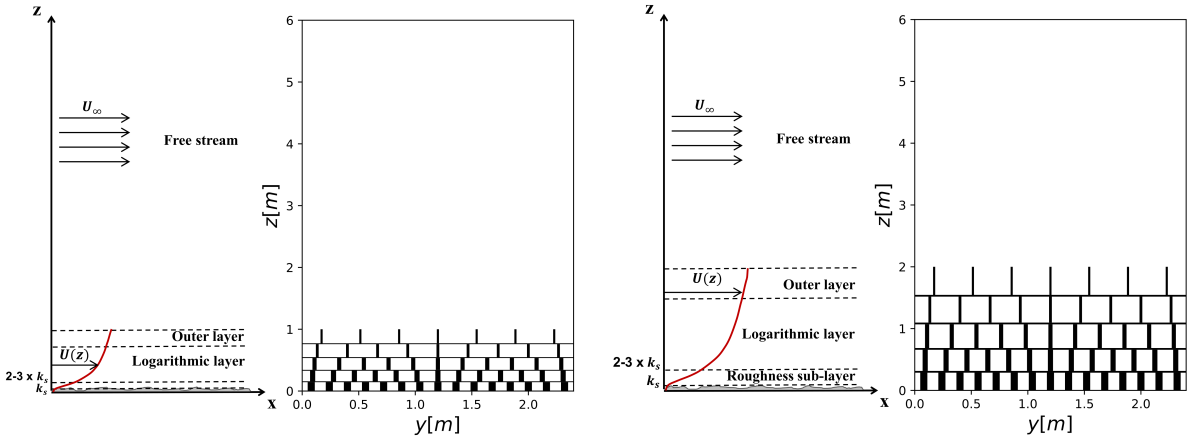

(a) Grid 2.b for the generation of a boundary layer thickness $\delta^{L2} = 1\ m$.

(b) Grid 2.b for the generation of a boundary layer thickness $\delta^{L2} = 2\ m$.

Figure 6.2: Schemes of the two grids 2.b for the L2 wind tunnel and turbulent velocity profiles over a rough surface. The boundary layer sketch is inspired from Kadivar (2021) [12]

since the spires in the two configurations have different heights. In each configuration, the spires' heights have to be the same and the spacing between them needs to be constant. Moreover, two adjacent spires should be spaced so that the distance between their tips is roughly half their height.

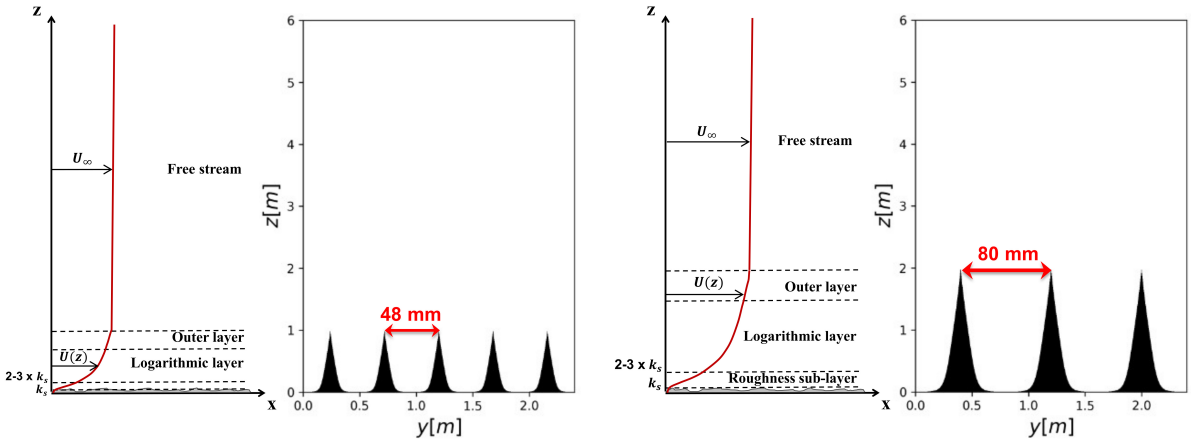

(a) Array of 5 spires for the generation of a boundary layer thickness $\delta^{L2} = 1\ m$.

(b) Array of 3 spires for the generation of a boundary layer thickness $\delta^{L2} = 2\ m$.

Figure 6.3: Schemes of the two spires arrays for the L2 wind tunnel and turbulent velocity profiles over a rough surface. The boundary layer sketch is inspired from Kadivar (2021) [12].

Bibliography

[1] "Establishment of an atmospheric flow laboratory," *https://bmeafl.com/the-project-proposal/*.

[2] Holton, *An Introduction to Dynamic Meteorology*, vol. 88. 5th ed., 2012.

[3] R. K. Smith, "LECTURES ON DYNAMICAL METEOROLOGY," p. 214, 2001.

[4] A. S. Monin and A. M. Obukhov, "Basic laws of turbulent mixing in the surface layer of the atmosphere," *Tr. Akad. Nauk. SSSR Geophiz. Inst.*, vol. 24, no. 151, pp. 163–187, 1954.

[5] J. C. Kaimal and J. J. Finnigan, *Atmospheric Boundary Layer Flows: Their Structure and Measurement*. Oxford, New York: Oxford University Press, Mar. 1994.

[6] I. N. Smalikho and V. A. Banakh, "Measurements of wind turbulence parameters by a conically scanning coherent Doppler lidar in the atmospheric boundary layer," *Atmospheric Measurement Techniques*, vol. 10, pp. 4191–4208, Nov. 2017. Publisher: Copernicus GmbH.

[7] ESDU 85020, "Characteristics of atmospheric turbulence near the ground - Part II: singlepoint data for strong winds (neutral atmosphere)," 1985.

[8] V. A. Banakh and I. N. Smalikho, "Lidar Studies of Wind Turbulence in the Stable Atmospheric Boundary Layer," *Remote Sensing*, vol. 10, p. 1219, Aug. 2018. Number: 8 Publisher: Multidisciplinary Digital Publishing Institute.

[9] S. J. Caughey, J. C. Wyngaard, and J. C. Kaimal, "Turbulence in the Evolving Stable Boundary Layer," *Journal of Atmospheric Sciences*, vol. 36, pp. 1041–1052, June 1979. Publisher: American Meteorological Society Section: Journal of Atmospheric Sciences.

[10] N. J. Cook, "Wind-tunnel simulation of the adiabatic atmospheric boundary layer by roughness, barrier and mixing-device methods," *Journal of Wind Engineering and Industrial Aerodynamics*, vol. 3, pp. 157–176, Jan. 1978.

[11] S. Zheng, P. J. K. Bruce, J. M. R. Graham, and J. C. Vassilicos, "Weakly sheared turbulent flows generated by multiscale inhomogeneous grids," *Journal of Fluid Mechanics*, vol. 848, pp. 788–820, Aug. 2018.

[12] M. Kadivar, D. Tormey, and G. McGranaghan, "A review on turbulent flow over rough surfaces: Fundamentals and theories," *International Journal of Thermofluids*, vol. 10, p. 100077, May 2021.

[13] T. von Kármán, "Progress in the statistical theory of turbulence*," *Proceedings of the National Academy of Sciences*, vol. 34, no. 11, pp. 530–539, 1948.

[14] R. B. Stull, *An Introduction to Boundary Layer Meteorology*. Atmospheric and Oceanographic Sciences Library, Springer Netherlands, 1988.

[15] S. E. Hommema and R. J. Adrian, "Packet Structure of Surface Eddies in the Atmospheric Boundary Layer," *Boundary-Layer Meteorology*, vol. 106, pp. 147–170, Jan. 2003.

[16] J. Counihan, "An improved method of simulating an atmospheric boundary layer in a wind tunnel," *Atmospheric Environment (1967)*, vol. 3, no. 2, pp. 197–200, 1969.

[17] R. J. Hearst and B. Ganapathisubramani, "Tailoring incoming shear and turbulence profiles for lab-scale wind turbines," *Wind Energy*, vol. 20, pp. 2021–2035, Dec. 2017.

[18] H. P. A. H. Irwin, "The design of spires for wind simulation," *Journal of Wind Engineering and Industrial Aerodynamics*, vol. 7, pp. 361–366, May 1981.

[19] H. Kozmar, "Characteristics of natural wind simulations in the TUM boundary layer wind tunnel," *Theor Appl Climatol*, vol. 106, pp. 95–104, Nov. 2011.

[20] J. E. Cermak, "Laboratory Simulation of the Atmospheric Boundary Layer," *AIAA Journal*, vol. 9, pp. 1746–1754, Sept. 1971.

[21] J. H. McCarthy, "Steady flow past non-uniform wire grids," *Journal of Fluid Mechanics*, vol. 19, pp. 491–512, Aug. 1964. Publisher: Cambridge University Press.

[22] T. Reichler, M. Dameris, and R. Sausen, "Determining the tropopause height from gridded data," *Geophysical Research Letters*, vol. 30, no. 20, 2003. _eprint: https://onlinelibrary.wiley.com/doi/pdf/10.1029/2003GL018240.

[23] J. R. Garratt, "Review: the atmospheric boundary layer," *Earth-Science Reviews*, vol. 37, pp. 89–134, Oct. 1994.

[24] L. Mahrt, "Stratified Atmospheric Boundary Layers," *Boundary-Layer Meteorology*, vol. 90, pp. 375–396, Mar. 1999.

[25] L. F. Richardson and W. N. Shaw, "The supply of energy from and to atmospheric eddies," *Proceedings of the Royal Society of London. Series A, Containing Papers of a Mathematical and Physical Character*, vol. 97, pp. 354–373, July 1920. Publisher: Royal Society.

[26] J. Jiménez, "Turbulent Flows Over Rough Walls," *Annual Review of Fluid Mechanics*, vol. 36, no. 1, pp. 173–196, 2004. _eprint: https://doi.org/10.1146/annurev.fluid.36.050802.122103.

[27] A. G. Davenport, *Wind loads on structures*. No. 83 in Division of Building Research Technical Paper, division of building research ed., 1960.

[28] C. S. B. Grimmond and T. R. Oke, "Aerodynamic Properties of Urban Areas Derived from Analysis of Surface Form," *J. Appl. Meteor.*, vol. 38, pp. 1262–1292, Sept. 1999. Publisher: American Meteorological Society.

[29] A. Davenport, C. Grimmond, T. Oke, and J. Wieringa, "Estimating the roughness of cities and sheltered country," *15th conference on probability and statistics in the atmospheric sciences/12th conference on applied climatology, Ashville, NC, American Meteorological Society*, pp. 96–99, Jan. 2000.

[30] D. Laporte, *A surface roughness parameterization study near two proposed windfarm locations in Southern Ontario*. PhD thesis, Aug. 2010.

[31] R. B. Stull, "9 - The Atmospheric Boundary Layer," in *Atmospheric Science (Second Edition)* (J. M. Wallace and P. V. Hobbs, eds.), pp. 375–417, San Diego: Academic Press, Jan. 2006.

[32] D. Coles, "The law of the wake in the turbulent boundary layer," *Journal of Fluid Mechanics*, vol. 1, pp. 191–226, July 1956. Publisher: Cambridge University Press.

[33] J. Hinze, *Turbulence: An Introduction to Its Mechanism and Theory par J.O. Hinze, Professor of Fluid Mechanics, Technological University, Delft: Good Hardcover | ThriftBooks-Atlanta*. New York: McGraw-Hill Publishing Co., second ed., 1975.

[34] I. Marusic, K. A. Chauhan, V. Kulandaivelu, and N. Hutchins, "Evolution of zero-pressure-gradient boundary layers from different tripping conditions," *Journal of Fluid Mechanics*, vol. 783, pp. 379–411, Nov. 2015. Publisher: Cambridge University Press.

[35] J. Andersson, D. R. Oliveira, I. Yeginbayeva, M. Leer-Andersen, and R. E. Bensow, "Review and comparison of methods to model ship hull roughness," *Applied Ocean Research*, vol. 99, p. 102119, June 2020.

[36] Y. K. Demirel, O. Turan, and A. Incecik, "Predicting the effect of biofouling on ship resistance using CFD," *Applied Ocean Research*, vol. 62, pp. 100–118, Jan. 2017.

[37] M. P. Schultz and K. A. Flack, "The rough-wall turbulent boundary layer from the hydraulically smooth to the fully rough regime," *Journal of Fluid Mechanics*, vol. 580, pp. 381–405, June 2007. Publisher: Cambridge University Press.

[38] J. Vilà-Guerau de Arellano, C. C. van Heerwaarden, B. J. H. van Stratum, and K. van den Dries, *Atmospheric Boundary Layer: Integrating Air Chemistry and Land Interactions*. Cambridge: Cambridge University Press, 2015.

[39] L. Xuhui, *Fundamentals of Boundary-Layer Meteorology*. 2018.

[40] P. Baas, *Turbulence and low-level jets in the stable boundary layer*. phd, S.n., [S.l., 2009. ISBN: 9789085854463 Pages: -.

[41] J. A. Businger, J. C. Wyngaard, Y. Izumi, and E. F. Bradley, "Flux-Profile Relationships in the Atmospheric Surface Layer," *J. Atmos. Sci.*, vol. 28, pp. 181–189, Mar. 1971.

[42] Eurocode, "Eurocode 1 : Actions sur les structures - Partie 1-4," 2005.

[43] J. E. Cermak and S. P. S. Arya, "Problems of atmospheric shear flows and their laboratory simulation," *Boundary-Layer Meteorology*, vol. 1, pp. 40–60, Mar. 1970.

[44] J. Armitt and J. Counihan, "The simulation of the atmospheric boundary layer in a wind tunnel," *Atmospheric Environment (1967)*, vol. 2, pp. 49–71, Jan. 1968.

[45] R. Avissar, M. D. Moran, G. Wu, R. N. Meroney, and R. A. Pielke, "Operating ranges of mesoscale numerical models and meteorological wind tunnels for the simulation of sea and land breezes," *Boundary-Layer Meteorol*, vol. 50, pp. 227–275, Mar. 1990.

[46] J. E. Cermak, "Applications of Fluid Mechanics to Wind Engineering—A Freeman Scholar Lecture," *Journal of Fluids Engineering*, vol. 97, pp. 9–38, Mar. 1975.

[47] O. G. Sutton, "The application to micrometeorology of the theory of turbulent flow over rough surfaces," *Quarterly Journal of the Royal Meteorological Society*, vol. 75, no. 326, pp. 335–350, 1949. _eprint: https://rmets.onlinelibrary.wiley.com/doi/pdf/10.1002/qj.49707532602.

[48] A. N. Kolmogorov, "The local structure of turbulence in incompressible viscous fluid for very large Reynolds numbers," *C. R. Acad. Sci. URSS*, vol. 30, pp. 301–305, 1941.

[49] J. E. Cermak and N. Isyumov, *Wind tunnel studies of buildings and structures*. Reston, VA: American Society of Civil Engineers, 1999. OCLC: 698590481.

[50] M. Jensen and N. Franck, "Model-scale tests in turbulent wind," 1963.

[51] A. G. Davenport and N. Isyumov, "The application of a the boundary layer wind tunnel to the prediction of wind loading," 1967.

[52] P. R. Owen and H. K. Zienkiewicz, "The production of uniform shear flow in a wind tunnel," *Journal of Fluid Mechanics*, vol. 2, pp. 521–531, Aug. 1957. Publisher: Cambridge University Press.

[53] J. C. R. Hunt and H. Fernholz, "Wind-tunnel simulation of the atmospheric boundary layer: a report on Euromech 50," *Journal of Fluid Mechanics*, vol. 70, pp. 543–559, Aug. 1975. Publisher: Cambridge University Press.

[54] Armitt, "The simulation of the atmopsheric boundary layer in a wind tunnel," *C.E.R.L Note*, no. RD/L/N/83/66, 1966.

[55] J. Counihan, "Simulation of an adiabatic urban boundary layer in a wind tunnel," *Atmospheric Environment (1967)*, vol. 7, pp. 673–689, July 1973.

[56] H. Kozmar, "Scale effects in wind tunnel modeling of an urban atmospheric boundary layer," *Theoretical and Applied Climatology*, vol. 100, pp. 153–162, Mar. 2010.

[57] N. J. Cook, "On simulating the lower third of the urban adiabatic boundary layer in a wind tunnel," *Atmospheric Environment (1967)*, vol. 7, pp. 691–705, July 1973.

[58] G. Campbell and N. Standen, "Simulation of earth's surface winds by artificially thickened wind tunnel boundary layers," *Progress Report, National Research Council of Canada, NAE Report LTR-LA-37*, vol. II, 1969.

[59] N. Standen, "A spire array for generating thick turbulent shear layers for natural wind simulation in wind tunnels," *Laboratory technical report LA-94, NAtional Aeronautical Establishment, Ottawa, Canada*, 1972.

[60] H. P. A. H. Irwin, "Design and use of spires for natural wind simulation," *Laboratory Technical Report (National Research Council of Canada. National Aeronautical Establishment. Low Speed Aerodynamics Laboratory)*, p. 65 p., Aug. 1979. Artwork Size: 65 p. Publisher: National Research Council of Canada. National Aeronautical Establishment.

[61] W. G. Rose, "Results of an attempt to generate a homogeneous turbulent shear flow," *Journal of Fluid Mechanics*, vol. 25, pp. 97–120, May 1966. Publisher: Cambridge University Press.

[62] S. Corrsin, "Turbulence: Experimental Methods," *Handbuch der Physik*, vol. 3, pp. 524–590, 1963.

[63] J. W. Elder, "Steady flow through non-uniform gauzes of arbitrary shape," *Journal of Fluid Mechanics*, vol. 5, pp. 355–368, Apr. 1959. Publisher: Cambridge University Press.

[64] S. Khanna and J. G. Brasseur, "Three-Dimensional Buoyancy- and Shear-Induced Local Structure of the Atmospheric Boundary Layer," *Journal of the Atmospheric Sciences*, vol. 55, pp. 710–743, Mar. 1998. Publisher: American Meteorological Society Section: Journal of the Atmospheric Sciences.

[65] C. Farell and A. K. S. Iyengar, "Experiments on the wind tunnel simulation of atmospheric boundary layers," *Journal of Wind Engineering and Industrial Aerodynamics*, vol. 79, pp. 11–35, Jan. 1999.

[66] K. Varshney and K. Poddar, "Experiments on integral length scale control in atmospheric boundary layer wind tunnel," *Theor Appl Climatol*, vol. 106, pp. 127–137, Nov. 2011.

[67] S. Du, M. Li, and Y. Yang, "Effects of turbulence integral scales on characteristics of fluctuating wind pressures," *Journal of Wind Engineering and Industrial Aerodynamics*, vol. 204, p. 104245, Sept. 2020.

[68] C. Ott, *Caractérisation dynamique d'actionneurs fluidiques, et identification expérimentale des mécanismes dynamiques d'interaction jet - couche limite induits.* phdthesis, Université Polytechnique Hauts-de-France, Jan. 2020.

[69] G. Comte-Bellot, "Hot-wire anemometry," *Annual Review of Fluid Mechanics*, vol. 8, no. 1, pp. 209–231, 1976.

[70] I. Rusli, S. Aleksandrova, H. Medina, and S. Benjamin, "Using single-sensor hot-wire anemometry for velocity measurements in confined swirling flows," *Measurement*, vol. 129, pp. 277–280, 2018.

[71] G. I. Taylor, G. K. Batchelor, H. L. Dryden, and G. B. Schubauer, "THE EFFECT OF WIRE GAUZE ON SMALL DISTURBANCES IN A UNIFORM STREAM," *Q J Mechanics Appl Math*, vol. 2, pp. 1–29, Jan. 1949. Publisher: Oxford Academic.

[72] K. E. G. Wieghardt, "On the Resistance of Screens," *Aeronautical Quarterly*, vol. 4, pp. 186–192, Aug. 1953. Publisher: Cambridge University Press.

[73] W. Cornell, "Losses of flow normal to plane screens," *Trans. ASME*, vol. 80, no. 4, pp. 791–799, 1958.

[74] U. Karnik and S. Tavoularis, "Generation and manipulation of uniform shear with the use of screens," *Experiments in Fluids*, vol. 5, pp. 247–254, July 1987.

[75] G. B. Schubauer, W. G. Spangenberg, and P. S. Klebanoff, "Aeodynamic Characteristics of Damping Screens," tech. rep., NATIONAL AERONAUTICS AND SPACE ADMINISTRATION WASHINGTON DC, Jan. 1950. Section: Technical Reports.

[76] A. J. Reynolds, "Flow Deflection by Gauze Screens," *Journal of Mechanical Engineering Science*, vol. 11, pp. 290–294, June 1969. Publisher: IMECHE.

[77] J. C. Gibbings, "The pyramid gauze diffuser," *Ing. arch*, vol. 42, pp. 225–233, July 1973.

[78] S. Li, J. Latt, and B. Chopard, "Model for pressure drop and flow deflection in the numerical simulation of stents in aneurysms," *International Journal for Numerical Methods in Biomedical Engineering*, vol. 34, no. 3, p. e2949, 2018. _eprint: https://onlinelibrary.wiley.com/doi/pdf/10.1002/cnm.2949.

[79] E. M. Laws and J. L. Livesey, "Flow Through Screens," *Annual Review of Fluid Mechanics*, vol. 10, no. 1, pp. 247–266, 1978. _eprint: https://doi.org/10.1146/annurev.fl.10.010178.001335.

[80] P. Roach, "The generation of nearly isotropic turbulence by means of grids," *International Journal of Heat and Fluid Flow*, vol. 8, no. 2, pp. 82–92, 1987.

[81] M. R. Raupach, R. A. Antonia, and S. Rajagopalan, "Rough-Wall Turbulent Boundary Layers," *Applied Mechanics Reviews*, vol. 44, pp. 1–25, Jan. 1991.

[82] J. Nikuradse, "Laws of flow in rough pipes," *VDI Forschungsheft*, p. 361, 1933.

[83] P. K. Kundu, I. M. Cohen, and D. R. Dowling, "Chapter 12 - Turbulence," in *Fluid Mechanics (Sixth Edition)* (P. K. Kundu, I. M. Cohen, and D. R. Dowling, eds.), pp. 603–697, Boston: Academic Press, Jan. 2016.

[84] H. Schlichting, *Experimental Investigation of the Problem of Surface Roughness*. National Advisory Commitee for Aeronautics, 1937. Google-Books-ID: 6s5CAQAAIAAJ.

[85] D. O. Mora and M. Obligado, "Estimating the integral length scale on turbulent flows from the zero crossings of the longitudinal velocity fluctuation," *Experiments in Fluids*, vol. 61, p. 199, Aug. 2020.

[86] E. Dogan, R. E. Hanson, and B. Ganapathisubramani, "Interactions of large-scale free-stream turbulence with turbulent boundary layers," *Journal of Fluid Mechanics*, vol. 802, pp. 79–107, Sept. 2016. Publisher: Cambridge University Press.

[87] K. A. Chauhan, P. A. Monkewitz, and H. M. Nagib, "Criteria for assessing experiments in zero pressure gradient boundary layers," *Fluid Dynamics Research*, vol. 41, p. 021404, Mar. 2009. Publisher: IOP Publishing.

[88] J. Counihan, "Adiabatic atmospheric boundary layers: A review and analysis of data from the period 1880-1972," *Atmospheric Environment*, vol. 9, pp. 871–905, Jan. 1975.

[89] G. I. Taylor, "Statistical theory of turbulence," *Proceedings of the Royal Society of London. Series A - Mathematical and Physical Sciences*, vol. 151, pp. 421–444, Sept. 1935. Publisher: Royal Society.

[90] R. Macdonald, R. Griffiths, and D. Hall, "An improved method for the estimation of surface roughness of obstacle arrays," *Atmospheric Environment*, vol. 32, no. 11, pp. 1857–1864, 1998.

[91] R. B. Cal, J. Lebrón, L. Castillo, H. S. Kang, and C. Meneveau, "Experimental study of the horizontally averaged flow structure in a model wind-turbine array boundary layer," *Journal of Renewable and Sustainable Energy*, vol. 2, p. 013106, Jan. 2010. Publisher: American Institute of Physics.

[92] T. Kurian and J. H. M. Fransson, "Grid-generated turbulence revisited," *Fluid Dynamics Research*, vol. 41, p. 021403, Mar. 2009. Publisher: IOP Publishing.

[93] A. Trush, S. Pospíšil, and H. Kozmar, "COMPARISON OF TURBULENCE INTEGRAL LENGTH SCALE DETERMINATION METHODS," pp. 113–123, Nov. 2020.

[94] S. B. Pope, *Turbulent Flows*. Cambridge University Press, 2000.

[95] R. Hill, "Corrections to taylor's frozen turbulence approximation," *Atmospheric Research*, vol. 40, no. 2, pp. 153–175, 1996. Trophospheric turbulence.

[96] H. Tennekes and J. L. Lumley, *A first course in turbulence*. Cambridge, Mass: MIT Press, 1972.

[97] J. McFadden, "The axis-crossing intervals of random functions–ii," *IRE Transactions on Information Theory*, vol. 4, no. 1, pp. 14–24, 1958.

[98] K. R. Sreenivasan, A. Prabhu, and R. Narasimha, "Zero-crossings in turbulent signals," *Journal of Fluid Mechanics*, vol. 137, p. 251–272, 1983.

[99] N. Mazellier and J. C. Vassilicos, "The turbulence dissipation constant is not universal because of its universal dependence on large-scale flow topology," *Physics of Fluids*, vol. 20, Jan. 2008. Publisher: American Institute of Physics.

[100] R. Flay and D. Stevenson, "Integral length scales in an atmospheric boundary-layer near the ground," in *Australasian Fluid Mechanics Conference, 9 th, Auckland, New Zealand*, pp. 464–467, 1987.

Appendix A

Three methods for the integral length scales estimation

This appendix describes the three methods utilized to compute the longitudinal integral length scale $L_{uu,x}$ from the data measured using the Hot Wire Anemometry (HWA) technique. The integral length scale is defined as an estimate of the maximum separation distance across which the eddy velocities' components are correlated at two different points [92]. In other words, this quantity can be seen as a statistical average size of the eddies which contain the most energy in the respective directions, caused by the velocity fluctuation in the longitudinal direction [93]. Therefore, this length scale is relevant for engineering applications since it is representative of the whole spectrum of energy-containing eddies.

A.1 Integration of the correlation function R_{uu}

The integration of the correlation function R_{uu} represents the rigorous method to estimate the integral length scale in a turbulent flow, since it derives directly from the definition of integral length scale.

In statistics if $\underline{U}$ is a random variable which is a continuous function of a coordinate $\underline{x}$, it is called *random field*. The velocity of a turbulent flow can be regarded as a random field $\underline{U} = U(\underline{x}, t)$, with fluctuation $\underline{u'} = \underline{U} - \langle \underline{U} \rangle$ according to the Reynolds decomposition. According to Pope (2000) [94], the two-point single-time *autocorrelation tensor* of $\underline{U}$ can be defined as:

$$R_{ij}(\underline{x}, \underline{r}) = \left\langle u_i'(\underline{x}) u_j'(\underline{x} + \underline{r}) \right\rangle$$

The *integral length scale* measured along the direction $\underline{n} = \underline{r}/|\underline{r}|$ is:

$$\mathcal{L}(\underline{n}) = \int_0^\infty \frac{R_{ii}(\underline{r})}{\langle u_i' u_i' \rangle} dr \tag{A.1}$$

where $\underline{r}$ is the coordinate along the $\underline{n}$ direction. However, the autocovariance tensor R_{ii} is not easy to compute and the concept of *autocorrelation* is used. The latter represents the degree of similarity between a given time series and a lagged version of itself over successive time intervals. The *autocorrelation* of $\underline{U}$ is defined as: $\langle u'(t)u'(t-\tau)\rangle$.

A common practice in turbulence is to apply the Taylor frozen turbulence hypothesis, Hill (1996) [95], which allows to compute the autocorrelation function knowing the time history at one point only (i.e. from the data measured by a hot-wire anemometer). As a result, the longitudinal correlation function can be measured as:

$$\langle u'(\underline{x},t)u'(\underline{x}+r,t)\rangle \approx \langle u'(\underline{x},t)u'(\underline{x},t-r/\langle\underline{U}\rangle)\rangle$$

where $\tau = r/\langle\underline{U}\rangle$ is the time delay between the two measurement. Finally, the longitudinal integral length scale can be calculated as:

$$\mathcal{L}_{uu,x} = \langle U\rangle \int_0^\infty \frac{\langle u'(t)u'(t-\tau)\rangle}{\langle u'u'\rangle} d\tau \tag{A.2}$$

A.2 Turbulence kinetic energy spectrum $E_{11}(k)$ interpolation

A good estimate of the turbulence length scales can be obtained using spectral turbulence models which are mostly based on empirical data. Indeed, the vortex size that corresponds to the highest spectral energy is the integral turbulence length scale according to spectral methods. The time scale corresponding to the frequency with the highest amount of energy in the spectrum, or peak frequency, is used to calculate the length scale [93].

Given the turbulence kinetic energy spectrum $E_{11}(k)$, the *longitudinal integral length scale* can be estimated using the relation suggested by Tennekes & Lumley (1972) [96]:

$$\mathcal{L}_{uu,x} = \frac{\pi E_{11}(0)}{2u'^2}$$

In order to estimate the power spectra, one of the most frequently used methods is the von Karman model [13](applied also by Zheng *et al.*, 2018 [11]):

$$E_{11}(k) = \frac{2u'^2\mathcal{L}_{uu,x}}{\pi}\left\{1+\left[\frac{k\mathcal{L}_{uu,x}B\left(1/2,1/3\right)}{\pi}\right]\right\}^{-5/6} \tag{A.3}$$

where $k = 2\pi f/U_\infty$ is the *wavenumber* (with f being the frequency in time), $B\left(1/2,1/3\right) = \Gamma(1/2)\Gamma(1/3)\Gamma(5/6)$ is the *beta function* and $\Gamma(n) = (n-1)!$ is the *gamma function*.

After taking the average of the spectra of two packets of data, the equation (A.3) is used to fit the data in a least square sense: one example is given in Figure A.1. Unfortunately, most spectrum models have flaws in the low frequency range.

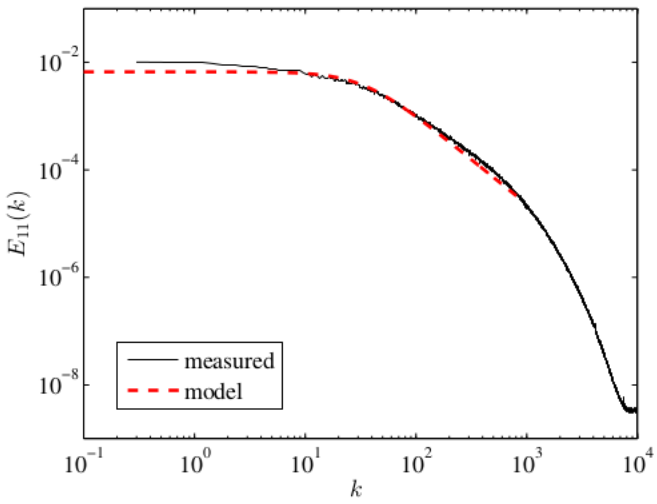

Figure A.1: Example spectrum from one of the grid analyzed in Zheng *et al.* (2018) [11].

A.3 Zero crossing of the longitudinal velocity fluctuation

This section describes the method introduced by Mora & Obligado (2020) [85] for estimating integral length scale and Taylor microscale using the zero crossing analysis of the streamwise velocity fluctuation u'.

First, the Reynolds decomposition of streamwise velocity is applied to extract the Eulerian fluctuating velocity $u'(\tau) = U - \langle U \rangle$ (the vector symbol is omitted). Then, the set of times instants τ_i^c for which $u'(\tau_i^c) = 0$ is computed (as shown in Figure A.2a) and a list of zero crossing is obtained. The latter can be converted from time into space by using the Taylor hypothesis $Z_i = \tau_i^c \langle U \rangle$.

The McFadden (1958) [97] method is applied for the analysis of the turbulent signals which is based on the assumption that intervals between successive zero crossing (ΔZ) are statistically independent. As a result, the variance for intervals between zeros can be expressed as follows:

$$Var(\Delta Z) = 2 \langle \Delta Z \rangle \int_0^\infty \frac{2}{\pi} arcsin(\rho(\tau)) d\tau$$

By computing the *arcsin* Taylor series and truncating it up to the $1st$ term, the following relation for the *integral length scale* is obtained:

$$\mathcal{L} = \frac{\pi}{4} \frac{Var(\Delta Z}{\langle \Delta Z \rangle} \approx \langle U \rangle \int_0^\infty \rho(\tau) d\tau = \langle U \rangle \mathcal{T} = \int_0^\infty \rho(r) dr \tag{A.4}$$

where $\mathcal{T}$ is the *integral time scale*.

If all the measurements have enough temporal resolution, the zero crossing method also enables to estimate the Taylor micro-scale λ. There is a common procedure to verify that

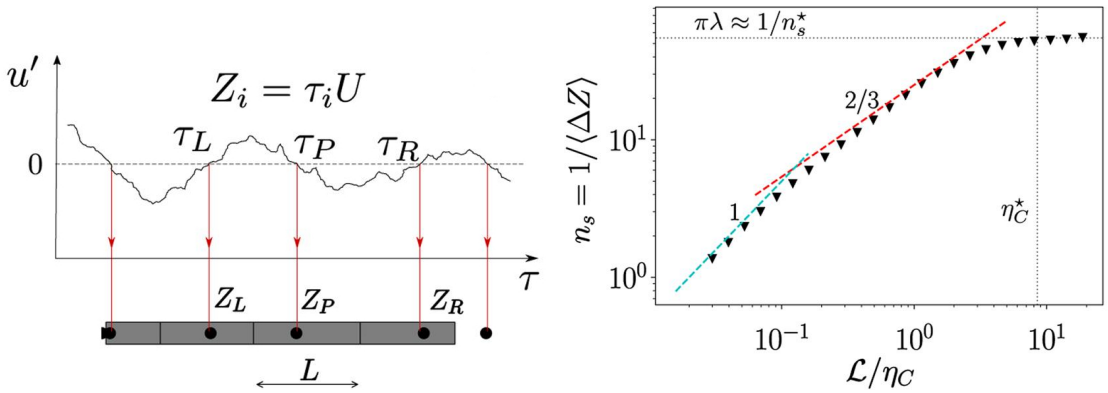

(a) Zero crossings and 1D Voronoï tessellation illustration, from Mora & Obligado (2020) [85].

(b) Zero-crossing computation example from Mora & Obligado (2020) [85].

Figure A.2: Identification of the intervals between zeros and validation of the Taylor micro-scale computation.

the estimation is reliable (Sreenivasan *et al.* 1983 [98], Mazellier and Vassilicos 2008 [99]):

- The measured fluctuating velocity signal has to be low pass filtered (with a high-order filter) at various sizes $\eta_C = 2\pi/k$, where k is the wavenumber.
- The ratio n_s of zero crossings to signal duration is determined for each filter size.
- The n_s value can be considered well resolved whether a plateau of n_s is achieved for filter scales smaller than a certain scale $\eta_C^\star$.

Figure A.2b shows a scenario where n_c is well resolved, in that case the Taylor micro-scale (λ) can be estimated as follows:

$$n_s^{-1}|_\star = \pi C \lambda$$

where $C \approx 1$ is a constant which takes into account the "non-Gaussianity" of the velocity derivative (Mazellier and Vassilicos, 2008 [99]).

Appendix B

Comparison of the methods for the integral length scales estimation

The "Turbulence kinetic energy spectrum interpolation" and the "Zero crossing of the longitudinal velocity fluctuation" methods are introduced to avoid the complications that occurs when the correlation function does not cross the horizontal axis because of random fluctuation (see [100] for instance).

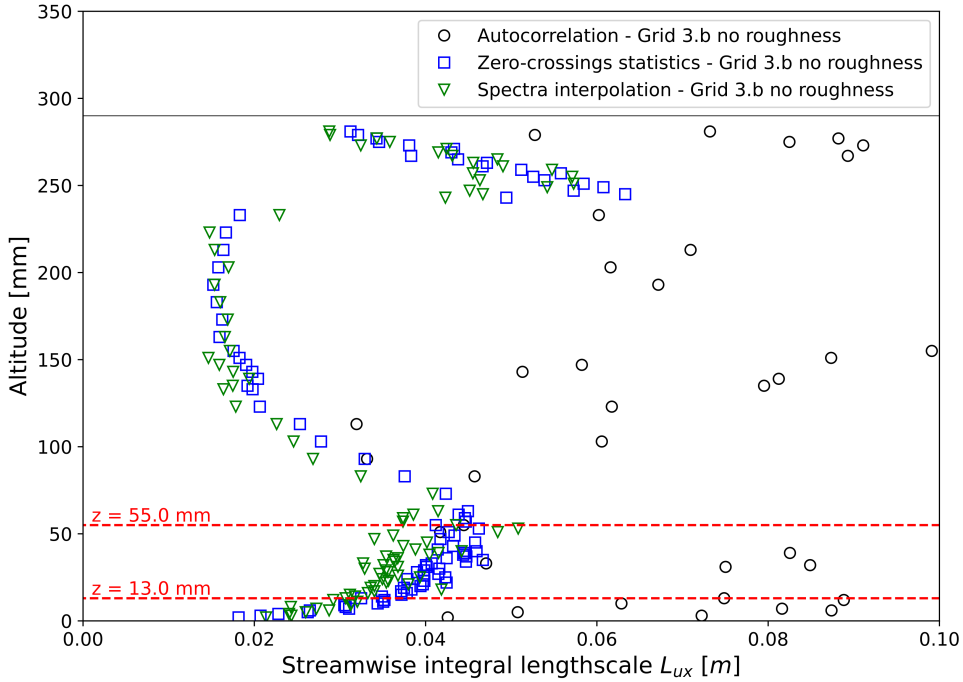

Figure B.1: Integral length scales produced by grid 3.b and computed using: integration of the autocorrelation function, interpolation of the turbulence kinetic energy spectrum and zero crossing statistics of the velocity fluctuation.

Figure B.1 shows a comparison of the length scales estimated using the three methods presented in Appendix A. The analysis considers Grid 3.b without roughness at the wall, but the same conclusions can be made for the other devices. The findings from the zero crossing statistics and spectrum interpolation approaches are often in excellent agreement,

however the integration of the autocorrelation function method seems to overestimate the integral length scales.

Two points in the normal-wall direction are considered: $z = 13\ mm$ and $z = 55\ mm$. In $z = 55\ mm$ the three methods give similar results, while in $z = 13\ mm$ the autocorrelation method appears to overestimate the integral length scale.

In order to understand which methods give physical results, the three methods need to be verified for the two positions highlighted in Figure B.1. The data gathered with the single hot wire anemometer DANTEC 55P15 are considered for the following analysis.

Figure B.2 shows a comparison of the normalized autocorrelation functions calculated at the two positions in the z directions. In Figure B.2a it is possible to see that the correlation function does not cross the horizontal axis before $t = 0.05\ s$, providing high values for integral length scales. This behaviour is not visible at $z = 55\ mm$, where the crossing takes place at $t = 0.02\ s$. The comparison demonstrates that this approach has a tendency to overestimate the turbulent integral length scale when the large random fluctuations prevent the autocorrelation function from crossing the horizontal axis.

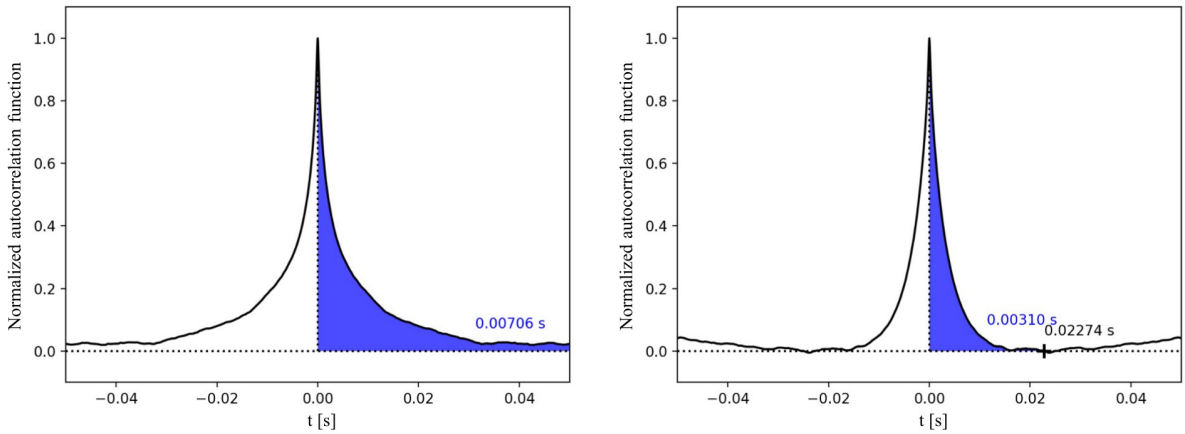

(a) $z = 13\ mm$. **(b)** $z = 55\ mm$.

Figure B.2: Normalized autocorrelation function computed at two different points in the normal-wall direction. The integral length scale estimate is displayed in blue.

Figure B.3 shows the normalized turbulence energy spectrum $E_{11}(f)$ and its interpolation using the von Karman model [13] for the same two z positions. The spectrum interpolation appears to be accurate for both locations. Therefore, the "Turbulence kinetic energy spectrum interpolation" approach provides a reliable estimate of the integral length scales for grid-generated flows

Finally, Mora & Obligado (2020) [85] does not provide a method to verify the reliability of the integral length scales estimate. They only suggest a procedure to verify the accuracy of the Taylor microscale (which is considered in this section). However, they stated that the "Zero crossing of the longitudinal velocity fluctuation" method give reliable results even under challenging experimental conditions because it is not dependant of the equipment calibration. Moreover, the results of this approach and the spectrum interpolation method

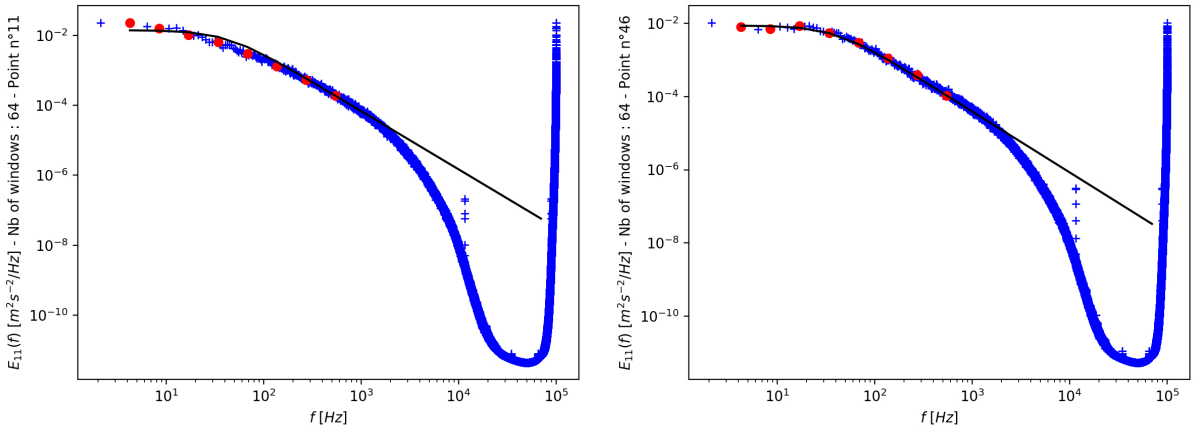

(a) $z = 13\ mm$. **(b)** $z = 55\ mm$.

Figure B.3: Normalized turbulence energy spectrum $E_{11}(f)$ (in blue) and its interpolation through the von Karman model [13] (in black). The points utilized for the interpolation are displayed as red dots.

are clearly comparable, as shown in Figure B.1.

To summarize, the three methods give similar estimations of the integral length scale when the autocorrelation function crosses the horizontal axis. However, when this does not occur, the autocorrelation technique give very high integral length scales which are not physical. On the other hand, the other two methods appear to give physical results over the whole profile. For this reason, the integral length scales analysis (presented in subsection 5.2.6) only consider the findings given by the "Turbulence kinetic energy spectrum" and the "Zero crossing of the longitudinal velocity fluctuation" approaches.